



TITLE:

# 走査型誘電顕微鏡による生体インピーダンスのイメージング

AUTHOR(S):

浅見, 耕司

---

CITATION:

浅見, 耕司. 走査型誘電顕微鏡による生体インピーダンスのイメージング. 2002

ISSUE DATE:

2002-03

URL:

<http://hdl.handle.net/2433/84769>

RIGHT:

# 走査型誘電顕微鏡による生体インピーダンスのイメージング

(課題番号 12680829)

平成12年度～平成13年度科学研究費補助金（基盤研究（C）（2））  
研究成果報告書

平成14年3月

研究代表者 浅見 耕司  
(京都大学化学研究所)

京 都 大 学 図 書



9810055230

附 属 図 書 館

# 走査型誘電顕微鏡による生体インピーダンスのイメージング

(課題番号 12680829)

平成12年度～平成13年度科学研究費補助金（基盤研究（C）(2)）  
研究成果報告書

平成14年3月

研究代表者 浅見 耕司  
(京都大学化学研究所)

はしがき

以前、単一細胞や顕微鏡レベルの組織を調べる方法として、走査型誘電顕微鏡法を開発した (K. Asami, Meas. Sci. Technol. 5: 589-592 (1994))。この方法は、微小電極を試料上で走査して、局所インピーダンスを測定し、インピーダンスのイメージングを行う方法である。試作機では、試料を肉眼で見ながら、目的の走査領域を設定していたため、顕微鏡レベルの試料については特定の領域を狙って測定することはできなかった。本研究では走査型プローブユニットを光学顕微鏡に組み込み、目的とする試料部分を確実に測定できるようにした。また、インピーダンス・イメージと光学顕微鏡像を同時に測定することにより、インピーダンスと形態のイメージの直接比較を可能にした。これにより、形態と電気的性質の相関研究を行う上で必要な手段を提供することができたと考えている。

#### 研究組織

研究代表者： 浅見 耕司 (京都大学化学研究所、助教授)

#### 交付決定額 (配分額)

(金額単位：千円)

	直接経費	間接経費	合計
平成12年度	2,300	0	2,300
平成13年度	800	0	800
総計	3,100	0	3,100



## 研究発表

### (1) 学会誌等

1. Dielectrospectroscopic monitoring of early embryogenesis in single frog embryos.  
*Phys. Med. Biol.* 45: 3285 – 3297 (2000).  
K. Asami, A. Irimajiri
2. Progression of cell cycle monitored by dielectric spectroscopy and flow-cytometric analysis of DNA content.  
*Yeast* 16:1359-1363 (2000)  
K. Asami, K. Takahashi, and K. Shirahige
3. Dielectric monitoring of cell growth in culture using an inductive probe  
Proceedings of XI International Conference on Electrical Bio-Impedance, 209-211 (2001)  
K. Asami, K.S. Zhao
4. Calculation of dielectric spectra of suspensions of rod-shaped cells using boundary element method  
*Bioelectrochemistry* (in press) 2002  
K. Sekine, N. Torii, C. Kuroda and K. Asami
5. 誘電率計測による酵母細胞分裂サイクルのモニター  
生物工学会誌, 78巻5号, 158–162頁, 2000年  
浅見耕司
6. Characterization of biological cells by dielectric spectroscopy  
*J. Non-crystalline solids* (in press) 2002  
K. Asami
7. Characterization of heterogeneous systems by dielectric spectroscopy  
*Prog. Polym. Sci.* (in press) 2002  
K. Asami

(2) 口頭発表

1. Characterization of biological cells by dielectric spectroscopy.  
1<sup>st</sup> International Conference on Dielectric spectroscopy in Physical, Chemical and Biological Applications, Jerusalem, Israel (March 13-15, 2001)  
K. Asami
2. Dielectric monitoring of cell growth in culture using an inductive probe.  
XI International Conference on Electrical Bio-Impedance, Oslo, Norway (Jun 17-21, 2001)  
K. Asami and K.S. Zhao
3. 境界要素法による棒状細胞懸濁系の誘電スペクトル計算  
第38回日本生物物理学会年会、2000年、9月、仙台  
関根克尚、鳥居野風江、畔田千尋、浅見耕司
4. 境界要素法による出芽酵母懸濁体の誘電スペクトル計算  
第39回日本生物物理学会年会、2001年、10月、大阪  
関根克尚、渡部洋子、飛田由佳里、浅見耕司

(3) 出版物

なし

(4) 研究成果による工業所有権の出願・取得状況

なし

## 研究成果

---

### 目次

1. 緒言
2. 走査型誘電顕微鏡原理
3. 光学顕微鏡への走査型誘電顕微鏡ユニットの組込
4. 測定制御プログラムの開発
5. 測定手順
6. 性能テスト
7. 生物組織を用いた測定
8. 結言

### 図および写真

### 参考資料

---

#### 1. 緒言

生物細胞の懸濁液や組織について、誘電率や導電率を広い周波数に渡って測定すると、誘電緩和現象が見られる。この現象は細胞が高い電気抵抗と大きな電気容量をもつ細胞膜で覆われていることによる。細胞に電場を与えると、細胞膜と導電性の高い細胞質や外部媒質との間の界面で分極現象が生ずる（界面分極）。このため、低い周波数の交流電場では大きな誘電率を示し、周波数の高いところでは、分極が追従できないため誘電率が低下する。この誘電緩和を解析することによって、細胞や組織の構造や電氣的性質が明らかとなる。この解析では、適当なモデルを仮定して、懸濁液のデーターから細胞に関する情報を求めることになる。このため、採用したモデルによって解析結果が異なるという問題が生じる。また、細胞はその状態、形態、電氣的性質に分布があるが、これを考慮すると解析が複雑になるため、通常は分布を考慮しないモデルを用いて解析を行い平均値を求める。一方、組織については構造が一様でなく、インピーダンスに分布がある。これらの問題に対する一つのアプローチは、単一細胞や組織の局所的なインピーダンスを測定する方法を開発することである。

単一細胞のインピーダンス解析法として、すでに回転電場法や誘電泳動法などが開発されている。しかし、これらは懸濁細胞にのみ適用が可能であり、基質に固定された細胞などには用いることができない。一方、組織のインピーダンスのイメージングを行うインピーダンス・トモグラフィーは人体のような比較的大きなものが対象であり、多数の電極を装着する必要があるため、顕微鏡レベルの組織に適用することは困難である。

そこで、単一細胞や顕微鏡レベルの組織を調べる新しい方法として、走査型

誘電顕微鏡法を開発した (K. Asami, Meas. Sci. Technol. 5: 589-592 (1994))。この方法は、微小電極を試料上で走査して、局所インピーダンスを測定し、インピーダンスのイメージングを行う方法である。適当な周波数を選ぶことによって、特定の構造をイメージすることが可能である。以前の試作機では、試料を見ながら、目的の領域を走査することができなかったために、顕微鏡レベルの試料については特定の部分を狙って測定することはできなかった。本研究では走査型誘電顕微鏡を光学顕微鏡と組み合わせて、目的とする試料部分を確実に測定できるようにした。また、インピーダンス・イメージと光学顕微鏡像を同時に測定することにより、インピーダンスと形態のイメージの直接比較が可能になる。

## 2. 走査型誘電顕微鏡原理

走査型誘電顕微鏡の電極配置を図 1 に示す。測定には横方向の分解能を上げるため、3 端子法を用いている。電極は微小同軸プローブ電極と対電極からなる。同軸プローブの外導体（保護電極）と内導体（測定または主電極）は、対電極に対して、同電位に保たれている。これにより、測定電極と対電極の間には平行電場が形成され、二電極測定の電極端に見られる電場の広がりを防ぐことができる。したがって、測定スポットの径を絞ることができるため、横方向の分解能を上げることができる。対電極に対して、一定の高さにプローブを保ちながら走査することによって、局所の電気容量とコンダクタンスを測定することができる。この局所の電気容量とコンダクタンスをマッピングすることによって、誘電イメージを得ることができる。この方法の特徴の一つは水中の試料について広い周波数範囲に渡って測定ができる点にあり、誘電緩和現象を単一細胞や組織の局所領域について調べることができる。

## 3. 光学顕微鏡への走査プローブユニットの組込

オリンパス倒立顕微鏡 IMT-2 に中央精機の自動 X-Y ステージを組み込んだ (図 2)。X-Y ステージの最小移動距離は  $1\ \mu\text{m}$ 、移動可能領域は約  $8\text{mm} \times 8\text{mm}$ 。X-Y ステージには試料用チャンバーを固定してある (図 3)。サンプルチャンバーは ITO 透明電極の上に試料用のウェルを備え付けたものである (図 4)。プローブ電極は顕微鏡のコンデンサーレンズ筒部分に固定したアクリル製のフィクスチャーにセットする (図 5)。

図 6 にプローブの模式図を示す。プローブの作成はつぎのように行った。

(1) 外径  $600\ \mu\text{m}$  の注射針の先端を  $90^\circ$  にカットし、ここに外径  $300\ \mu\text{m}$ 、内径  $130\ \mu\text{m}$  のステンレス管 (長さ  $3\text{--}5\ \text{mm}$ ) の一部を押し込む。(2) このステンレス管の内側にテフロン被覆された直径  $76\ \text{mm}$  あるは  $25\ \text{mm}$  の白金線

を挿入する。(3) 注射針の元まで引き出した白金線をコネクター・ピンに銀ペーストで接着し、コネクターピンは注射針の元にアラルダイトで接着する。

(4) 注射針の先端部分の被覆白金線とステンレス管の隙間は銀ペーストで埋めた後、先端からはみ出している白金線を切断する。プローブの先端はさらに砥石で研磨する。

プローブ電極と対電極は同軸ケーブルを用いてインピーダンスアナライザーへ接続する。インピーダンスアナライザーには測定精度の高い HP-4194A Gain Phase / Impedance Analyzer を使用した。High 側の Potential と Current 端子を対電極に、Low 側の Potential と Current 端子はプローブ電極の内導体に接続、外導体はグランドへ接続してある。この状態で、内導体と外導体は対電極に対して同電位は保たれるようになっている。

システム全体の模式図と写真を図 7、8 に示す。

#### 4. 測定制御プログラムの開発

HP-4194A Gain Phase / Impedance Analyzer と中央精機 M9103 DC サーボモーターコントローラーは GP-IB 介して Windows PC で制御した。制御プログラムはナショナルインスツルメントのプログラム言語 LabVIEW を使用して作成した。測定はスポット、ラインスキャン、ラスタスキャンの 3 つのモードで測定できるようにしてある。周波数範囲は 100 Hz - 10 MHz。

指定したステップ幅で X-Y ステージを移動させ、1 ステップ移動毎に設定周波数範囲を掃引して測定する。測定後、ヘッダーファイル、電気容量のデータ・ファイル、コンダクタンスのデータ・ファイルの三つのファイルを作成する。データ・ファイルは Excel のマクロを用いて加工して、特定の周波数の電気容量とコンダクタンスのイメージを得る。また、特定のポイントでの電気容量とコンダクタンスの周波数依存性（誘電スペクトル）も得ることができる。

測定中の光学顕微鏡の画像はリアルタイムで CCD カメラで取り込み、CRT で進行状況をモニターしている。また、インピーダンス・イメージと直接比較できる試料の顕微鏡像は ImagePro を用いてコンピュータに取り込み保存する。

#### 5. 測定手順

試料用チャンバーを顕微鏡より取り外し、試料をセットする。セットにはプラスチックの固定リングを用いる。チャンバーに水を満たした後、顕微鏡の X-Y ステージに固定する。プローブ電極をコンデンサーレンズ筒に装着したフィクスチャーに固定し、プローブ先端を試料に接近させる。次に、顕微鏡の焦点をプローブ先端と試料上端に交互に合わせながらプローブを出来るだけ試料に接近させる。X-Y ステージを手動で測定位置に移動させる。プローブを走査



する範囲はプローブの位置が画像の中心になるように設定してある。走査の範囲とステップ数、周波数範囲、周波数ポイント数、測定電圧などをコンピュータで設定する。測定を開始すると、プローブを1ステップずつ走査し、インピーダンス測定を行う。測定領域全体の走査が終わると、設定した1周波数点での電気容量とコンダクタンスの画像を表示する。誘電データと CCD で取り込んだ静止画像を保存して一連の作業が終了する。

## 6. 性能テスト

今回試作したシステムの性能試験をカーボン・シート、ステンレス・メッシュ、ナイロン・メッシュを用いて行った。プローブには直径 25mm の白金線を内導体にもつものを用いた。図 9 には 1MHz での電気容量とコンダクタンスのイメージを示してある。カーボン・シートは導電性を示すため、コンダクタンスと電気容量はシート上では大きな値になっている。カーボンシートの輪郭がインピーダンスイメージの輪郭と良く一致している。

図 10 にステンレス・メッシュの測定結果を示す。ステンレス・メッシュはステンレス線を編んだもので、線の交差する点ではコンダクタンスと電気容量が共に大きくなっている。インピーダンス・イメージでメッシュの形状を捉えることができる。

図 11 にナイロン・メッシュの測定結果を示す。ナイロン・メッシュは直径約 30  $\mu\text{m}$  のナイロン繊維の織物、メッシュ・サイズは 20 $\times$ 20  $\mu\text{m}$ 。ナイロン繊維の部分は電気容量、コンダクタンスとも小さくなっている。電気容量とコンダクタンスの高い部分はメッシュの目の部分と一致している。

これらの試験測定では、横方向の分解能を正確に見積もることはできないが、おおよそ 10  $\mu\text{m}$  程度ではないかと考えている。

## 7. 生物組織を用いた測定

生体組織として、植物の葉の表皮について、インピーダンス・イメージと光学顕微鏡像の比較を行った。植物の葉から表皮を剥ぎ取り、その測定を水中で行った。光学顕微鏡像から分かるように、表皮は孔辺細胞からなる気孔をもっている。この光学顕微鏡像と電気容量イメージを比較すると (図 12)、電気容量の大きいスポットがちょうど孔辺細胞の位置に対応している。また、コンダクタンスと電気容量のイメージを比較すると、電気容量の高い 2, 3 のスポットがコンダクタンスの高いスポットに対応しているのが分かる。これらの結果は、孔辺細胞が周りの上皮細胞と電氣的性質が異なること、コンダクタンスの高いスポットが開いている気孔に相当すると、気孔の開閉をコンダクタンスのイメージから識別できることを示している。

## 8. 結言

今回試作した装置は市販の比較的大きな倒立顕微鏡に走査プローブユニットを組み込んだため、装置全体がかなり大きなものになってしまった。比較的大きな試料については簡単な光学系で充分であるので、簡易型として、よりコンパクトな装置を作ることが可能である。多くの周波数点を必要としなければ、インピーダンス測定器に安価なものが使えるので、全体として、よりコストパフォーマンスの良いものを実用化することが可能である。

## 参考資料

この研究期間中に誘電顕微鏡やその背景となる研究について、総説2報 (J. Non-crystalline Solids と Progress in Polymer Science、印刷中) にまとめたので以下に収録する。

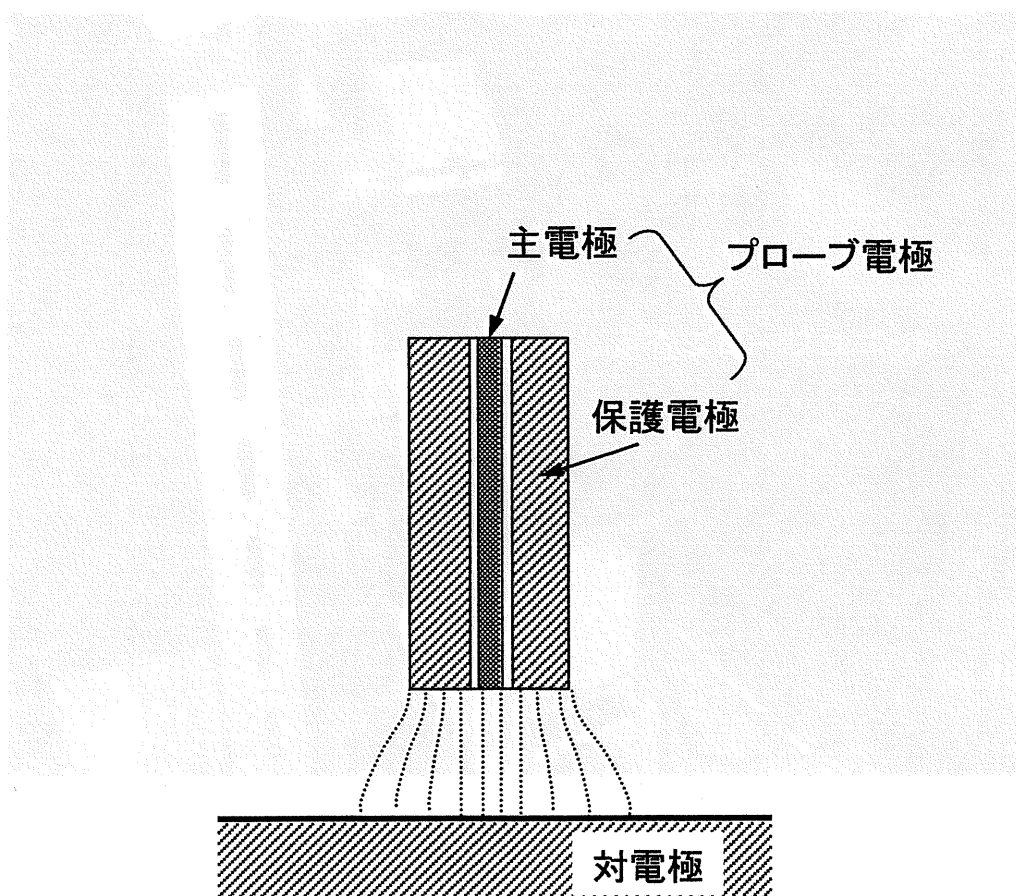


図1 走査型誘電顕微鏡の測定原理(三端子法)。  
主電極と保護電極は対電極に対して同電位に保たれている



図2 倒立型光学顕微鏡にX-Y自動ステージ、試料チャンバー、  
プローブ電極の組込





図4 試料用チャンバー

図3 X-Y自動ステージ、試料チャンバー、プローブ電極、  
プローブ電極フィクスチャー





図4 試料用チャンバー

図5 走査プローブユニット模式図

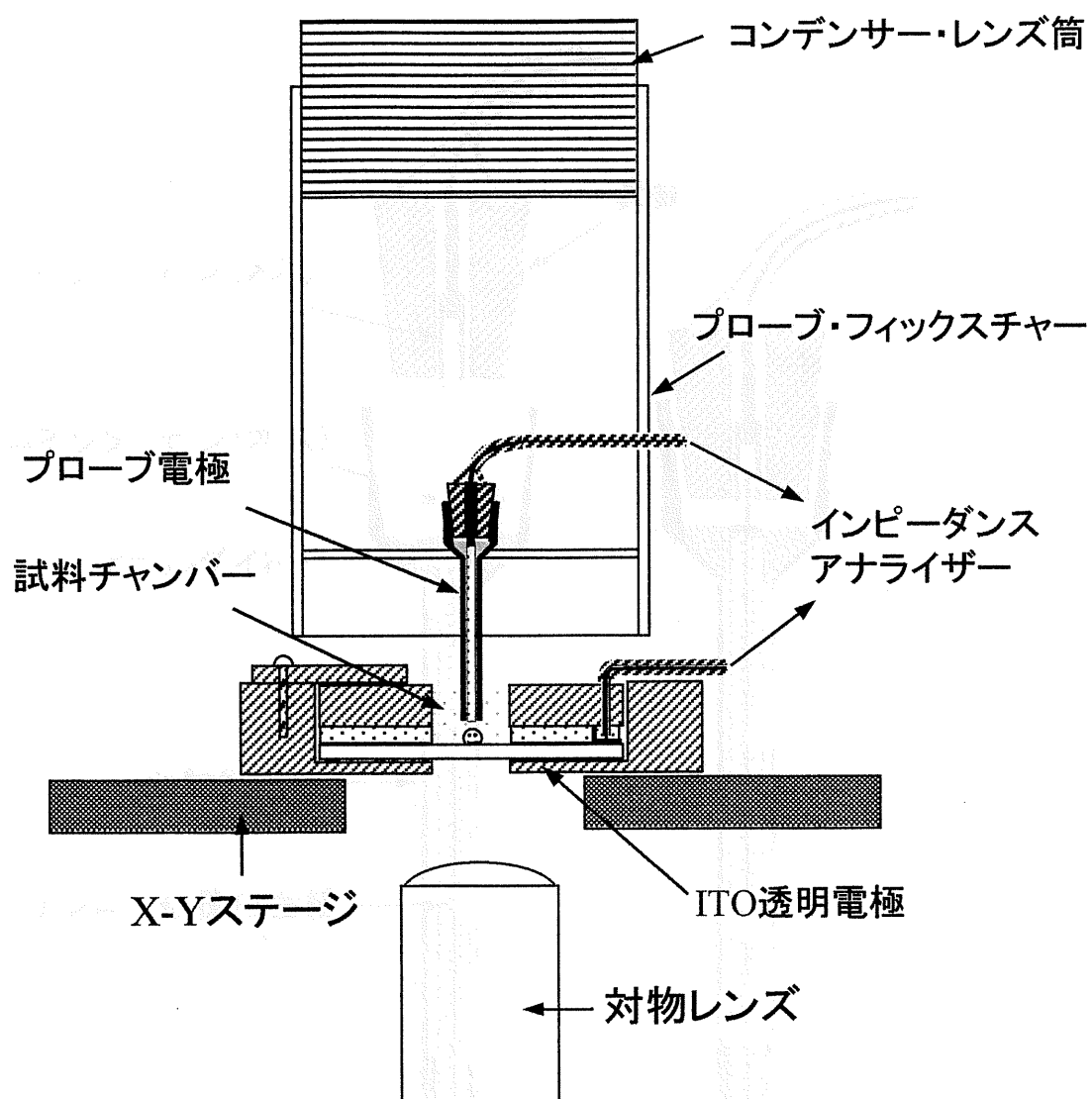


図5 走査プローブユニット模式図

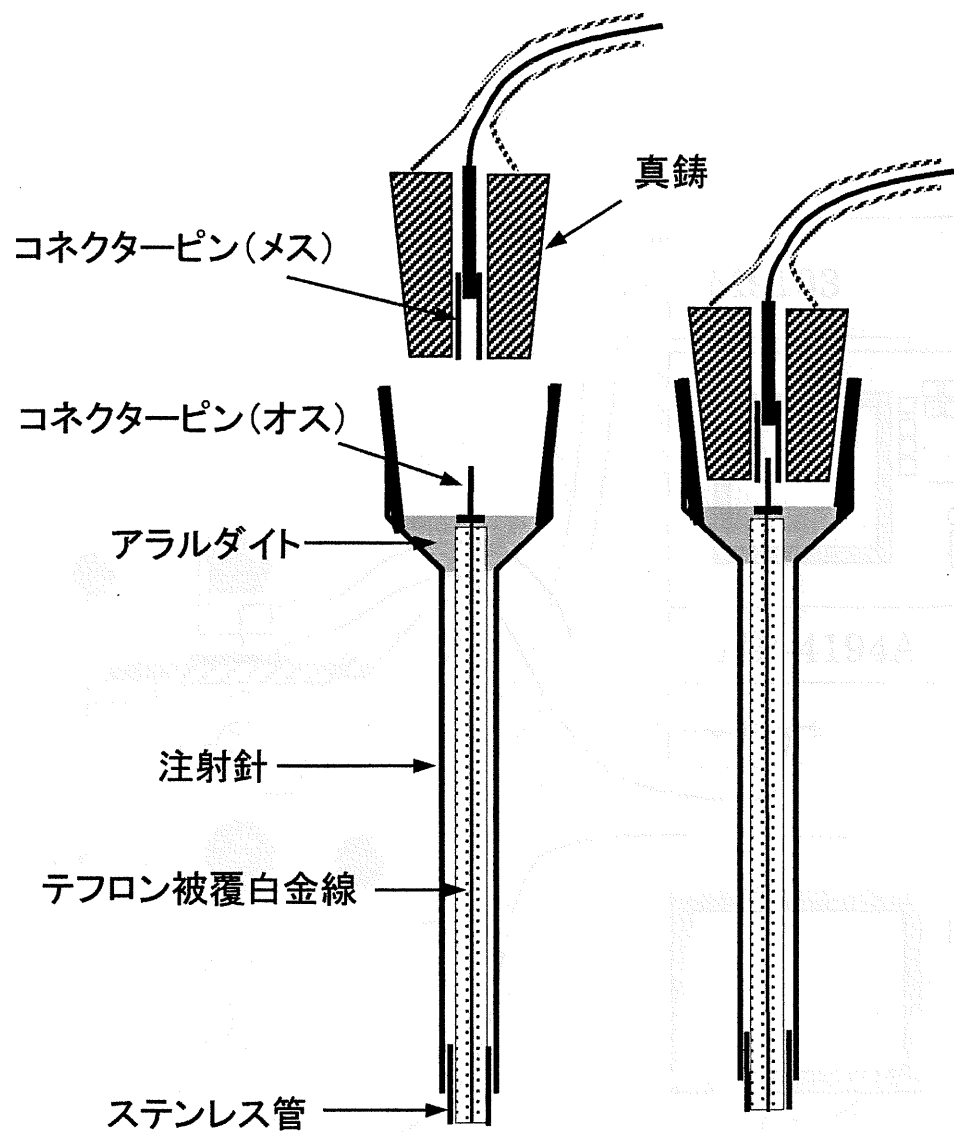


図6 プローブ電極とコネクター模式図

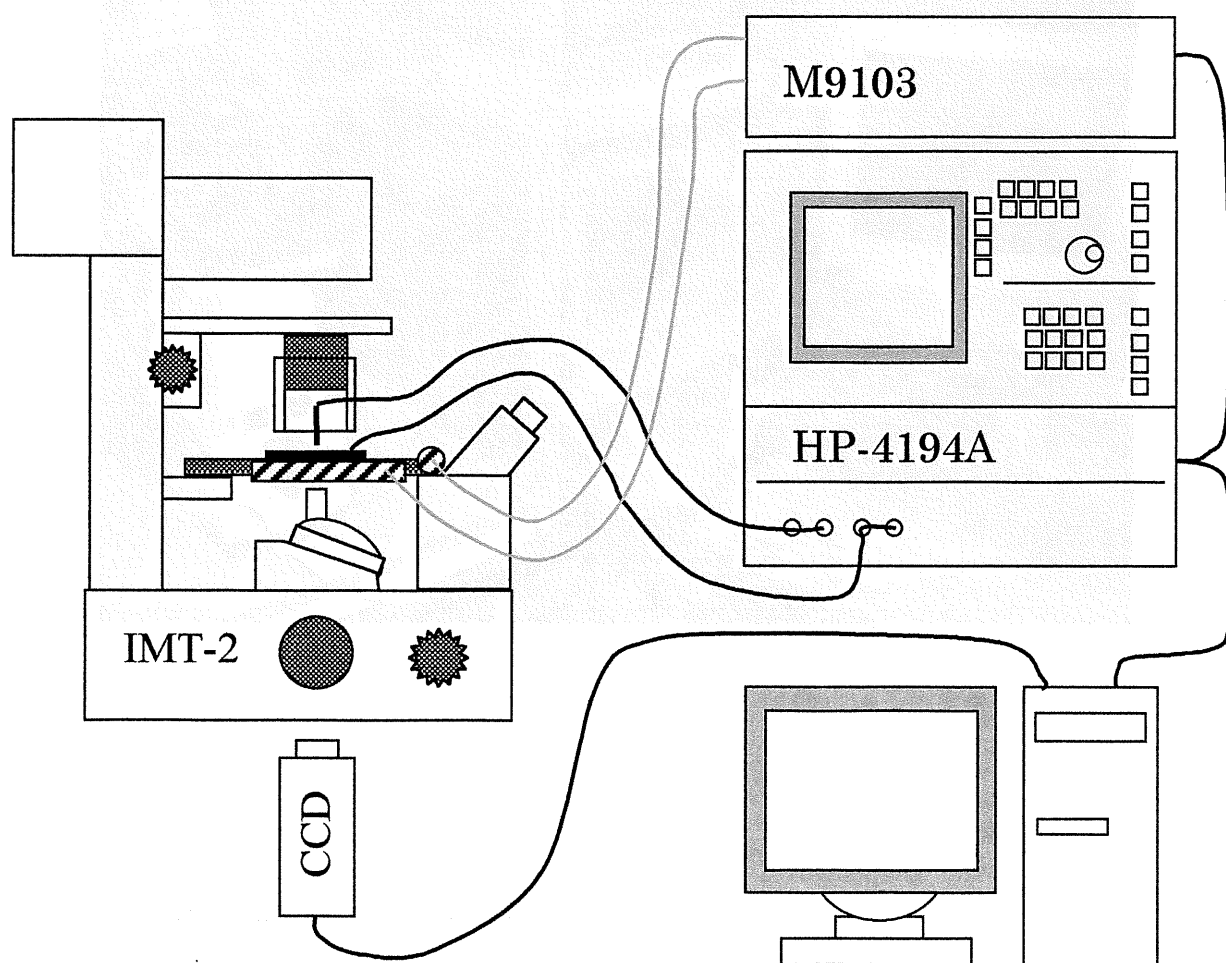


図7 測定システム全体の模式図



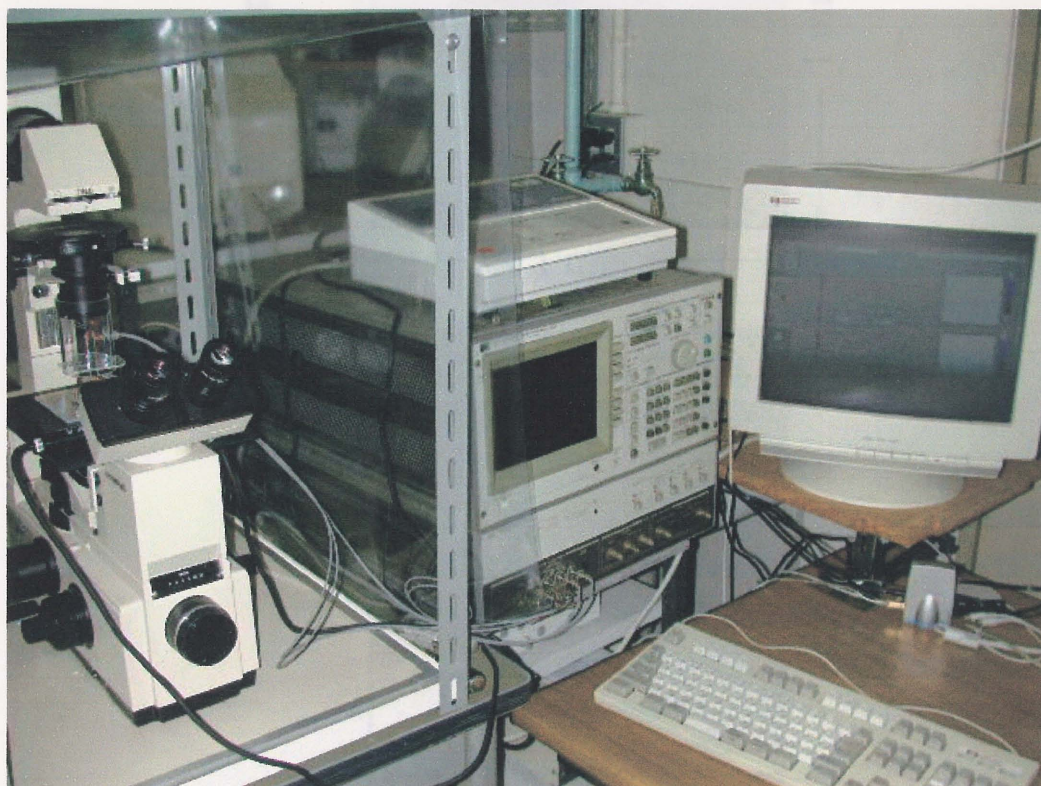


図8 測定システム全体

図9 カarbonシート(水中)の(b)キャパシタンスと(c)コンダクタンスのグレイ・スケールイメージ。(a)カarbonシートの光学顕微鏡像。(b)、(c)には(a)から読み取ったシートの輪郭を重ね書きしてある。



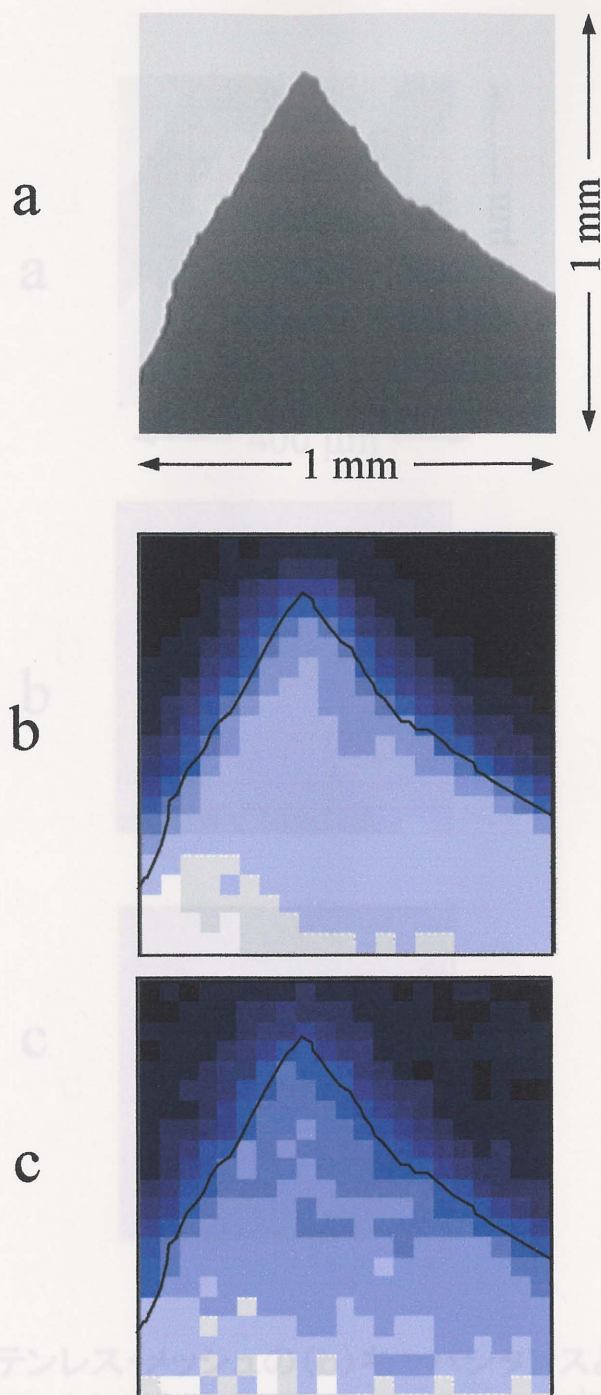


図10 水中のステンレス鋼の(b)キャパシタンスと(c)コンダクタンスのグレイ・スケールイメージ。(a)カーボンシートの光学顕微鏡像。

図9 カーボンシート(水中)の(b)キャパシタンスと(c)コンダクタンスのグレイ・スケールイメージ。(a)カーボンシートの光学顕微鏡像。(b)、(c)には(a)から読み取ったシートの輪郭を重ね書きしてある。

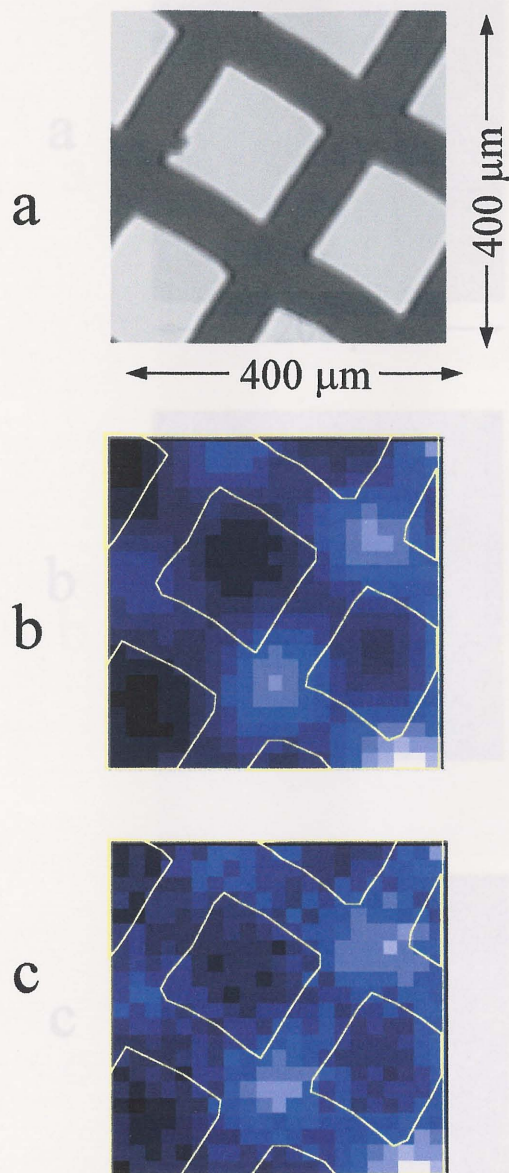


図10 水中のステンレス・メッシュの(b)キャパシタンスと(c)コンダクタンスのグレイ・スケールイメージ。(a)ステンレスメッシュの光学顕微鏡像。(b)、(c)には(a)から読み取ったメッシュの輪郭を重ね書きしてある。



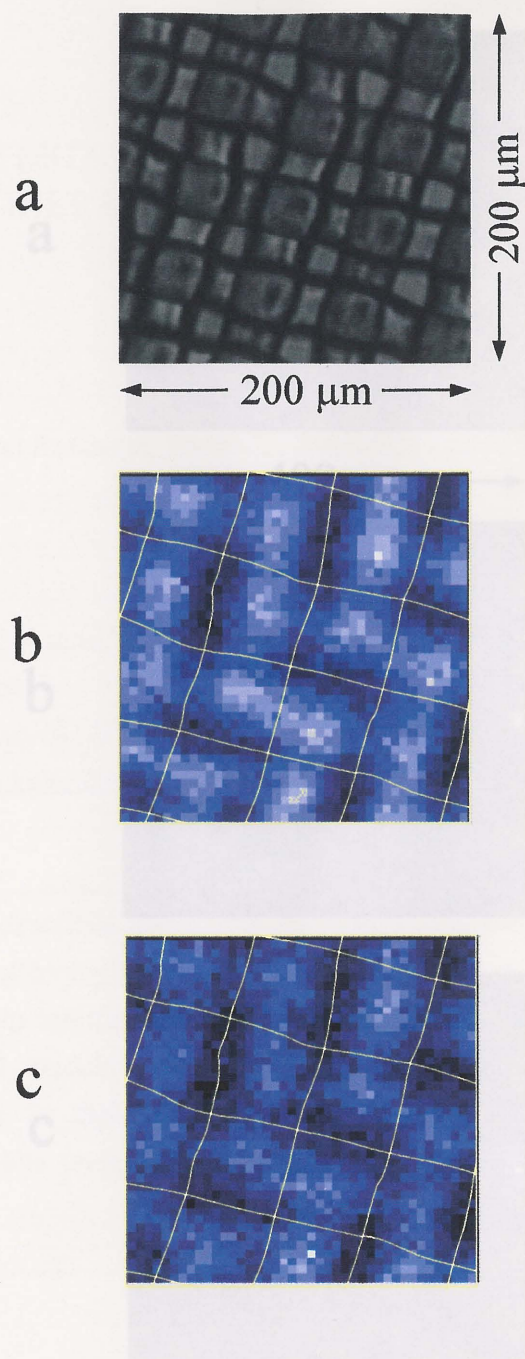


図11 水中のナイロンメッシュの(b)キャパシタンスと(c)コンダクタンスのグレイ・スケールイメージ。(a)ナイロンメッシュの光学顕微鏡像。(b)、(c)には(a)から読み取ったナイロン繊維の中心を通る線を重ね書きしてある。

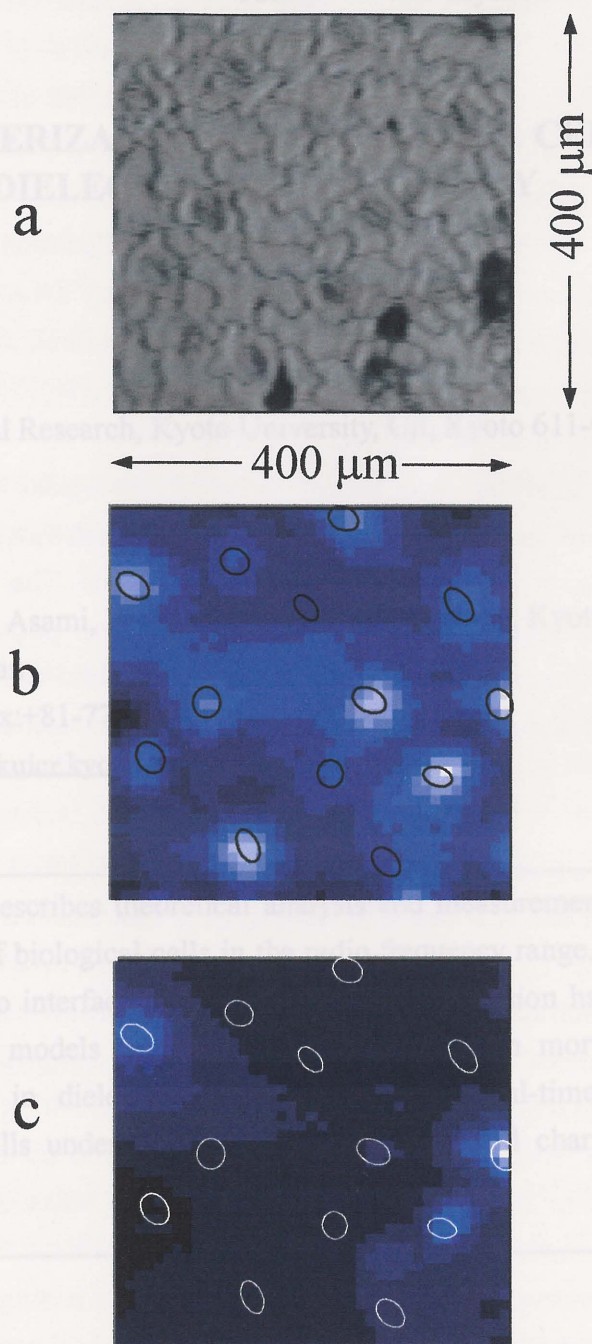


図12 葉の表皮(水中)の(b)キャパシタンスと(c)コンダクタンスの  
グレイ・スケールイメージ。(a)表皮の光学顕微鏡像。  
(b)、cには(a)から読み取った孔辺細胞の輪郭を重ね書きしてある。

## CHARACTERIZATION OF BIOLOGICAL CELLS BY DIELECTRIC SPECTROSCOPY

*Koji Asami*

Institute for Chemical Research, Kyoto University, Uji, Kyoto 611-0011, Japan

Corresponding author: K. Asami, Institute for Chemical Research, Kyoto University,  
Uji, Kyoto 611-0011, Japan

Tel.: +81-774 38 3081; Fax: +81-774 38 3084

E-mail: [asami@tampopo.kuicr.kyoto-u.ac.jp](mailto:asami@tampopo.kuicr.kyoto-u.ac.jp)

---

**Abstract:** This review describes theoretical analysis and measurement techniques for dielectric spectroscopy of biological cells in the radio frequency range. The main focus is the  $\beta$ -dispersion due to interfacial polarization. The  $\beta$ -dispersion has been analyzed using various electrical models proposed for diverse cells in morphology. Recent technical developments in dielectric spectroscopy allow real-time monitoring of dynamic behavior of cells under physiological conditions and characterizing single cells.

---

### 1. Introduction

Dielectric spectroscopy has proved to be a useful technique for analyzing heterogeneous systems, especially biological cell suspensions and tissues because of its capability of non-invasive measurements [1-7]. The application of dielectric spectroscopy is no longer limited to academic researches, but also includes industrial bioprocess controls and medical diagnostics. This review is concerned with (a) theoretical analysis of dielectric behavior of biological cells, (b) dielectric monitoring techniques of cells under physiological conditions, and (c) single-cell approaches to characterize individual cells.



Many biological cells have been studied by dielectric spectroscopy and the dielectric spectra have been analyzed using theories based on various electrical models for cells. The development of personal computers enabled us to deal with complicated and realistic cell models such as composite cell models including intracellular organelles and ellipsoidal cell models for non-spherical cells.

The advent of instruments capable of rapid and automated measurements over a wide range of frequencies has made it possible to study dynamic dielectric behavior in time-dependent phenomena. The phenomena so far studied are cell sedimentation [8], cell aggregation [9], cell division and growth in culture [10,11], organ deterioration [12], and embryogenesis of single frog embryos [13].

Single-cell analysis is a recent trend in biological and medical researches. Characterization of individual cells by dielectric spectroscopy has many advantages over the "suspension" technique with cell populations. The single-cell approach can escape from time-consuming preparation of a uniform population of cells, which is required for the "suspension" technique. In addition, the theoretical analysis becomes relatively simple because it needs not to take into account electrical interactions between cells.

## **2. Theoretical analysis of dielectric dispersion of biological cell suspensions**

A biological cell is a heterogeneous system that consists of the plasma membrane and the cytoplasm. The plasma membrane that is a lipid bilayer containing proteins has low ionic permeability and, therefore, is regarded as a low conducting thin shell. If the cytoplasm is assumed to be a homogeneous phase, the simplest electrical model of the cell is that a conducting sphere is covered with an insulating thin shell [14]. This cell model, called the "single-shell" model, essentially explains dielectric relaxation of cell suspensions due to interfacial polarization (or the Maxwell-Wagner effect), which occurs at the boundaries between materials of different electrical properties. The cytoplasm is, however, a heterogeneous system containing intracellular organelles, proteins, nucleic acids and so forth, and thus its electrical properties are not simple and might depend on frequency. Membrane-bounded intracellular organelles show dielectric relaxation due to interfacial polarization [15-19]. Protein and DNA solutions have dielectric relaxation due to orientation of polar molecules and counterion fluctuation, respectively [20].

When dielectric spectra are measured for biological tissues and cell suspensions over a frequency range of 1 Hz to 10 GHz, three distinct dispersions (or relaxations), termed  $\alpha$ -,  $\beta$ - and  $\gamma$ -dispersions would be found in an idealized case [1]. The  $\alpha$ -dispersion, which appears at frequencies below a few kHz, is not easy to be measured

because of interference from artifactual electrode polarization effects. The relaxation process has not been well understood but could be originated from the displacement of counter ions surrounding charged membranes [21]. The  $\beta$ -dispersion is due to interfacial polarization, being mainly attributed to the existence of the insulating plasma membrane surrounding cells. This is apparent from the fact that the dispersion almost disappears after the membrane is disrupted or permeabilized by detergents [22]. The  $\gamma$ -dispersion that results from reorientation of water molecules lies above 1 GHz [23]. Between the  $\beta$ - and  $\gamma$ -dispersions there may be small dispersions that could be accounted for by relaxation of biopolymers and bound water.

Of the dielectric dispersions, our main concern is the  $\beta$ -dispersion and we will discuss what kind of information about cells and cellular components can be obtained from the  $\beta$ -dispersion in the next subsections.

### 2.1 Plasma membrane

The electrical properties of the plasma membrane may be the most important information obtained from the  $\beta$ -dispersion. Here, we first discuss the accuracy of the estimation of the membrane capacitance and conductance using the single-shell model that is composed of a spherical core of the complex permittivity  $\varepsilon_i^*$  and a shell of  $\varepsilon_m^*$ . Complex permittivity (or complex relative permittivity, more precisely) is defined as  $\varepsilon^* = \varepsilon - j\kappa/\omega\varepsilon_0$ , where  $\varepsilon$  is relative permittivity,  $\kappa$  conductivity,  $\omega$  angular frequency,  $\varepsilon_0$  the permittivity of vacuum and  $j=(-1)^{1/2}$ . The equivalent, homogeneous complex permittivity of the shell-sphere  $\varepsilon_p^*$  is given by Maxwell [24].

$$\varepsilon_p^* = \varepsilon_m^* \frac{2\varepsilon_m^* + \varepsilon_i^* - 2\nu(\varepsilon_m^* - \varepsilon_i^*)}{2\varepsilon_m^* + \varepsilon_i^* + \nu(\varepsilon_m^* - \varepsilon_i^*)}, \quad (1)$$

where  $\nu=(1-d/R)^3$ ,  $R$  is the outer radius of the shell-sphere and  $d$  is the thickness of the shell. The complex permittivity  $\varepsilon^*$  of the system in which the shell-spheres of  $\varepsilon_p^*$  are dispersed in a continuous medium of  $\varepsilon_a^*$  at volume fraction  $\Phi$  is given by Wagner's mixture equation [25]

$$\varepsilon^* = \varepsilon_a^* \frac{2\varepsilon_a^* + \varepsilon_p^* - 2\Phi(\varepsilon_a^* - \varepsilon_p^*)}{2\varepsilon_a^* + \varepsilon_p^* + \Phi(\varepsilon_a^* - \varepsilon_p^*)}. \quad (2)$$

#### <Fig. 1>

The membrane conductance  $G_m$  (defined as  $G_m=\kappa_m/d$ ) of the intact plasma membrane is usually lower than 100 S/m<sup>2</sup>; the membrane conductivity  $\kappa_m$  is below 10<sup>-6</sup> S/m and much lower than the medium conductivity  $\kappa_a$  and the cytoplasmic conductivity  $\kappa_i$ . The membrane thickness  $d$  is about 10 nm, and thus much smaller than the cell radius  $R$ . Assuming that  $\kappa_m/\kappa_a \ll 1$ ,  $\kappa_m/\kappa_i \ll 1$  and  $d/R \ll 1$ , Eqs.1 and 2 approximately provide one

dielectric relaxation of magnitude  $\Delta\epsilon$  [14].

$$\Delta\epsilon = \frac{9\Phi}{(2+\Phi)^2} \frac{RC_m}{\epsilon_0} \left[ 1 + RG_m \left( \frac{1}{\kappa_l} + \frac{1-\Phi}{(2+\Phi)\kappa_a} \right) \right]^{-2}, \quad (3)$$

where  $C_m$  is the membrane capacitance defined as  $C_m = \epsilon_m \epsilon_0 / d$ . When  $G_m \approx 0$ ,  $\Delta\epsilon$  is

$$\Delta\epsilon(G_m = 0) = \frac{9\Phi}{(2+\Phi)^2} \frac{RC_m}{\epsilon_0}. \quad (4)$$

To examine the effect of  $G_m$  on  $\Delta\epsilon$ , the  $\Delta\epsilon/\Delta\epsilon(G_m=0)$  is obtained dividing Eq.4 by Eq.3.

$$\frac{\Delta\epsilon}{\Delta\epsilon(G_m = 0)} = \left( 1 + \frac{3RG_m}{2\kappa_a} \right)^{-2} \approx 1 - 3 \frac{RG_m}{\kappa_a}, \quad (5)$$

where, for sake of simplicity, we suppose that  $\kappa_a = \kappa_l$  and  $\Phi \ll 1$ . When  $\kappa_a = 1$  S/m (the value is relevant to physiological saline solutions) and  $G_m = 1000$  S/m<sup>2</sup> (a much higher value for  $G_m$  of intact cells),  $\Delta\epsilon/\Delta\epsilon(G_m=0)$  is 0.985 for  $R=5$   $\mu$ m. Hence, we can reasonably assume  $G_m=0$  for intact cells of ordinary size and thus calculate the membrane capacitance  $C_m$  from the observed  $\Delta\epsilon$  using Eq.4 if the cell radius  $R$  and the volume fraction  $\Phi$  are given. The volume fraction is estimated from the values obtained for  $\kappa_l$  (the limiting conductivity of the suspension at low frequencies) and  $\kappa_a$  (the medium conductivity) using the following equation.

$$\Phi = \frac{2(1 - \kappa_l/\kappa_a)}{2 + \kappa_l/\kappa_a}. \quad (6)$$

This equation is derived from Eq.2 by assuming  $\kappa_p \ll \kappa_a$ . Instead of Eqs.4 and 6, alternative equations based on Hanai's mixture equation [26] are used, especially for concentrated cell suspensions [27,28].

$$\Delta\epsilon = \frac{3}{2} \left[ 1 - (1 - \Phi)^{\frac{3}{2}} \right] \frac{RC_m}{\epsilon_0}, \quad (7)$$

$$\Phi = 1 - \left( \frac{\kappa_l}{\kappa_a} \right)^{\frac{2}{3}}. \quad (8)$$

The membrane capacitance estimated from Eq.4 or Eq.7, however, is not "specific" membrane capacitance, but depends on the degree of membrane ramification (microvilation, enfolding, etc.). Indeed, the membrane capacitance estimated for cultured cells from Eq.4 increased with increasing the degree of membrane ramification caused by osmotic perturbation [29,30].

We have assumed that the membrane capacitance is independent of frequency. Is this assumption reasonable? The basic structure of the plasma membrane is a lipid bilayer that has a hydrophobic core layer and a hydrophilic surface layer. The two-layer

system is expected to show one dielectric dispersion due to interfacial polarization. Coster et al. [31] found that the membrane capacitance of lipid bilayers showed a small dielectric dispersion at low frequencies below a few Hz. The membrane capacitance that was measured for some non-excitable cells (erythrocytes, HeLa and myeroma) using the patch pipette was almost unchanged between 1 Hz and 1 kHz [28,32]. On the contrary, frequency dependence of the membrane capacitance was found for muscle cells and their culture cells, being due to the presence of the extensive enfolding of surface membrane, namely T-tubules [33-35]. Nerve membranes also showed frequency-dependent membrane capacitance, which was explained in terms of the ionic flow related to membrane excitability [36,37]. Frequency dependence of the membrane capacitance could also arise from either the orientation of polar molecules or the migration of charged molecules in the membrane.

## 2.2 External matrix

Bacteria, yeast and plant cells have external matrices (cell wall) outside the plasma membrane. For analysis of dielectric behavior of such cells, the single-shell model is not available unless the electrical properties of the cell wall are the same as those of the external medium. This is also the case for animal cells in the medium of a low ionic strength, where the counterion cloud in the neighborhood of the charged surface of the plasma membrane forms a conducting layer. An electrical model for these cells might be represented by the "two-shell" model in which a sphere is covered with two concentric shells (Fig.2b) [38-40]. The effective complex permittivity of the cell  $\epsilon_c^*$  is

$$\epsilon_c^* = \epsilon_w^* \frac{2\epsilon_w^* + \epsilon_p^* - 2w(\epsilon_w^* - \epsilon_p^*)}{2\epsilon_w^* + \epsilon_p^* + w(\epsilon_w^* - \epsilon_p^*)}, \quad (9)$$

where  $\epsilon_w^*$  is the complex permittivity of the cell wall,  $\epsilon_p^*$  is given by Eq.1,  $w=(1-d_w/R_c)$ ,  $d_w$  is the wall thickness and  $R_c$  is the outer cell radius. Substituting  $\epsilon_c^*$  for  $\epsilon_p^*$  in Eq.2 we obtain the complex permittivity of the cell suspension. Assuming that  $G_m=0$  and  $d/R \ll 1$  the low-frequency limits of the relative permittivity and conductivity of the suspension are

$$\epsilon_1 \approx \frac{9 \times 9 C_m R w \Phi}{\epsilon_0 \left[ (2+w)(2+\Phi) + 2(1-w)(1-\Phi) \frac{\kappa_w}{\kappa_a} \right]^2}, \quad (10)$$

$$\frac{\kappa_l}{\kappa_a} = \frac{2(2+w)(1-\Phi) + 2(1-w)(1+2\Phi) \frac{\kappa_w}{\kappa_a}}{(2+w)(2+\Phi) + 2(1-w)(1-\Phi) \frac{\kappa_w}{\kappa_a}} \quad (11)$$

The  $\varepsilon_l$  and  $\kappa_l$  markedly depend on the  $\kappa_w/\kappa_a$  ratio as shown in Fig.3a. The presence of the wall also affects the shape of the dielectric spectrum; a two-step curve composed of two relaxation terms is obtained for  $\kappa_w/\kappa_a \neq 1$ , whereas there is a single relaxation for  $\kappa_w/\kappa_a = 1$  (Fig.3b).

Since the conductivity of the cell wall is not known, the volume fraction  $\Phi$  cannot be calculated from Eq.11. However, once the volume fraction is determined by non-electrical methods such as the dye exclusion method with large marker molecules that do not penetrate into the wall, we can estimate the wall conductivity from Eq.11 and the membrane capacitance from Eq.10 if  $w$  is known. The conductivity of the wall of bacteria and yeast cells was determined by varying ionic strength of the external medium [38,41,42]. The relationships between the wall conductivity and the ionic strength were similar to that for ion-exchange resins of fixed charges. The  $\kappa_w/\kappa_a$  was higher than unity at low  $\kappa_a$  and decreased beyond unity with increasing  $\kappa_a$ . This is because mobile ions distribute between the charged matrix and the external medium following the Donnan equilibrium and the volume ratio of the space available for mobile ions in the wall is less than unity.

### <Figs. 2 and 3>

#### 2.3 Relaxation of molecules in cytoplasm

Protein and DNA solutions show dielectric relaxation due to molecular orientation and counterion redistribution, respectively. Can we obtain such information from the dielectric spectra of cell suspensions? It depends on the magnitude  $\Delta\varepsilon$  and the characteristic frequency  $f_c$  of the dielectric dispersion due to interfacial polarization, which are essentially predicted from the single-shell model. At lower frequencies than the  $f_c$ , the information on the cytoplasm is hardly obtained, because the electric field strength in the cytoplasm is very small owing to the insulating plasma membrane. The information of the cytoplasm is obtainable at higher frequencies than the  $f_c$ , where the insulating membrane is short-circuited. The characteristic frequency is given by [14]

$$\tau = \frac{1}{2\pi f_c} = RC_m \left( \frac{1}{\kappa_i} + \frac{1-\Phi}{2+\Phi} \frac{1}{\kappa_a} \right), \quad (12)$$

where  $\kappa_i$  and  $\kappa_a$  are the conductivity of the cytoplasm and the external medium, respectively. When  $\kappa_i$  and  $\kappa_a$  are 1 S/m (the value corresponds to physiological saline



solutions),  $f_c$  is about 1 MHz for  $R$  of 5  $\mu\text{m}$ . The value is close to that of dielectric dispersion of protein solutions (1-10MHz) and much higher than that of the low-frequency dispersion of DNA solutions (1-100 Hz). Therefore, it is hard to study the biological macromolecules in intact cells under physiological conditions. However, if  $\kappa_i$  and  $\kappa_a$  are lowered or the plasma membrane was permeabilized with chemical reagents such as detergents and ionophores, dielectric dispersion of proteins might be obtainable.

#### 2.4 Intracellular structure

A simple model like the single-shell model may represent mammalian erythrocytes that have no intracellular organelles. Indeed, spherical erythrocytes that were swollen in moderate hypotonic media showed one dielectric dispersion, which was fully simulated by the single-shell model [43,44]. However, the cytoplasm of most biological cell types has organelles and membranous structure, which are polarized owing to interfacial polarization. The polarization may cause additional dielectric dispersions besides the main dielectric dispersion due to the plasma membrane. In order to analyze the dielectric spectra of such cells, various composite cell models including intracellular structure have been proposed (Fig.4). Irimajiri et al. [45] have developed the theory of the "double-shell" model (Fig.1a), and first applied it to lymphoma cells that possess a sizable nucleus. The double-shell model also successfully simulated the dielectric spectra of isolated mitochondria with double membranes [19], lymphocytes [30,43,46], budding yeast cells having a vacuole in the cytoplasm [40, 47]. Plant protoplasts isolated from leaves have a large vacuole and a thin cytoplasmic layer containing chloroplasts. The dielectric spectra of plant protoplasts were composed of two large dispersions, and one small dispersion at higher frequencies. For the dispersion curves, the double-shell model including vesicles (Fig.1b) gave a better simulation than the double-shell model [48]. In this case, the inner-shell sphere corresponds to the vacuole and the vesicles to the chloroplasts.

#### <Fig.4>

#### 2.5 Cell shape

The dielectric spectra of cell suspensions considerably depend on cell shape. Non-spherical cells are represented by the shell-ellipsoid model, in which an ellipsoid is covered with a confocal shell (Fig.4c). The dielectric theory of the shell-ellipsoid model is more complicated than that of spherical models because the effective complex permittivity of the shell-ellipsoid  $\epsilon_p^*$  has three components along its three axes [49-52]. In the case of an ellipsoid of rotation with two different axes, the dielectric dispersion of the dilute suspension of randomly oriented cells is approximately represented by a sum

of two subdispersions corresponding to the two components of  $\varepsilon_p^*$ .

$$\varepsilon^* = \varepsilon_h + \frac{\Delta\varepsilon_1}{1 + j\omega\tau_1} + \frac{\Delta\varepsilon_2}{1 + j\omega\tau_2} + \frac{\kappa_i}{j\omega\varepsilon_0}, \quad (13)$$

where  $\Delta\varepsilon$  is the magnitude of dispersion,  $\tau$  the relaxation time and subscripts 1 and 2 refer to the dispersions due to the two components of  $\varepsilon_p^*$  along the rotational axis and the other axis, respectively. The  $\Delta\varepsilon_1/\Delta\varepsilon_2$  and the  $\tau_1/\tau_2$  are simply represented by the following equations [53].

$$\frac{\Delta\varepsilon_1}{\Delta\varepsilon_2} = \frac{(1+A)^2}{16A(1-A)}, \quad (14)$$

$$\frac{\tau_1}{\tau_2} = \frac{(1+A)(1-A) + A(1+A)\kappa_i/\kappa_a}{2[A(1+A) + A(1-A)\kappa_i/\kappa_a]}. \quad (15)$$

The depolarization factor  $A$  along the rotational axis is given by

$$A = -\frac{1}{q^2 - 1} + \frac{q}{(q^2 - 1)^{3/2}} \ln[q + (q^2 - 1)^{1/2}], \quad (\text{for prolate spheroids}) \quad (16)$$

$$A = \frac{1}{1 - q^2} - \frac{q}{(1 - q^2)^{3/2}} \cos^{-1} q, \quad (\text{for oblate spheroids}) \quad (17)$$

where  $q = a/b$ ,  $a$  is the semiaxis along the rotational axis and  $b$  is the other semiaxis. Figure 5 shows the  $A$ ,  $\Delta\varepsilon_1/\Delta\varepsilon_2$  and  $\tau_1/\tau_2$  calculated from Eqs.14-17. The  $\tau_1/\tau_2$  increases crossing over unity at  $q=1$  with increasing the axial ratio. The  $\Delta\varepsilon_1/\Delta\varepsilon_2$  is roughly proportional to  $q$  for prolate spheroids ( $q>1$ ), whereas it varies inversely as  $q$  for oblate spheroids ( $q<1$ ).

As non-spherical cells, *E.coli* of rod-like shape, erythrocyte of biconcave shape, budding yeast as doublet, and fission yeast of rod-like shape have been studied by dielectric spectroscopy [6,51,53, 54]. All these cells whose shape is represented as a body of rotation showed dielectric dispersion that was decomposed into two subdispersions as expected from the theory based on the shell-spheroid model. The theory, however, provides rather qualitative explanations and there are some discrepancies between the theoretical calculations and the measured data. For a quantitative explanation, numerical calculation methods with cell models of more realistic shape have been developed [55,56].

<Fig.5>

### 3. Monitoring of cells under physiological conditions

Rapid and automated instruments for dielectric spectroscopy encourage us to investigate dynamic behavior of biological cells under physiological conditions although there is still a serious problem to be solved for practical applications. The

detailed analyses described in the above section were made for the data obtained under rather artificial conditions (i.e., in relatively low salt media and at high cell concentrations) to avoid errors due to electrode polarization. For special samples such as whole blood in which the volume fraction of erythrocytes is very high (~40%), the conventional two-electrode method (Fig.6a) can be used without serious errors due to electrode polarization, cf., monitoring of rouleaux formation by erythrocytes in human blood [9]. However, in cell culture where the volume fraction of cells is a few percents at most, the dielectric dispersion of cell suspensions is appreciably masked by the electrode polarization effect. Hence, a prerequisite for successful measurements is how to eliminate the electrode polarization effect. To solve this problem, Harris et al. [10] employed the four-electrode method (Fig.6b), in which electrodes for current supply are separated from electrodes for voltage detection [57, 58]. Recently, an alternative technique has been developed by Wakamatsu [59], which uses an inductive probe consisting of two concentric toroidal coils instead of metal electrodes (Fig.6c). The technique is regarded as an electrode-less method based on electromagnetic induction. In the next subsections, the examples monitored by the electromagnetic induction method are described.

### <Fig.6>

#### 3.1 Bacteria and yeast growth in culture

The relative permittivity of the culture medium inoculated with *E. coli* or yeast was monitored during its non-synchronous and synchronous growth. With either the single-shell model or the ellipsoidal model, the relative permittivity  $\epsilon$  of a cell suspension is proportional to the cell concentration. Since the cell concentration increases exponentially in cell growth and levels off at the stationary phase, the relative permittivity of the culture broth would show an exponential increase followed by a plateau. Figure 7 shows the time course of the increment in relative permittivity  $\delta\epsilon$  probed at 0.17 MHz. For non-synchronous growth of *E. coli* and yeast, an exponential increase in  $\delta\epsilon$  was found as expected. On the other hand, for synchronized culture of yeast, the  $\delta\epsilon$  periodically changed in the early growth phase. The cycle of  $\delta\epsilon$  corresponds to one cell division cycle, being explained as follows. The increase in  $\delta\epsilon$  is due to the increase in both cell volume and length, and the decrease in  $\delta\epsilon$  is due to the shape change in cell separation (mitosis). This was confirmed both by a theoretical simulation [52] and by experimental evidence [54,60].

### <Fig.7>

#### 3.2 Fermentation in brewery

Dielectric spectroscopy have been applied to monitoring of fermentation processes in beer and whisky brewery [61]. The monitoring provides integrated information on yeast cell properties, such as cell concentration, changes in cell volume and cell shape, and cell viability. The information is important for analyzing and controlling the fermentation processes. In whisky fermentation, the changes in relative permittivity of the fermenting wort showed four distinct phases. In the first phase, the relative permittivity  $\epsilon$  increased owing to the increase in cell number. After the increase in cell number stopped, an increase in  $\epsilon$  was still observed (the second phase), being explained in terms of the increase in cell volume. In the third phase, there was a decrease in  $\epsilon$  due to both of the decrease in cell volume and the increase in number of dead cells. In the last phase the relative permittivity became the same value as that of the medium, indicating that most cells were dead because dead cells with leaky plasma membranes are not polarized in ac fields. In beer fermentation, the dielectric monitoring suggested that most cells were alive all over the fermentation and that the initial cell growth was highly synchronized.

#### 4. Single-cell analysis

"Single-cell" approaches would be more straightforward than the 'suspension' method that estimates the average electrical properties of cells from the dielectric spectrum of their suspension using an appropriate mixture equation. An application of dielectric spectroscopy to single cells was first carried out with eggs by Cole and Guttman [62]. Since the single-cell analysis need not to take into account electrical interactions between cells, Wagner's mixture equation can be used for the analysis. Indeed, Pauly-Schwan's equation based on Wagner's mixture equation excellently simulated the dielectric behavior of single spherical bilayer membranes [63] and single microcapsules [64] as models for biological cells. The measurement technique used for single eggs and cell models (Fig.8a), however, is difficult to apply to cells of ordinary size ( $\sim 10 \mu\text{m}$ ). Instead, electromechanical methods can be used to investigate electrical properties of such single cells [65], utilizing their motional responses to applied ac fields, namely dielectrophoresis [66-69] (Fig.8b) and electrorotation [70,71] (Fig.8c). An alternative approach is the use of the "scanning dielectric microscope" (SDM) that can image local relative permittivity and conductivity sensed using a scanning fine probe [72] (Fig.8c).

<Fig.8>

##### 4.1 Electromechanical techniques

When subjected to an ac field, a cell is polarized and has a induced dipole moment. The cell with the induced dipole moment experiences forces and torques in the ac field.

Hence, the motional response of a single cell, measured as a function of frequency of the ac field, provides the dielectric spectrum of the cell through appropriate theories. The electrorotation measures the rotational rate of a cell in a rotating electric field that is generated with four electrodes arranged as shown in Fig.8b [70,71]. The rotational rate is proportional to the imaginary part of the dipole moment of the cell induced by the electric field. The dielectrophoresis uses heterogeneous ac fields produced using asymmetric electrodes such as the electrode system shown in Fig.8c [68,69]. A cell experiences force in the heterogeneous ac field and migrates along the gradient of the electric field strength. The measurement of the dielectrophoretic force provides the real part of the induced dipole moment of the cell.

#### 4.2 Scanning dielectric microscopy

The scanning dielectric microscopy (SDM) was developed for imaging the permittivity and conductivity of fine particles in an aqueous medium over a wide frequency range. Figure 8d shows a schematic view of the SDM. The coaxial probe consisting of an inner probing electrode and an outer guard electrode is scanned over a sample on a plate electrode. Dielectric measurements are made based on the three-terminal method that is effective to eliminate the fringing field and to restrict the measurement to a small area. The SDM, therefore, would enable us to examine dielectric properties of individual biological cells, although its application to date is limited to low-conductive media. This method has been applied to single sub-mm size PS microcapsules [73] and cultured cells [74].

#### Acknowledgments

I thank Dr. A Irimajiri for his helpful comments. This work was supported in part by Ministry of Education, Science and Culture (Grants 12680829 and 09555252).

#### References

- [1] H.P. Schwan, Electrical Properties of Tissue and Cell Suspensions, in: J.H. Lawrence and C.A. Tobias (Eds.), *Advances in Biological and Medical Physics*, Vol. 5, New York, 1957, p.147.
- [2] K.S. Cole, *Membranes, Ions and Impulses*, University of California Press, Berkeley and Los Angeles, 1968.
- [3] T. Hanai, Electrical Properties of Emulsions, in: P. Sherman (Ed.), *Emulsion Science*, Academic Press, London and New York, 1968, p. 353.
- [4] R. Pethig and D.B. Kell, *Phys. Med. Biol.*, 32 (1987) 933.
- [5] K.R. Foster and H.P. Schwan, Dielectric properties of tissues, in: C. Polk and E.



- Postow (Eds.) Handbook of Biological Effects of Electromagnetic Fields, CRC Press, Boca Raton, 1996, p. 25.
- [6] K. Asami, Dielectric Relaxation Spectroscopy of Biological Cell Suspensions, in V.A. Hackley and J. Texter (Eds.), Handbook on Ultrasonic and Dielectric Characterization Techniques for Suspended Particulates, The American Ceramic Society, Westerville, 1998, p.333.
  - [7] G.H. Markx, C.L. Davey, *Enzyme Microb. Technol.* 25 (1999) 161.
  - [8] K. Asami, T. Hanai, *Colloid Polym. Sci.*, 270 (1992) 78.
  - [9] A. Irimajiri, M. Ando, R. Matsuoka, T. Ichinowatari, S. Takeuchi, *Biochim. Biophys. Acta*, 1290 (1996).
  - [10] C.M. Harris, R.W. Todd, S.J. Bungard, R.W. Lovitt, G. Morris, D.B. Kell, *Enzyme Microb. Technol.*, 9 (1987) 181.
  - [11] K. Asami, E. Gheorghiu, T. Yonezawa, *Biophysical J.* 76 (1999) 3345
  - [12] V. Raicu, T. Saibara, H. Enzan, A. Irimajiri, *Bioelectrochem. Bioenerg.* 47 (1998) 333.
  - [13] K. Asami, A. Irimajiri, *Phys. Med. Biol.* 45 (2000) 3285.
  - [14] H. Pauly, H.P. Schwan, *Z. Naturforsch.*, 14b (1959) 125.
  - [15] H. Pauly, L. Packer, H.P. Schwan, *J. Biophys. Biochem. Cytol.* 7 (1960) 589.
  - [16] H. Pauly, L. Packer, *J. Biophys. Biochem. Cytol.* 7 (1960) 603.
  - [17] A. Irimajiri, T. Hanai, A. Inouye, *Biophys. Struct. Mechanism* 1 (1975) 273.
  - [18] K. Asami, A. Irimajiri, T. Hanai, N. Shiraishi, K. Utsumi, *Biochim. Biophys. Acta* 778 (1984) 559.
  - [19] K. Asami, A. Irimajiri, *Biochim. Biophys. Acta* 778 (1984) 570.
  - [20] S. Takashima, *Electrical Properties of Biopolymers and Membranes*, Adam Hilger, Bristol, England, 1989.
  - [21] G. Schwarz, *J. Phys. Chem.*, 66 (1962) 2636.
  - [22] K. Asami, T. Hanai, N. Koizumi, *J. Membrane Biol.* 34 (1977) 145.
  - [23] J.B. Hasted, *Aqueous Dielectrics*, Chapman and Hall, London, 1973.
  - [24] J.C. Maxwell, *Treatise on Electricity and Magnetism*, Clarendon Press, Oxford, London, 1891.
  - [25] K.W. Wagner, *Archiv fur Electrotechnik.*, 2 (1914) 371.
  - [26] T. Hanai, *Kolloid Z.*, 171 (1960) 23.
  - [27] T. Hanai, K. Asami, N. Koizumi, *Bull. Inst. Chem. Res., Kyoto Univ.*, 57 (1979) 297.
  - [28] K. Asami, Y. Takahashi, S. Takashima, *Biophys. J.* 58 (1990) 143.
  - [29] A. Irimajiri, K. Asami, T. Ichinowatari, Y. Kinoshita, *Biochim. Biophys. Acta*, 896 (1987) 214.

- [30] F. Bordi, C. Cametti, R. Rosi, A. Calcabrini, *Biochim. Biophys. Acta* 1153 (1993) 77.
- [31] H.G.L. Coster, T.C. Chilcott, A.C.F. Coster, *Bioelectrochem. Bioenerg.* 40 (1996) 79.
- [32] S. Takashima, K. Asami, Y. Takahashi, *Biophys. J.*, 54 (1988) 995.
- [33] R.S. Eisenberg, P.W. Gage, *Science* 158 (1967) 1700.
- [34] S. Takashima, *Pflugers Archiv.* 403 (1985) 197.
- [35] K. Asami, S. Takashima, *Biochim. Biophys. Acta* 1190 (1994) 129.
- [36] S. Takashima, *Biophys. J.* 26 (1979) 133.
- [37] H.M. Fishman, D. Poussart, L.E. Moore, *J. Membrane Biol.* 50 (1979) 43.
- [38] E.L. Carstensen, H.A. Cox, W.B. Mercer, L.A. Natale, *Biophys. J.* 5 (1965) 289.
- [39] K. Asami, T. Hanai, N. Koizumi, *J. Membrane Biol.* 28 (1976) 169.
- [40] K. Asami, T. Yonezawa, *Biophys. J.*, 71 (1996) 2192.
- [41] E.L. Carstensen, R.E. Marquis, *Biophys. J.* 8 (1968) 536.
- [42] K. Asami, *Bull. Inst. Chem. Res., Kyoto Univ.* 55 (1977) 394.
- [43] K. Asami, Y. Takahashi, S. Takashima, *Biochim. Biophys. Acta*, 1010 (1989) 49.
- [44] R. Lisin, B.Z. Ginzburg, M. Schlesinger, Y. Feldman, *Biochim. Biophys. Acta*, 1280 (1996) 34.
- [45] A. Irimajiri, Y. Doida, T. Hanai, A. Inouye, *J. Membr. Biol.*, 38 (1978) 209.
- [46] Y. Polevaya, I. Ermolina, M. Schlesinger, B.Z. Ginzburg, Y. Feldman, *Biochim. Biophys. Acta*, 1419 (1999) 257.
- [47] V. Raicu, G. Raicu, G. Turcu, *Biochim. Biophys. Acta*, 1274 (1996) 143.
- [48] K. Asami, T. Yamaguchi, *Biophys. J.*, 63 (1992) 1493.
- [49] H. Fricke, *J. Phys. Chem.* 57 (1953) 934.
- [50] K. Asami, T. Hanai, N. Koizumi, *Jpn. J. Appl. Phys.*, 19 (1980) 359.
- [51] K. Asami, T. Hanai, N. Koizumi, *Biophys. J.*, 31 (1980) 215-228.
- [52] K. Asami and T. Yonezawa, *Biochim. Biophys. Acta*, 1245 (1995) 317.
- [53] K. Asami, *Biochim. Biophys. Acta* 1472 (1999) 137.
- [54] K. Asami, E. Gheorghiu, T. Yonezawa, *Biochim. Biophys. Acta* 1381 (1998) 234.
- [55] D. Vrinceanu, E. Gheorghiu, *Bioelectrochem. Bioenerg.*, 40 (1996) 167.
- [56] K. Sekine, *Bioelectrochem.* 52 (2000) 1.
- [57] H.P. Schwan, *Biophysik*, 3 (1966) 181.
- [58] H.P. Schwan, C.D. Ferris, *Rev. Sci. Instrum.*, 39 (1968) 481.
- [59] H. Wakamatsu, *Hewlett-Packard Journal*, 48 (1997) 37.
- [60] K. Asami, K. Takahashi, K. Shirahige, *Yeast* 16 (2000) 1359.
- [61] K. Asami, T. Yonezawa, H. Wakamatsu and N. Koyanagi, *Bioelectrochem. Bioenerg.*, 40 (1996).

- [62] K.S. Cole, R. M. Guttman, 25 (1942) 765.
- [63] K. Asami and A. Irimajiri, *Biochim. Biophys. Acta*, 769 (1984) 370.
- [64] K. Asami and K.S. Zhao, *Colloid Polym. Sci.*, 272 64.
- [65] T.B. Jones, *Electromechanics of Particles*, Cambridge University Press, 1995.
- [66] H.A. Pohl, *Dielectrophoresis*, Cambridge University Press, London, 1978.
- [67] R. Pethig, Y. Huang, X. Wang, J.P.H. Burt, *J. Phys. D: Appl. Phys.* 24 (1992) 881.
- [68] K.V.I.S. Kaler, T.B. Jones, *Biophys. J.*, 57 (1990) 173.
- [69] K.V.I.S. Kaler, J.P. Xie, T.B. Jones, R. Paul, *Biophys. J.*, 63 (1992) 58.
- [70] W.M. Arnold, U. Zimmermann, *Z. Naturforsch.*, 37c (1982) 908.
- [71] G. Fuhr, J. Gimsa, R. Glaser, *Studia Biophys.* 108 (1985) 149.
- [72] K. Asami, *Meas. Sci. Technol.*, 5 (1994) 589.
- [73] K. Asami, *Colloid Polym. Sci.* 276 (1998) 373.
- [74] K. Asami, *Colloid Polym. Sci.* 273 (1995) 1095.
- [75] K. Asami, *Colloid Polym. Sci.* 274 (1996) 1095.
- [76] K. Asami, *Colloid Polym. Sci.* 275 (1997) 1095.
- [77] K. Asami, *Colloid Polym. Sci.* 276 (1998) 373.
- [78] K. Asami, *Colloid Polym. Sci.* 277 (1999) 1095.
- [79] K. Asami, *Colloid Polym. Sci.* 278 (2000) 1095.
- [80] K. Asami, *Colloid Polym. Sci.* 279 (2001) 1095.
- [81] K. Asami, *Colloid Polym. Sci.* 280 (2002) 1095.
- [82] K. Asami, *Colloid Polym. Sci.* 281 (2003) 1095.
- [83] K. Asami, *Colloid Polym. Sci.* 282 (2004) 1095.
- [84] K. Asami, *Colloid Polym. Sci.* 283 (2005) 1095.
- [85] K. Asami, *Colloid Polym. Sci.* 284 (2006) 1095.
- [86] K. Asami, *Colloid Polym. Sci.* 285 (2007) 1095.
- [87] K. Asami, *Colloid Polym. Sci.* 286 (2008) 1095.
- [88] K. Asami, *Colloid Polym. Sci.* 287 (2009) 1095.
- [89] K. Asami, *Colloid Polym. Sci.* 288 (2010) 1095.
- [90] K. Asami, *Colloid Polym. Sci.* 289 (2011) 1095.
- [91] K. Asami, *Colloid Polym. Sci.* 290 (2012) 1095.
- [92] K. Asami, *Colloid Polym. Sci.* 291 (2013) 1095.
- [93] K. Asami, *Colloid Polym. Sci.* 292 (2014) 1095.
- [94] K. Asami, *Colloid Polym. Sci.* 293 (2015) 1095.
- [95] K. Asami, *Colloid Polym. Sci.* 294 (2016) 1095.
- [96] K. Asami, *Colloid Polym. Sci.* 295 (2017) 1095.
- [97] K. Asami, *Colloid Polym. Sci.* 296 (2018) 1095.
- [98] K. Asami, *Colloid Polym. Sci.* 297 (2019) 1095.
- [99] K. Asami, *Colloid Polym. Sci.* 298 (2020) 1095.
- [100] K. Asami, *Colloid Polym. Sci.* 299 (2021) 1095.
- [101] K. Asami, *Colloid Polym. Sci.* 300 (2022) 1095.
- [102] K. Asami, *Colloid Polym. Sci.* 301 (2023) 1095.
- [103] K. Asami, *Colloid Polym. Sci.* 302 (2024) 1095.
- [104] K. Asami, *Colloid Polym. Sci.* 303 (2025) 1095.

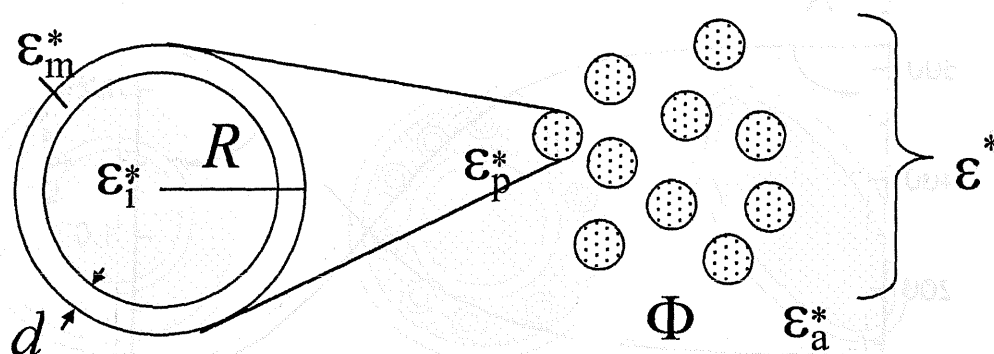


**Fig.1** Single-shell model for membrane-bounded spherical cells.  $\epsilon_i^*$ ,  $\epsilon_m^*$  and  $\epsilon_a^*$  are the complex permittivities of the inner phase, the membrane, and the external medium.  $R$  the outer radius of the shell-sphere and  $d$  is the membrane thickness.  $\epsilon^*$  is the complex permittivity of the suspension containing shell-spheres of  $\epsilon_p^*$  at volume fraction  $\Phi$ .

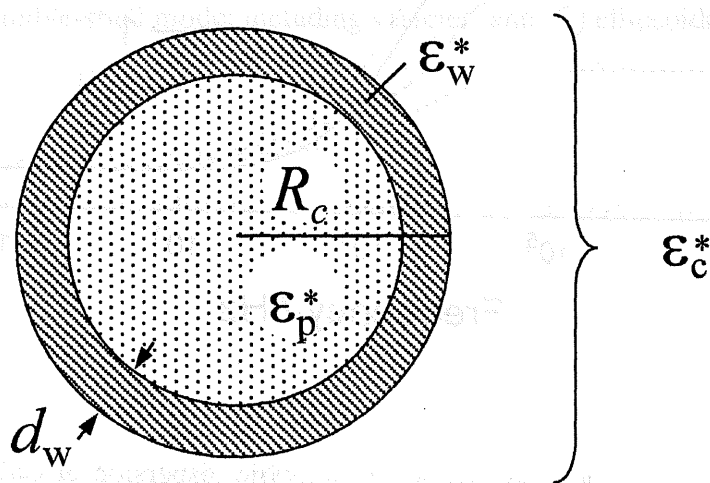


**Fig.2** Two-shell model for wall-bounded cells.  $\epsilon_c^*$  is the equivalent complex permittivity of the whole sphere,  $\epsilon_p^*$  the equivalent complex permittivity of the membrane-bounded sphere,  $\epsilon_w^*$  the complex permittivity of the wall,  $d_w$  the wall thickness and  $R_c$  the outer radius of the sphere.

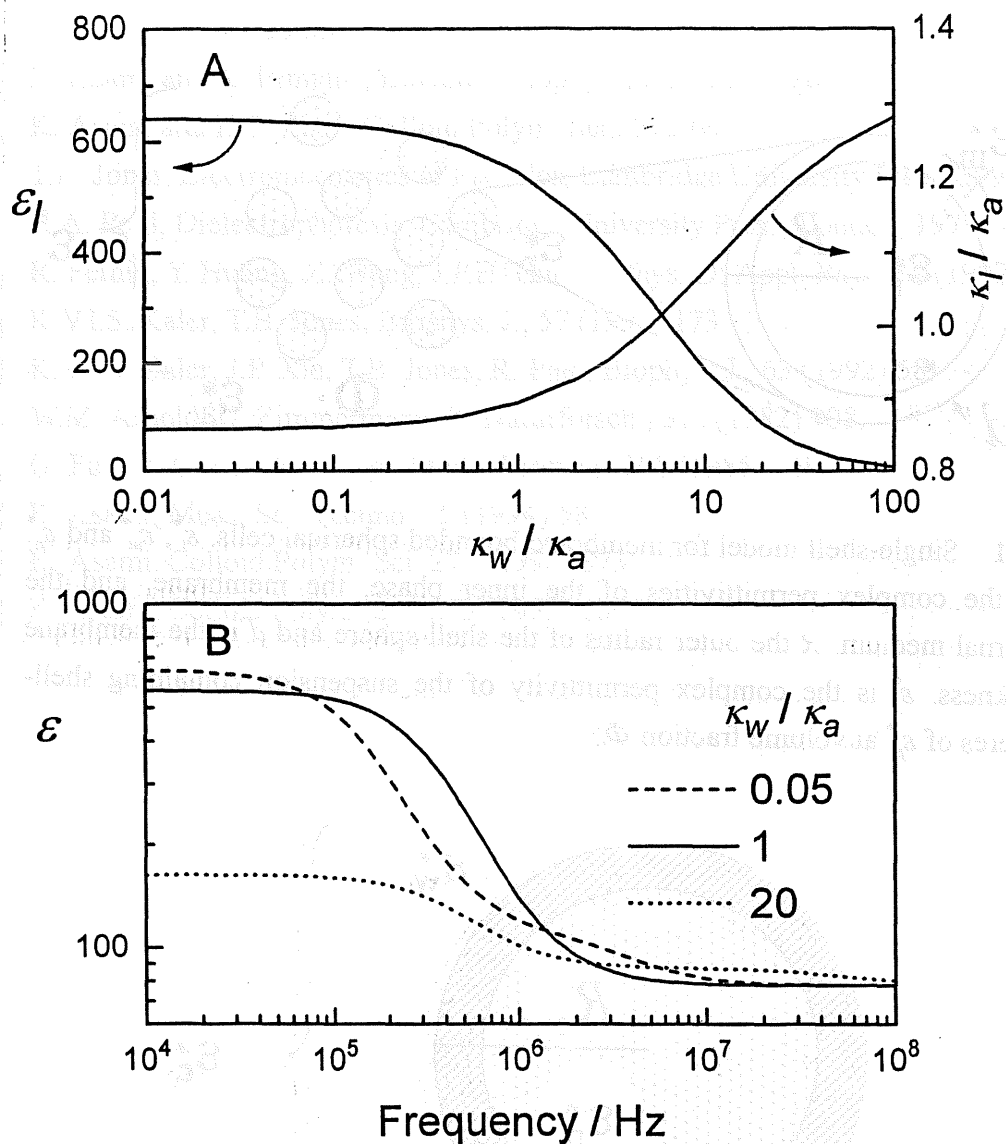


**Fig.3** Effects of wall conductivity on dielectric dispersion of cell suspension, which were simulated using the two-shell model. (A) The low-frequency limits of relative permittivity  $\epsilon_l$  and conductivity  $\kappa_l$  calculated from Eqs.10 and 11 are plotted for the ratio of the wall conductivity  $\kappa_w$  to the medium conductivity  $\kappa_a$ . (B) The dielectric dispersion curves were calculated for  $\kappa_w/\kappa_a=0.05, 1, 20$ . The parameter values used are:  $\epsilon_i=60$ ,  $\epsilon_w=60$ ,  $\epsilon_a=80$ ,  $\kappa_i=0.1 \text{ Sm}^{-1}$ ,  $\kappa_a=0.1 \text{ Sm}^{-1}$ ,  $R=5 \text{ }\mu\text{m}$ ,  $d_m=7 \text{ nm}$ ,  $d_w=0.5 \text{ }\mu\text{m}$ ,  $\Phi=0.1$ .



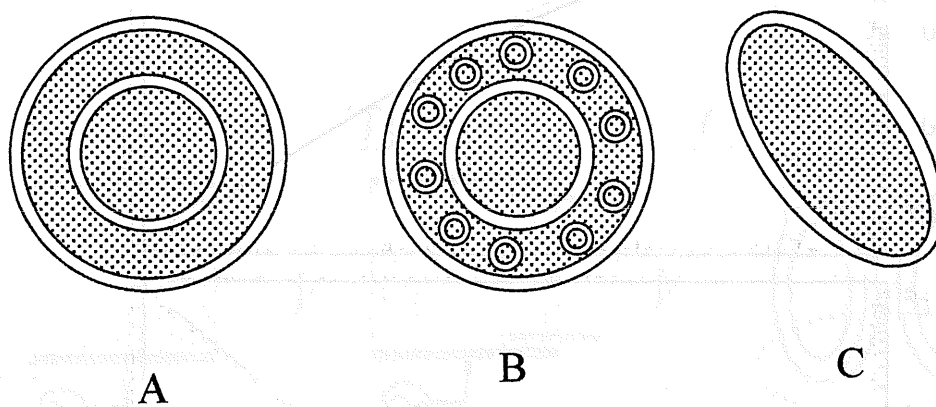


**Fig.4** Composite cell models and an ellipsoidal cell model. (A) Double-shell model, (B) double-shell model including vesicles, and (C) ellipsoidal model.

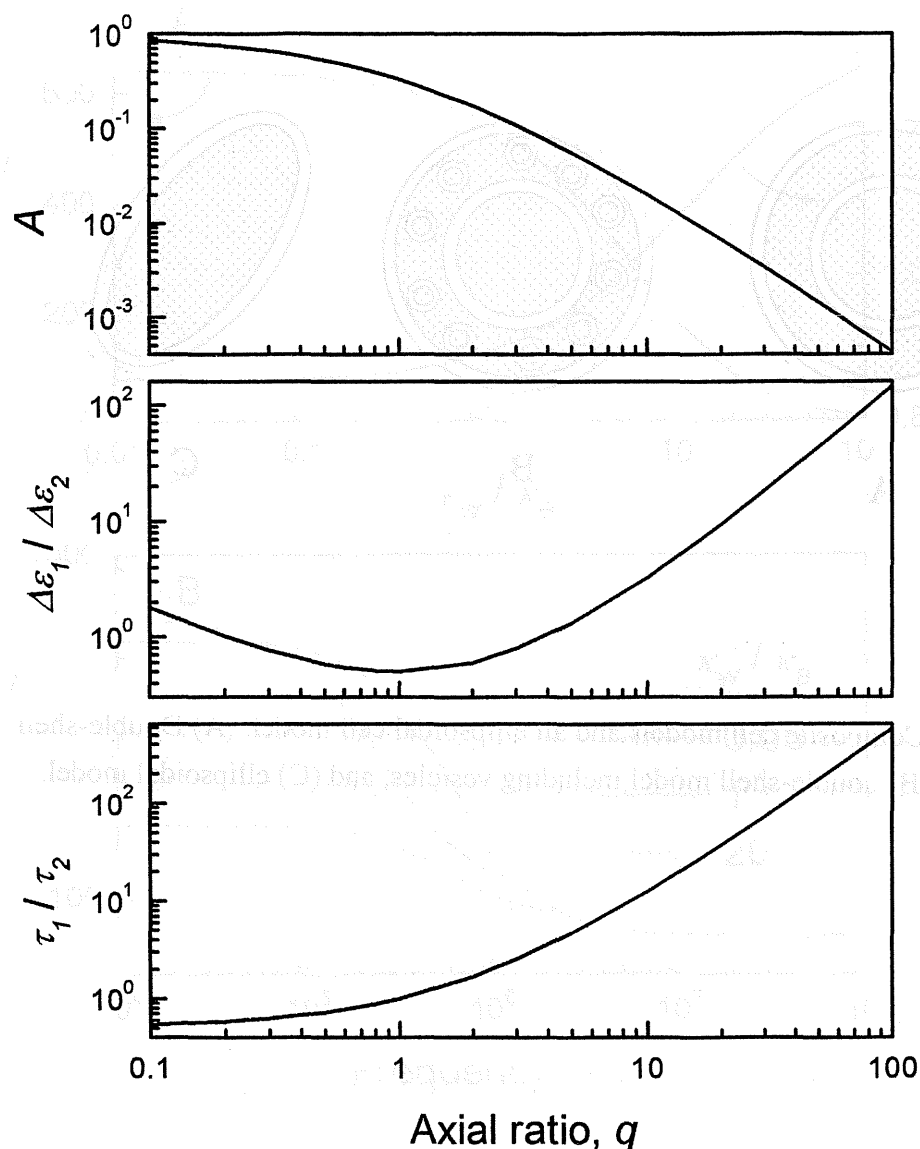


**Fig.5** Effects of cell shape on dielectric dispersion of cell suspension, which were simulated using the shell-spheroid model. (A) The depolarization factor  $A$  calculated from Eqs.16 and 17, (B) the  $\Delta\epsilon_1/\Delta\epsilon_2$  ratio calculated from Eq.14. and (C) the  $\tau_{e1}/\tau_{e2}$  ratio calculated from Eq.15 are plotted for the axial ratio  $q$  of shell-spheroids.

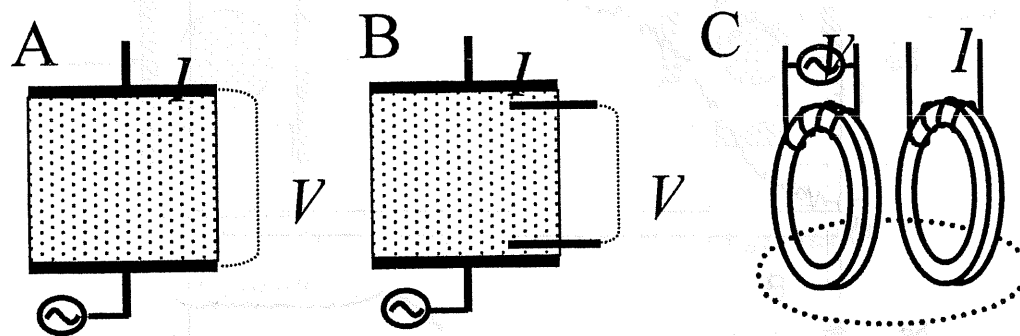


**Fig.6** Methods used for dielectric monitoring. (A) Two-electrode method, (B) four-electrode method, and (C) electromagnetic induction method (non-electrode method).

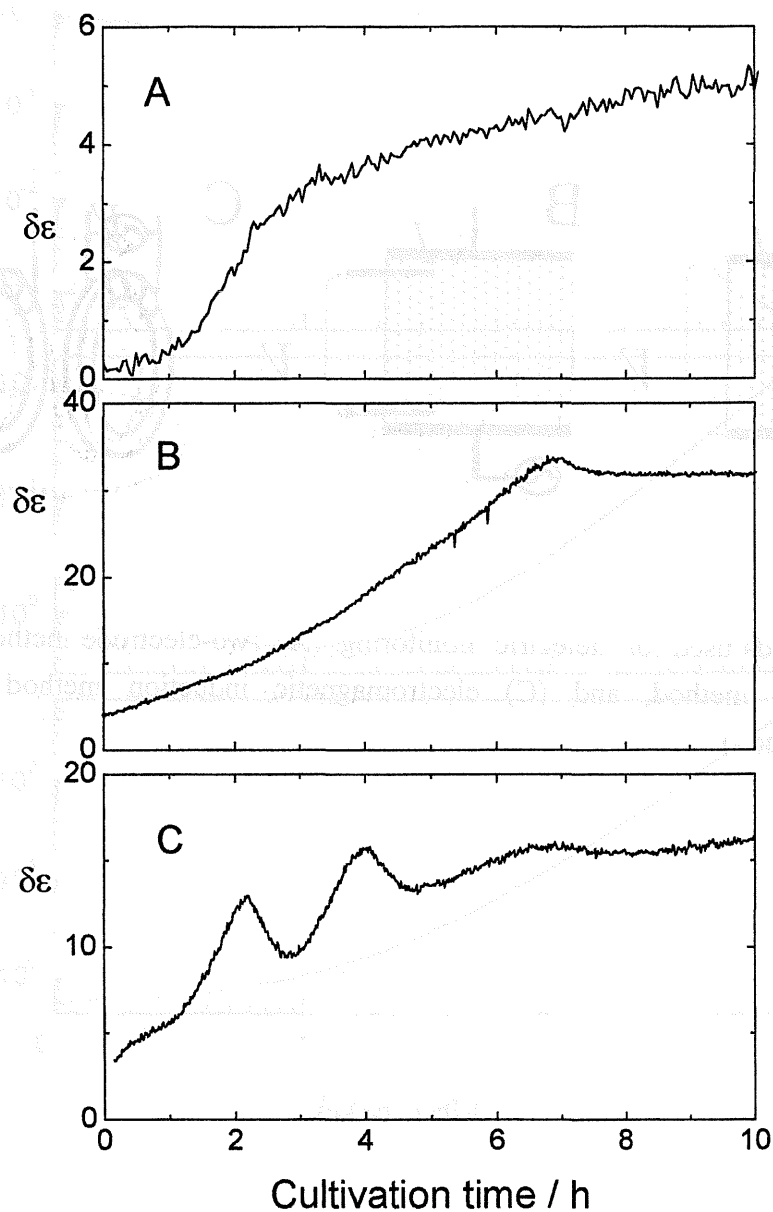


**Fig.7** Dielectric monitoring of bacteria and yeast cells in culture using the electromagnetic induction method. The increment in relative permittivity  $\delta\epsilon$  from the initial culture medium was measured at 0.17 MHz. (A) Non-synchronous growth of *Escherichia coli* (K12), (B) non-synchronous growth of *Saccharomyces cerevisiae* (K6), and (C) synchronous growth of *Saccharomyces*



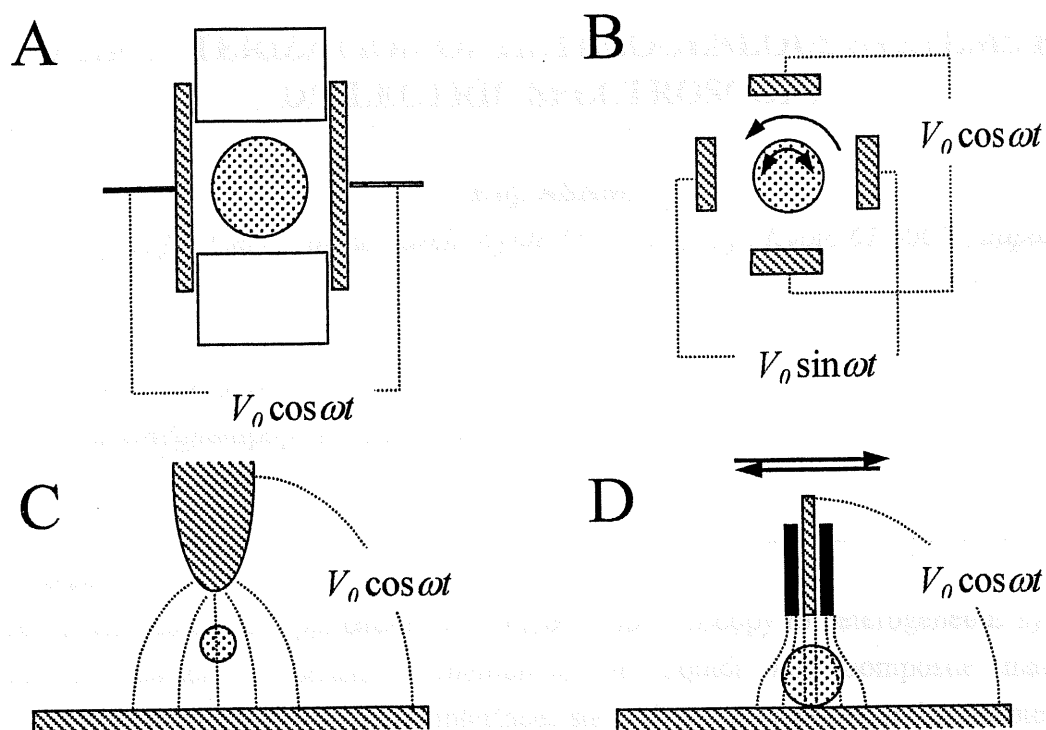


**Fig.8** Methods used for single-cell measurement. (A) Dielectric spectroscopy with a small parallel plate capacitor, (B) electrorotation, (C) dielectrophoresis, and (D) scanning dielectric microscopy.

Progress in Polymer Science (in press)

## CHARACTERIZATION OF HETEROGENEOUS SYSTEMS BY DIELECTRIC SPECTROSCOPY

Koji ASAMI

*Institute for Chemical Research, Kyoto University, Uji, Kyoto 611-0011, Japan*

Fax: +81-774-38-3084

E-mail: [asami@tampopo.kuicr.kyoto-u.ac.jp](mailto:asami@tampopo.kuicr.kyoto-u.ac.jp)

---

### Abstract

This article describes applications of dielectric spectroscopy to heterogeneous systems, such as particle suspensions, membranes in liquids and composite materials. Heterogeneous systems including interfaces show dielectric relaxation due to interfacial polarization. Theories for interfacial polarization in two-, three- and multi-phase systems are summarized and technical developments in dielectric spectroscopy are also described. Practical applications to artificial and biological membrane systems and colloidal suspensions including biological cells are presented.

---

**Keywords:** dielectric spectroscopy; heterogeneous systems; dielectric relaxation; interfacial polarization; membranes; colloidal particles

---

### CONTENTS

1. Introduction
2. Dielectric spectroscopy
  - 2.1 Dielectric relaxation
  - 2.2 Measurement techniques
3. Theoretical basis of interfacial polarization
  - 3.1 Two-phase systems
    - 3.1.1 Electrical potential around an ellipsoid in ac field
    - 3.1.2 Effective dipole moment of an ellipsoid induced by ac field
    - 3.1.3 Complex permittivity of a suspension of ellipsoidal particles
    - 3.1.4 Extension to high volume fraction

- 3.1.5 Distribution of particle parameters
  - 3.2 Three-phase systems
    - 3.2.1 Particles covered with a shell
    - 3.2.2 Particles including droplets
  - 3.3 Multi-phase systems
  - 3.4 Influence of ion diffusion, surface roughness and awkward shape
  - 4. Membrane systems
    - 4.1 Lipid bilayer membranes
    - 4.2 Reverse osmosis membranes
    - 4.3 Ion-exchange membranes (concentration polarization)
    - 4.4 Solid supported membranes
    - 4.5 Biological membranes
  - 5. Suspensions of particles
    - 5.1 Emulsions
    - 5.2 Ion-exchange resin beads
    - 5.3 Polystyrene latices
    - 5.4 Microcapsules
    - 5.5 Liposomes
    - 5.6 Biological cells
  - 6. Single particle analysis
    - 6.1 Electromechanical methods
    - 6.2 Scanning dielectric microscopy
  - 7. Concluding remarks
  - Acknowledgements
  - Appendixes
  - References
- 

## 1. INTRODUCTION

Colloidal dispersions, membranes in liquids, composite materials and biological cells are heterogeneous systems, which have diverse functions and structures by assembling the constituent components in various ways. Characterization of heterogeneous systems requires in situ and non-invasive measurement. Dielectric spectroscopy that measures permittivity and conductivity as a function of frequency in a non-invasive way is well suited for this purpose and can provide insights into the structures and electrical properties of heterogeneous systems at molecular and

macroscopic levels. Materials are polarized in ac fields by various polarization mechanisms and their permittivity, as a measure of the polarization, shows frequency dependence, namely dielectric relaxation or dielectric dispersion. Since heterogeneous systems have interfaces where materials of different electrical properties contact each other, the characteristic polarization is interfacial polarization that is due to the build-up of charge on the interfaces [1-8]. The dielectric relaxation due to interfacial polarization provides information on the heterogeneous structure and the electrical properties of the constituent components using an appropriate theory.

Dielectric theories of interfacial polarization have been developed, their validity being tested with various heterogeneous systems [1-4]. Theoretical studies have still continued to seek more reliable theories with more realistic models. Measurement techniques in dielectric spectroscopy have been drastically changed by the advent of computer-controlled instruments capable of precise and rapid measurements over a wide frequency range in the last two decades, namely, broadband dielectric spectroscopy and time-domain reflectometry. This has allowed more precise analysis and facilitated investigations of time-dependent phenomena. Dielectric spectroscopy also provides a promising method for quality control in factories and for evaluation of industrial products.

In this review, I summarize theories of interfacial polarization in various heterogeneous systems and technical developments in dielectric spectroscopy. I present some practical applications to membrane systems and colloidal dispersions including biological cells.

## 2. DIELECTRIC SPECTROSCOPY

### 2.1 Dielectric relaxation

Dielectric spectroscopy measures complex relative permittivity of materials over a wide frequency range. Complex relative permittivity  $\varepsilon^*$  (hereafter, referred to complex permittivity for convenience) is defined as:

$$\varepsilon^* = \varepsilon' - j\varepsilon'' = \varepsilon + \frac{\kappa}{j\varepsilon_0\omega}, \quad (1)$$

where  $\varepsilon'$  and  $\varepsilon''$  are respectively the real and imaginary parts of  $\varepsilon^*$ ,  $\varepsilon$  relative permittivity ( $\varepsilon = \varepsilon'$ ),  $\kappa$  conductivity,  $\varepsilon_0$  the permittivity of vacuum,  $\omega$  angular frequency ( $\omega = 2\pi f$ ,  $f$  is frequency), and  $j = (-1)^{1/2}$ . The relative permittivity  $\varepsilon$  and conductivity  $\kappa$  of materials, though not always, show dielectric relaxation (or dielectric dispersion) in which  $\varepsilon$  decreases and  $\kappa$  increases with increasing frequency (Fig.1a). Single dielectric relaxation is characterized by a set of parameters (called relaxation parameters):  $\varepsilon_i$  and

$\varepsilon_h$  are the low- and the high-frequency limits of relative permittivity, respectively,  $\Delta\varepsilon (= \varepsilon_l - \varepsilon_h)$  the relaxation intensity (or the relaxation magnitude),  $f_0$  the characteristic frequency,  $\tau$  ( $\tau = (2\pi f_0)^{-1}$ ) the relaxation time, and  $\kappa_l$  the low-frequency limit of conductivity.

Instead of the conductivity  $\kappa$ , the loss factor  $\varepsilon''$  ( $\varepsilon'' = \kappa/\omega\varepsilon_0$ , the imaginary part of  $\varepsilon^*$ ) may also be plotted against frequency, giving rise to a peak at the characteristic frequency  $f_0$  (Fig.1b). If the dc conductivity ( $=\kappa_l$ ) is not negligible, the loss factor is calculated from  $\varepsilon'' = (\kappa - \kappa_l)/\omega\varepsilon_0$ . The complex plane plot (or the Cole-Cole plot) is also used for the analysis of dielectric relaxation (Fig.1c). In the complex plane plot the loss factor  $\varepsilon''$  is plotted against the relative permittivity  $\varepsilon$  (or  $\varepsilon'$ , the real part of  $\varepsilon^*$ ), tracing a semicircle if the dielectric relaxation has a single relaxation time, namely, the Debye type relaxation. The complex plane plots, however, often deviate from a semicircle, which indicates a distribution of relaxation times. The deviation is formulated by various empirical equations proposed by Cole and Cole [9], Davidson and Cole [10], Havriliak and Negami [11], von Schweidler [12], Williams and Watts [13], Fuoss-Kirkwood [14], Jonscher [15] and so forth, some of which are summarized in Table 1 and Fig.2. These equations are often used not only for classifying dielectric relaxation of various materials for convenience but also for extracting the relaxation parameters from dielectric relaxation data. However, the physical (or molecular) meanings of the parameters related to the distribution of relaxation times are certainly open to question. Further, it must be kept in mind that different equations with multi parameters can sometimes fit the same data.

The chief mechanisms of dielectric relaxation in the radio frequency range are reorientation of polar molecules and interfacial polarization. Although the heterogeneous systems include both the mechanisms, our main concern is interfacial polarization that is characteristic of heterogeneous systems. Even if our interest is not in interfacial polarization but in molecular polarization in heterogeneous systems, careful consideration of interfacial polarization is prerequisite for discussion on molecular polarization.

<Figs.1 and 2>

<Table 1>

## 2.2. Measurement techniques

Dielectric spectra can be easily obtained over a frequency range of 1 Hz to 10 GHz using rapid, automated, frequency-domain spectrometers (FDS) with high precision. Recently, time-domain spectrometers (TDS) have been improved in accuracy



[16, 17], the time required for measurements being much shorter than FDS, thereby enabling us to investigate faster phenomena.

For measurements at frequencies below tens MHz, we commonly use measuring cells of parallel-plate capacitor type (Fig.3a). The measuring cells require correction for the residual inductance and capacitance arising from the cell itself and the connecting leads [18]. If a fringing field at the edges of parallel plate electrodes causes a serious error, the three-terminal method is effective for its elimination (Fig.3b). Open-ended coaxial probes are suited for measurements with network analyzers and time domain reflectometers at frequencies above 100 MHz (Fig.3c).

Samples containing electrolytes have a serious problem at frequencies below tens kHz owing to electrode polarization, i.e., the impedance at the boundary between metal electrodes and electrolyte solutions. Although various correction methods have been proposed so far [18], there has been no established method yet. To eliminate the electrode polarization effect, some measurement techniques such as the four-electrode method [19] (Fig.3d) and the electromagnetic induction method with a pair of toroidal coils [20] (Fig.3e) have been developed. Their applications are, however, limited to rather high frequency ranges and/or to special cases.

Recently, single-particle analysis has been developed and becomes increasingly important especially in medical and biotechnological researches. For the single-particle analysis electromechanical techniques [21, 22], such as electrorotation and dielectrophoresis, are used in stead of conventional dielectric spectroscopy. Alternatively, imaging techniques with a scanning fine probe are also available in the single-particle analysis [23].

<Fig.3>

### 3. THEORETICAL BASIS OF INTERFACIAL POLARIZATION

Although this paper is concerned with dielectric properties of macroscopic heterogeneous systems, the calculations that will be described below might also be useful for obtaining fundamental molecular information because those provide the frequency dependent internal electric field acting on a molecule. The calculations on multi-phase systems with differing shapes could particularly serve to analyze dielectric behavior of polar molecules in molecular aggregates, complex ions, and biopolymers with bond water. However, the limitation of the macroscopic approach to molecular behavior is not well understood and is still controversial.

If special interface phenomena in heterogeneous systems are disregarded at first approximation, their dielectric properties can be approached from the "composite

material" standpoint. Indeed, the composite material approach has proved to be quite effective for many heterogeneous systems. Hence, we focus mainly on the composite material approach, namely Maxwell-Wagner polarization, although theories related to the ion diffusion around charged interfaces are briefly described. In the following sections, first we derive general formulas for the complex permittivity of binary systems based on ellipsoidal models. Although the derivation is cumbersome, the general formulas merit yielding various equations for spherical, cylindrical and planar systems as special cases. Secondly, three-phase and multi-phase systems are dealt with.

### 3.1. Two-phase Systems

#### 3.1.1 Electrical potential around an ellipsoid in ac field

Let's consider an ellipsoid whose surface is expressed as:

$$\frac{x^2}{R_x^2} + \frac{y^2}{R_y^2} + \frac{z^2}{R_z^2} = 1, \quad (2)$$

where  $R_x$ ,  $R_y$  and  $R_z$  are the semiaxes along the  $x$ -,  $y$ - and  $z$ -axes, respectively (Fig.4a). When a homogeneous ac field  $E(E_x, E_y, E_z)$  is applied to the ellipsoid of complex permittivity  $\epsilon_p^*$  in a continuous medium of  $\epsilon_a^*$ , the electrical potentials ( $V_{out}$  and  $V_{in}$ ) outside and inside the ellipsoid are obtained by solving the Laplace equation with the boundary conditions at the surface of the ellipsoid.

$$V_{out} = - \sum_{k=x,y,z} E_k k \left\{ 1 - \frac{\epsilon_p^* - \epsilon_a^*}{\epsilon_a^* + (\epsilon_p^* - \epsilon_a^*) L_k} L_k' \right\}, \quad (3)$$

$$V_{in} = - \sum_{k=x,y,z} E_k k \frac{\epsilon_a^*}{\epsilon_a^* + (\epsilon_p^* - \epsilon_a^*) L_k}, \quad (4)$$

where

$$L_k' = \frac{R_x R_y R_z}{2} \int_s^\infty \frac{ds}{(R_k^2 + s) R_s}, \quad (5)$$

$$L_k = \frac{R_x R_y R_z}{2} \int_0^\infty \frac{ds}{(R_k^2 + s) R_s}, \quad (6)$$

$$R_s = \sqrt{(R_x^2 + s)(R_y^2 + s)(R_z^2 + s)}, \quad (7)$$

$$\sum_{k=x,y,z} L_k = 1. \quad (8)$$

At a far apart point from the ellipsoid by  $r$ ,  $L_k'$  is approximated as:

$$L'_k \approx \frac{R_x R_y R_z}{3} \frac{1}{r^3}. \quad (9)$$

$L_k$  is called the depolarization factor along the  $k$ -axis, being expressed in terms of the elliptic integrals of the first and the second kind as shown in Appendix A.

<Fig.4>

### 3.1.2. Effective dipole moment of an ellipsoid induced by ac field

Equation 3 indicates that the electrical potential outside the ellipsoid includes the contributions of the external electric field  $E$  and the dipole moment of the ellipsoid induced by the  $E$ . To evaluate the induced dipole moment, we first consider the dipole moment induced by the  $x$ -component of the  $E$ . Equation 3 is rewritten using Eq.9 as:

$$V_{out,x} = -E_x r \cos \theta \left\{ 1 - \frac{\epsilon_p^* - \epsilon_a^*}{\epsilon_a^* + (\epsilon_p^* - \epsilon_a^*) L_x} \frac{R_x R_y R_z}{3} \frac{1}{r^3} \right\}, \quad (10)$$

where  $\theta$  is the angle between the  $x$ -axis and the  $r$ -direction. The second term of Eq.10 is the contribution of the induced dipole moment of the ellipsoid. Alternatively, the potential due to the equivalent dipole moment  $\mu_x$  along the  $x$ -axis is

$$V_{out,x} = \frac{\mu_x}{4\pi r^2 \epsilon_a^* \epsilon_0} \cos \theta. \quad (11)$$

Equating the second term of Eq.10 to Eq.11 we obtain  $\mu_x$  as:

$$\mu_x = 4\pi \epsilon_a^* \epsilon_0 \frac{\epsilon_p^* - \epsilon_a^*}{\epsilon_a^* + (\epsilon_p^* - \epsilon_a^*) L_x} \frac{R_x R_y R_z}{3} E_x. \quad (12)$$

The total dipole moment  $\mu$  is given by the sum of the  $x$ -,  $y$ - and  $z$ -components.

$$\mu = \mu_x \mathbf{i}_x + \mu_y \mathbf{i}_y + \mu_z \mathbf{i}_z, \quad (13)$$

where  $\mathbf{i}_x$ ,  $\mathbf{i}_y$ ,  $\mathbf{i}_z$  are the unit vectors along the  $x$ -,  $y$ - and  $z$ -axes, respectively. With the angle  $\varphi_k$  between the direction of the ac field and the  $k$ -axis (see Fig.4b) the component of the dipole moment in the  $E$ -direction is given by

$$\begin{aligned} m &= \mu_x \cos \varphi_x + \mu_y \cos \varphi_y + \mu_z \cos \varphi_z \\ &= \frac{4\pi R_x R_y R_z}{3} \epsilon_a^* \epsilon_0 E \sum_{k=x,y,z} \frac{\epsilon_p^* - \epsilon_a^*}{\epsilon_a^* + (\epsilon_p^* - \epsilon_a^*) L_k} \cos^2 \varphi_k, \end{aligned} \quad (14)$$

with

$$\cos^2 \varphi_x + \cos^2 \varphi_y + \cos^2 \varphi_z = 1. \quad (15)$$

### 3.1.3. Complex permittivity of a suspension of ellipsoidal particles

When a system has  $N$  particles per unit volume, each of which have a dipole moment  $m$  in the  $E$ -direction, the polarization  $P$  of the system is given by  $P=mN$  and the electric flux density  $D$  is

$$D = \varepsilon_a^* \varepsilon_0 E + P = \varepsilon_a^* \varepsilon_0 E + mN. \quad (16)$$

Hence, the complex permittivity of the dilute suspension of oriented ellipsoids is obtained substituting Eq. 14 for  $m$  in Eq. 16 [24].

$$\varepsilon^* = D/\varepsilon_0 E = \varepsilon_a^* \left[ 1 + \Phi \sum_{k=x,y,z} \frac{\varepsilon_p^* - \varepsilon_a^*}{\varepsilon_a^* + (\varepsilon_p^* - \varepsilon_a^*) L_k} \cos^2 \varphi_k \right]. \quad (17)$$

where  $\Phi = 4\pi R_x R_y R_z N/3$  and  $\Phi$  is the volume fraction of particles in the suspension.

Rearrangement of Eq. 17 yields the following equation that includes three relaxation terms of the Debye type.

$$\varepsilon^* = \varepsilon_h + \sum_{k=x,y,z} \frac{\Delta \varepsilon_k}{1 + j\omega \tau_k} + \frac{\kappa_l}{j\omega \varepsilon_0}. \quad (18)$$

The relaxation parameters ( $\varepsilon_h$ ,  $\Delta \varepsilon_k$ ,  $\tau_k$  and  $\kappa_l$ ) are related to the phase parameters ( $\varepsilon_p$ ,  $\kappa_p$ ,  $\varepsilon_a$ ,  $\kappa_a$  and  $\Phi$ ) and the depolarization factor  $L_k$  as shown in Appendix B.

When the ellipsoids orient such that the  $k$ -axis is parallel to the electric field, Eq. 17 is simplified as:

$$\varepsilon^* = \varepsilon_a^* \left[ 1 + \Phi \frac{\varepsilon_p^* - \varepsilon_a^*}{\varepsilon_a^* + (\varepsilon_p^* - \varepsilon_a^*) L_k} \right], \quad (19)$$

which has only one relaxation term of the Debye type. When the ellipsoids orient at random in suspension,  $\langle \cos^2 \varphi_k \rangle = 1/3$  and thus Eq. 17 becomes

$$\varepsilon^* = \varepsilon_a^* \left[ 1 + \frac{1}{3} \Phi \sum_{k=x,y,z} \frac{\varepsilon_p^* - \varepsilon_a^*}{\varepsilon_a^* + (\varepsilon_p^* - \varepsilon_a^*) L_k} \right]. \quad (20)$$

This equation has been derived by many authors [24-27], having three relaxation terms of the Debye type. For ellipsoids of revolution (spheroids) of  $R_x = R_y \neq R_z$ , two of the three relaxation terms become the same and therefore two relaxation terms are expected.

Figure 5a shows theoretical calculations of dielectric relaxation for suspensions of spheroids that are oriented at random. The reduced intensity  $\Delta \varepsilon/\Phi$  and the relaxation time  $\tau$  of the two relaxation terms due to the effective dipole moments along the rotational axis (the  $z$ -axis) and the other axes (the  $x$ - and  $y$ -axes) were calculated from

Eq.20. The axial ratio of the spheroids  $q$  ( $q=R_z/R_x=R_z/R_y$ ) seriously affects the intensity and relaxation time of the two relaxation terms.  $\Delta\epsilon_z$  and  $\tau_z$  are strongly dependent on the axial ratio  $q$  for prolate spheroids ( $q>1$ ) but not for oblate spheroids ( $q<1$ ), whereas reverse relations are found for  $\Delta\epsilon_x+\Delta\epsilon_y$  and  $\tau_x$  ( $\tau_x=\tau_y$ ). Figure 5b shows the effects of orientation of spheroids on dielectric relaxation. With prolate-spheroids of  $q=10$ , the intensity of the two relaxation terms changes depending on the angle  $\phi_z$  between the major axis (the  $z$ -axis) and the direction of the electric field  $E$ . When the major axis of the spheroids orients by 54.7 degrees from the  $E$ -direction, the dielectric relaxation is the same as that for randomly oriented spheroids.

In stead of Eq.19, Sillars [28] derived an alternative equation in a similar manner to Maxwell-Wagner's derivation for spherical particle suspensions [29, 30].

$$\frac{\epsilon^* - \epsilon_a^*}{\epsilon_a^* + (\epsilon^* - \epsilon_a^*)L_k} = \Phi \frac{\epsilon_p^* - \epsilon_a^*}{\epsilon_a^* + (\epsilon_p^* - \epsilon_a^*)L_k} \quad (21)$$

Similarly, an alternative equation for Eq.20 was also obtained for a suspension of randomly oriented ellipsoids [31].

$$\frac{\epsilon^* - \epsilon_a^*}{\epsilon^* + 2\epsilon_a^*} = \frac{1}{9} \Phi \sum_{k=x,y,z} \frac{\epsilon_p^* - \epsilon_a^*}{\epsilon_a^* + (\epsilon_p^* - \epsilon_a^*)L_k} \quad (22)$$

On the assumption of  $\Phi \ll 1$ , Eqs.21 and 22 become Eqs.19 and 20, respectively.

In the case of spherical particles,  $L_k$  is 1/3 (see Appendix A) and either Eqs.21 or 22 reduces to Wagner's equation [30]

$$\frac{\epsilon^* - \epsilon_a^*}{\epsilon^* + 2\epsilon_a^*} = \Phi \frac{\epsilon_p^* - \epsilon_a^*}{\epsilon^* + 2\epsilon_p^*} \quad (23)$$

For cylinders whose longitudinal direction is perpendicular to the direction of the electric field, the approximate value of  $L_k$  is 1/2 (see Appendix A) and the corresponding equation is obtained substituting 1/2 for  $L_k$  in Eq.21 as:

$$\frac{\epsilon^* - \epsilon_a^*}{\epsilon^* + \epsilon_a^*} = \Phi \frac{\epsilon_p^* - \epsilon_a^*}{\epsilon^* + \epsilon_p^*}, \quad (24)$$

and, for a two-planar layer system, the substitution of  $L_k=1$  in Eq.21 leads

$$\frac{1}{\epsilon^*} = (1 - \Phi) \frac{1}{\epsilon_a^*} + \Phi \frac{1}{\epsilon_p^*} \quad (25)$$

<Fig.5>



### 3.1.4. Extension to high volume fraction

In the previous section we have described the complex permittivity of dilute particle suspensions in which there is no interaction between particles. For concentrated particle suspensions, we need to deal with the interaction between induced dipoles of particles. It is, however, difficult to solve the problem rigorously. Bruggeman proposed the effective medium theory that provided a reasonable approximation to the problem. In the theory, each particle is assumed to be dispersed in the effective medium including particles rather than the real medium. Bruggeman derived an equation for the conductivity of spherical particle suspensions [32]. The Bruggeman equation was extended to the case of complex permittivity by Hanai [33]. Boned and Peyrelasse [34] further extended Hanai's equation to ellipsoidal particle suspensions.

In the Bruggeman's theory the initially low volume fraction is gradually increased by infinitesimal additions of particles. When a small amount of particles of  $\varepsilon_p^*$  are added to the particle suspension that is regarded as an effective medium of  $\varepsilon^*$ , Eq.20 derived for dilute suspensions of randomly oriented ellipsoid particles may be applicable to every addition process. Hence, the increment in complex permittivity  $d\varepsilon^*$  due to an infinitesimal addition of particles is related to the increment in volume fraction  $d\Phi$  by substituting  $\varepsilon^* + d\varepsilon^*$ ,  $\varepsilon^*$  and  $d\Phi/(1-\Phi)$  for  $\varepsilon$ ,  $\varepsilon_a^*$ ,  $\Phi$  in Eq.20, respectively.

$$-\frac{d\Phi'}{1-\Phi'} = \frac{3}{\varepsilon^*(\varepsilon^* - \varepsilon_p^*)} \left[ \sum_{k=x,y,z} \frac{1}{\varepsilon^* + (\varepsilon_p^* - \varepsilon^*)L_k} \right]^{-1} d\varepsilon^* \quad (26)$$

By successive infinitesimal additions of particles, the system reaches the final volume fraction  $\Phi$  and complex permittivity  $\varepsilon^*$ , and thus we obtain an integral equation as:

$$\int_0^\Phi -\frac{d\Phi'}{1-\Phi'} = \int_{\varepsilon_a^*}^{\varepsilon^*} \frac{3}{\varepsilon^*(\varepsilon^* - \varepsilon_p^*)} \left[ \sum_{k=x,y,z} \frac{1}{\varepsilon^* + (\varepsilon_p^* - \varepsilon^*)L_k} \right]^{-1} d\varepsilon^* \quad (27)$$

Solving this integral equation, we obtain the final form as:

$$1 - \Phi = \left( \frac{\varepsilon_a^* - \alpha\varepsilon_p^*}{\varepsilon^* - \alpha\varepsilon_p^*} \right)^A \left( \frac{\varepsilon_a^* - \beta\varepsilon_p^*}{\varepsilon^* - \beta\varepsilon_p^*} \right)^B \left( \frac{\varepsilon^* - \varepsilon_p^*}{\varepsilon_a^* - \varepsilon_p^*} \right) \left( \frac{\varepsilon_a^*}{\varepsilon^*} \right)^{3T}, \quad (28)$$

where

$$A = -\frac{(1-2S-3T)\alpha + 2(S-3T)}{2\sqrt{1-3S}}, \quad (29)$$

$$B = \frac{(1-2S-3T)\beta + 2(S-3T)}{2\sqrt{1-3S}}, \quad (30)$$

$$\alpha = \frac{S - 1 - \sqrt{1 - 3S}}{1 + S}, \quad (31)$$

$$\beta = \frac{S - 1 + \sqrt{1 - 3S}}{1 + S}, \quad (32)$$

$$S = L_x L_y + L_y L_z + L_z L_x, \quad (33)$$

$$T = \frac{L_x L_y L_z}{S}. \quad (34)$$

For spheroids of  $R_x = R_y \neq R_z$ , Eq.27 with  $L=L_x=L_y$  and  $L_z=1-2L$  becomes

$$1 - \Phi = \left( \frac{\epsilon_a^*(1+3L) + \epsilon_p^*(2-3L)}{\epsilon_a^*(1+3L) + \epsilon_p^*(2-3L)} \right)^C \left( \frac{\epsilon_a^* - \epsilon_p^*}{\epsilon_a^* - \epsilon_p^*} \right) \left( \frac{\epsilon_a^*}{\epsilon^*} \right)^{3T}, \quad (35)$$

with

$$T = \frac{L_x L_y L_z}{L_x L_y + L_y L_z + L_z L_x} = \frac{L(1-2L)}{(2-3L)}, \quad (36)$$

$$C = \frac{2(1-3L)^2}{(2-3L)(1+3L)}. \quad (37)$$

When ellipsoids are oriented such that the  $k$ -axis is parallel to the electric field, Eq.35 reduces to the equation derived by Boyle [35].

$$1 - \Phi = \left( \frac{\epsilon_a^* - \epsilon_p^*}{\epsilon_a^* - \epsilon_p^*} \right) \left( \frac{\epsilon_a^*}{\epsilon^*} \right)^{L_k}. \quad (38)$$

For spherical particles, Eq.38 with  $L_k=1/3$  becomes Hanai's mixture equation [33].

$$1 - \Phi = \left( \frac{\epsilon_a^* - \epsilon_p^*}{\epsilon_a^* - \epsilon_p^*} \right) \left( \frac{\epsilon_a^*}{\epsilon^*} \right)^{1/3}. \quad (39)$$

Hanai's mixture equation has proved to give excellent simulations for various colloidal dispersions over a wide range of volume fraction up to 0.8. Equation 38 with  $L_k=1/2$  provides the complex permittivity for cylinders whose longitudinal direction is perpendicular to the direction of the electric field.

$$1 - \Phi = \left( \frac{\epsilon_a^* - \epsilon_p^*}{\epsilon_a^* - \epsilon_p^*} \right) \left( \frac{\epsilon_a^*}{\epsilon^*} \right)^{1/2}. \quad (40)$$

and for two-planar layer system Eq.38 with  $L_k=1$  becomes Eq.25.

Figure 6 shows the effects of volume fraction on dielectric relaxation for spherical particle suspensions. The calculation was made using Eq.39 with the parameter values relevant to water in oil (W/O) type emulsions. The dielectric relaxation curves become broader with increasing volume fraction, i.e., the complex plane plots deviate from a semicircle (the Debye type) at volume fractions above 0.5. Hanai et al. [36] reported that the deviation was simulated by circular arcs (the Cole-Cole type) at volume fractions between 0.5 and 0.6 and by deformed arcs proposed by Williams and Watts [13] at volume fractions above 0.7.

<Fig.6>

### 3.1.5. Distribution of particle parameters

The morphological and electrical parameters of particles are to some extent different from particle to particle even if particles are carefully prepared. The distribution of the parameters causes broadening of the relaxation spectrum due to a distribution of relaxation times. In this case, Eqs.20 and 22 can be extended to a suspension including  $n$  kinds of particles as:

$$\epsilon^* = \epsilon_a^* \left[ 1 + \frac{1}{3} \Phi \sum_{g=1}^n r_g \sum_{k=x,y,z} \frac{\epsilon_{pg}^* - \epsilon_a^*}{\epsilon_a^* + (\epsilon_{pg}^* - \epsilon_a^*) L_{kg}} \right], \quad (41)$$

$$\frac{\epsilon^* - \epsilon_a^*}{\epsilon^* + 2\epsilon_a^*} = \frac{1}{9} \Phi \sum_{g=1}^n r_g \sum_{k=x,y,z} \frac{\epsilon_{pg}^* - \epsilon_a^*}{\epsilon_a^* + (\epsilon_{pg}^* - \epsilon_a^*) L_{kg}}, \quad (42)$$

where  $\epsilon_{pg}^*$  and  $L_{kg}$  is the complex permittivity and the depolarization factor of the  $g$ th group particles and  $r_g$  is the relative volume fraction of the  $g$ th group ( $\sum_{g=1}^n r_g = 1$ ).

According to the Bruggeman-Hanai procedure, Eq.41 can be simply extended to concentrated suspensions as:

$$\int_0^\Phi -\frac{d\Phi'}{1-\Phi'} = \int_{\epsilon_a^*}^{\epsilon^*} \frac{3}{\epsilon^*} \left[ \sum_{g=1}^n r_g \sum_{k=x,y,z} \frac{\epsilon^* - \epsilon_{pg}^*}{\epsilon^* + (\epsilon_{pg}^* - \epsilon^*) L_{kg}} \right]^{-1} d\epsilon^* \quad (43)$$

In the case of two kinds of particles ( $n=2$ ), Hanai and Sekine solved Eq.43 to obtain an analytical equation [37].

## 3.2. Three-phase systems

### 3.2.1. Particles covered with a shell

When a particle has a layer between its surface and the external medium, such as colloidal particles with an electrical double layer and biological cells with the plasma membrane, we may adopt a shell ellipsoid model having two confocal surfaces (Fig. 7a) that are expressed as:

$$\frac{x^2}{R_x^2} + \frac{y^2}{R_y^2} + \frac{z^2}{R_z^2} = 1, \quad (44)$$

$$\frac{x^2}{R_{ix}^2} + \frac{y^2}{R_{iy}^2} + \frac{z^2}{R_{iz}^2} = 1, \quad (45)$$

$$R_{ik}^2 = R_k^2 - s, \quad (46)$$

where  $R_k$  and  $R_{ik}$  are the semiaxes of the outer and inner surfaces along the  $k$ -axis respectively,  $s$  is the parameter representing a family of the confocal surfaces. When the shell-ellipsoid has the inner phase of complex permittivity of  $\epsilon_i^*$  and the shell phase of  $\epsilon_2^*$ , the electrical potential outside the shell-ellipsoid are obtained by solving the Laplace equation under the boundary conditions at the two surfaces [31, 38, 39].

$$V_{out} = - \sum_{k=x,y,z} E_k k \left\{ 1 - \frac{\epsilon_{pk}^* - \epsilon_a^*}{\epsilon_a^* + (\epsilon_{pk}^* - \epsilon_a^*) L_k} L_k' \right\}, \quad (47)$$

where

$$\epsilon_{pk}^* = \epsilon_2^* \left[ 1 + \frac{v(\epsilon_1^* - \epsilon_2^*)}{\epsilon_2^* + (\epsilon_1^* - \epsilon_2^*)(L_{ik} - vL_k)} \right], \quad (48)$$

with

$$L_{ik} = \frac{R_{ix}R_{iy}R_{iz}}{2} \int_0^\infty \frac{ds}{(R_{ik}^2 + s)R_{is}}, \quad (49)$$

$$R_{is} = \sqrt{(R_{ix}^2 + s)(R_{iy}^2 + s)(R_{iz}^2 + s)}, \quad (50)$$

$$v = \frac{R_{ix}R_{iy}R_{iz}}{R_xR_yR_z}. \quad (51)$$

Equation 48 provides the effective complex permittivity  $\epsilon_{pk}^*$  of the shell-ellipsoid along the  $k$ -axis. Comparing Eq. 47 with Eq. 3 we notice that the complex permittivity of the suspension of shell-ellipsoids can be obtained by substituting  $\epsilon_{pk}^*$  for  $\epsilon_p^*$  in one of the equations (Eqs. 17 and 19-22) for the two-phase systems described in section 3.1.3. The

combination of Eq.20 and Eq.48 provides six relaxation terms of the Debye type for randomly oriented shell-ellipsoids [40]. For shell-spheres, we obtain the effective complex permittivity as

$$\varepsilon_p^* = \varepsilon_2^* \frac{2(1-\nu)\varepsilon_2^* + (1+2\nu)\varepsilon_1^*}{(2+\nu)\varepsilon_2^* + (1-\nu)\varepsilon_1^*}, \quad (52)$$

and their suspension has two relaxation terms of the Debye type [41]. For shell-cylinders whose longitudinal direction is oriented perpendicular to the  $E$ -direction, the equivalent complex permittivity is

$$\varepsilon_p^* = \varepsilon_2^* \frac{(1-\nu)\varepsilon_2^* + (1+\nu)\varepsilon_1^*}{(1+\nu)\varepsilon_2^* + (1-\nu)\varepsilon_1^*}, \quad (53)$$

and the complex permittivity of the whole system is given by combining Eqs.24 and 53. For a planar layer having two phases, the equivalent complex permittivity is

$$\frac{1}{\varepsilon_p^*} = (1-\nu) \frac{1}{\varepsilon_2^*} + \nu \frac{1}{\varepsilon_1^*}. \quad (54)$$

The combination of Eqs.25 and 54 provides the complex permittivity of three-layer systems.

$$\frac{1}{\varepsilon^*} = (1-\Phi) \frac{1}{\varepsilon_a^*} + \Phi \left[ (1-\nu) \frac{1}{\varepsilon_1^*} + \nu \frac{1}{\varepsilon_2^*} \right]. \quad (55)$$

The equations for dilute suspensions of shell-ellipsoids can be simply extended to high volume fraction according to the Bruggeman-Hanai procedure although we have to consider the anisotropy of the equivalent complex permittivity of the shell-ellipsoid  $\varepsilon_{pk}^*$ .

$$\int_0^\Phi -\frac{d\Phi'}{1-\Phi'} = \int_{\varepsilon_a^*}^{\varepsilon^*} \frac{3}{\varepsilon^*} \left[ \sum_{k=x,y,z} \frac{\varepsilon^* - \varepsilon_{pk}^*}{\varepsilon^* + (\varepsilon_{pk}^* - \varepsilon^*)L_k} \right]^{-1} d\varepsilon^*. \quad (56)$$

Boned and Peyrelasse [34] solved Eq.56 in the case of randomly oriented shell-spheroids to obtain an analytical equation for the concentrated suspension. For suspensions of shell-spheres, Hanai et al. [42] derived an equation by substituting Eq.52 for  $\varepsilon_p^*$  in Eq.39, as an extension of Pauly-Schwan's equation [41].

### 3.2.2 Particles including droplets

Next we consider another three-phase system that is a suspension of ellipsoidal particles including spherical droplets (Fig.7b). The equivalent complex permittivity  $\varepsilon_p^*$  of the ellipsoidal particle in which spherical droplets of  $\varepsilon_1^*$  are in a continuous phase of  $\varepsilon_2^*$  at volume fraction  $\nu$  may be calculated from Eq.52 for  $\nu < 0.1$  and for higher values of  $\nu$ ,



$$1 - v = \left( \frac{\varepsilon_p^* - \varepsilon_1^*}{\varepsilon_2^* - \varepsilon_1^*} \right) \left( \frac{\varepsilon_2^*}{\varepsilon_p^*} \right)^{1/3}. \quad (57)$$

The complex permittivity  $\varepsilon^*$  of the suspension of randomly oriented particles including droplets is given by combining Eq.57 and Eq.22 or 28.

Equation 57 may be also applicable to particle aggregates in which the inter-particle space is assumed to have the same complex permittivity as the bulk external phase, i.e.,  $\varepsilon_2^* = \varepsilon_a^*$  [43].

<Fig.7>

### 3.3. Multi-phase Systems

The equations for the two- and three-phase systems described in the previous sections can be simply extended to more complicated multi-phase systems [44]. Here, we deal with the multi-shell ellipsoid model that is a core ellipsoid covered with confocal shells (Fig.8). The multi-shell model is applicable to biological cells having intracellular organelles and multi-lamella lipid vesicles. The complex permittivity of the multi-shell ellipsoid is formulated by successive applications of Eq.48 that represents the effective complex permittivity of the single-shell ellipsoid. For convenience, we define the following function.

$$f(\varepsilon_s^*, \varepsilon_i^*, L_{out,k}, L_{in,k}, v) = \varepsilon_s^* \left[ 1 + \frac{v(\varepsilon_i^* - \varepsilon_s^*)}{\varepsilon_s^* + (\varepsilon_i^* - \varepsilon_s^*)L_{in,k} - v(\varepsilon_i^* - \varepsilon_s^*)L_{out,k}} \right], \quad (58)$$

where  $\varepsilon_s^*$  and  $\varepsilon_i^*$  are respectively the complex permittivities of the shell and inner phases,  $L_{out,k}$  and  $L_{in,k}$  are the depolarization factors for the outer and inner surfaces of the shell, and  $v$  is the volume ratio of the inner ellipsoid to the outer one.

We suppose an ellipsoid includes  $n$  confocal shells, which are numbered in the increasing order from the inner most to the outer most shell. The effective complex permittivity  $\bar{\varepsilon}_{p1k}^*$  of the inner most shell-ellipsoid (referred to the 1st shell-ellipsoid) that a core ellipsoid of  $\varepsilon_c^*$  is covered with the 1st shell of  $\varepsilon_{s1}^*$  is given by

$$\bar{\varepsilon}_{p1k}^* = f(\varepsilon_{s1}^*, \varepsilon_c^*, L_{1k}, L_{0k}, v_1), \quad (59)$$

where  $v_1 = R_{0x}R_{0y}R_{0z} / R_{1x}R_{1y}R_{1z}$ ,  $R_{0k}$  and  $R_{1k}$  are the semiaxes of the inner and the outer surfaces of the 1st shell respectively, and  $L_{0k}$  and  $L_{1k}$  are the depolarization factors for the inner and outer surfaces of the 1st shell. Next, the 1st shell-sphere is regarded as a

homogeneous inner phase (referred to the 2nd inner phase) of  $\bar{\epsilon}_{p1k}^*$ . The equivalent complex permittivity  $\bar{\epsilon}_{p2k}^*$  of the 2nd shell-ellipsoid including the 2nd inner phase and the 2nd shell of  $\epsilon_{s2}^*$  is represented as:

$$\bar{\epsilon}_{p2k}^* = f(\epsilon_{s2}^*, \bar{\epsilon}_{p1k}^*, L_{2k}, L_{1k}, v_2), \quad (60)$$

where  $v_2 = R_{1x}R_{1y}R_{1z} / R_{2x}R_{2y}R_{2z}$ ,  $R_{2k}$  and  $L_{2k}$  are the semiaxe and the depolarization factor of the outer surface of the 2nd shell.

Similarly, for the  $g$ th shell-ellipsoid that consists of the  $g$ th shell of  $\epsilon_{sg}^*$  and the  $g$ th inner phase of  $\bar{\epsilon}_{p(g-1)k}^*$  the effective complex permittivity is given by

$$\bar{\epsilon}_{pgk}^* = f(\epsilon_{sg}^*, \bar{\epsilon}_{p(g-1)k}^*, L_{gk}, L_{(g-1)k}, v_g). \quad (61)$$

Finally, we obtain the equivalent complex permittivity of the ellipsoid with  $n$ th shells as:

$$\epsilon_{pk}^* = f(\epsilon_{sn}^*, \bar{\epsilon}_{p(n-1)k}^*, L_{nk}, L_{(n-1)k}, v_n). \quad (62)$$

For spherical particles, the following function can be used instead of Eq.58 [45-47].

$$f(\epsilon_s^*, \epsilon_i^*, v) = \epsilon_s^* \frac{2(1-v)\epsilon_s^* + (1+2v)\epsilon_i^*}{(2+v)\epsilon_s^* + (1-v)\epsilon_i^*} \quad (63)$$

Figure 9 shows theoretical dielectric relaxation calculated using the single-shell and the multi-shell models, which are relevant to biological cells and multi lamella vesicles. In the calculation, the multi-shell model has membranes and aqueous inter-membrane phase that are alternately arranged. The complex permittivity was calculated for spherical particle suspensions by varying the number  $n_m$  of membranes. The characteristics of dielectric behavior obtained from the calculations are as follows. The low-frequency limit of the relative permittivity is not affected by the inner membranes but depends on the outer most membrane. The number of dielectric relaxation terms increase with increasing  $n_m$  and the complex plain plots are close to a skewed arc for  $n_m > 100$ .

<Figs.8 and 9>

### 3.4. Influence of ion diffusion, surface roughness and awkward shape

Recently, theories related to interfacial polarization have been developed to analyze interfacial phenomena. When particles with charged surfaces disperse in

aqueous electrolyte solutions, the effect of ion-diffusion in the electrical double layer becomes considerable and the electrical double layer forms a surface conductive layer. The theories predicted two relaxation processes: the polarization due to the ion-diffusion and the Maxwell-Wagner polarization due to the conductive surface layer [48-50]. The theories interpreted the dielectric relaxation observed for polystyrene particle dispersions.

Effects of surface roughness of particles on the dielectric relaxation are not clearly understood. For biological cells, the roughness of the membrane surface has been analyzed on the basis of a fractal model [51, 52].

The ellipsoidal model is useful for understanding the effects of particle shape on dielectric relaxation of non-spherical particle suspensions. However, the model is not sufficient to represent diverse and awkward shape. Numerical calculations of the complex permittivity of such particles in suspension have been developed using the boundary integral equation method [53], the finite element method [54] and the boundary element method [55].

#### 4. MEMBRANE SYSTEMS

When a planar membrane of complex permittivity  $\epsilon_m^*$  separates two liquid phases having the same complex permittivity  $\epsilon_a^*$ , the whole system is represented by Eq.25, i.e.,

$$\frac{1}{\epsilon^*} = (1 - \Phi) \frac{1}{\epsilon_a^*} + \Phi \frac{1}{\epsilon_m^*} \quad (64)$$

With the cross section  $S$  and length  $l$  of the whole system and the membrane thickness  $d$ ,  $\Phi$  is given by  $\Phi = d/l$  and thus Eq.64 is rewritten as:

$$\frac{1}{C^*} = \frac{1}{C_a^*} + \frac{1}{C_m^*}, \quad (65)$$

where  $C^*$ ,  $C_a^*$  and  $C_m^*$  are the complex capacitances defined by  $C^* = \epsilon_0 \epsilon^* (S/l)$ ,  $C_a^* = \epsilon_0 \epsilon_a^* [S/(l-d)]$  and  $C_m^* = \epsilon_0 \epsilon_m^* (S/d)$ , respectively. In general, complex capacitance can be expressed by

$$C^* = C + \frac{G}{j\omega}, \quad (66)$$

where  $C$  and  $G$  are the capacitance and conductance, respectively. Thus, the membrane/aqueous phase system may be represented by the equivalent circuit model shown in Fig.10. Similarly, three-layer systems, such as a homogeneous membrane in asymmetric bathing solutions and a membrane having two different layers in symmetric bathing solutions, are expressed by a combination of three  $C/G$  circuit units in series as:

$$\frac{1}{C^*} = \frac{1}{C_a^*} + \frac{1}{C_m^*} + \frac{1}{C_b^*}, \quad (67)$$

where  $C_b^*$  is the complex capacitance of the third layer. The equivalent circuit approach may be extended to multi-membrane systems with  $n$  lamellas, i.e., a combination of  $n$   $C/G$  circuit units in series [56].

<Fig.10>

#### 4.1. Lipid Bilayer Membranes

The basic structure of biological cell membranes is a lipid bilayer containing functional proteins. Hence, artificial bilayer lipid membranes (BLMs) are important as a model of biological cell membranes and are used for reconstitution of membrane proteins to study their functions. Planar BLMs formed on a small hole of a Teflon sheet that separates two aqueous electrolyte solutions are convenient for electrical measurements; the trans-membrane admittance is directly measured with a pair of electrodes placed in the bathing solutions. If the BLM is regarded as a homogeneous layer, the membrane/aqueous phase system would be a two-phase system. Since the conductance of the membrane is much lower than that of the bathing solutions, the membrane/aqueous phase system is approximately represented by a serial combination of the capacitance corresponding to the membrane and the resistance to the aqueous phase. Hanai et al. [57] found dielectric relaxation of the Debye type for lecithin membranes as expected from the electrical model and determined the membrane capacitance, which gave the first good estimate for the thickness of the hydrophobic layer of the membrane. Following their studies, the membrane capacitance of planar BLMs has been intensively studied, e.g., the effects of the diffuse double layers at the surface of the membrane and the effect of various alkanes on the membrane thickness [58].

Bilayer lipid membrane, however, are not a simple thin oil membrane but have hydrophilic surface layers outside the hydrophobic layer. The electrical properties of the hydrophilic surface layers are different from those of the hydrophobic layer and the external electrolyte solutions. The membrane with the two layers is expected to have one dielectric relaxation term, thus the membrane/aqueous phase system may have two relaxation terms. Indeed, Coster and Smith [59] found that planar BLMs showed another small relaxation at low frequencies below 10 Hz, and first estimated the electrical properties of the hydrophilic surface layers (Fig.11). Later, they resolved further four relaxation terms corresponding to four layers within the hydrophilic region by their improved measuring technique [60].

&lt;Fig.11&gt;

#### 4.2. Reverse Osmosis Membranes

Reverse osmosis is the basis of sea and brackish water desalination. The desalination uses asymmetric membranes made up of an ultrathin, dense skin layer with a porous support layer underneath. The skin layer is the active layer for reverse osmosis under a high trans-membrane pressure difference. The evaluation of the structure and the electrical properties of the skin layer is important for understanding the mechanism of reverse osmosis and also for improving the efficiency of desalination. Asaka [61] studied dielectric relaxation of asymmetric cellulose acetate membranes in various aqueous electrolyte solutions. He found dielectric relaxation, from which the membrane capacitance  $C_m$  and conductance  $G_m$  were determined. The thickness of the membrane estimated from the observed  $C_m$  was about 30 nm, being different from the nominal thickness of the membrane but the same order of the thickness of the skin layer determined by electron microscopy. The result suggested that the  $C_m$  is attributed to the skin layer and that the support layer does not contribute to the dielectric relaxation. The conductivity of the skin layer that was estimated from the membrane conductance  $G_m$  was the order of 1  $\mu\text{S}/\text{m}$  in 10 mM NaCl. The  $G_m$  depended not only on the conductance of the aqueous solution  $G_w$  but also the type of electrolyte. The sequence of the  $G_m/G_w$  ratio for different types of electrolytes was the same as the solute separation sequence determined by Matsuura et al. [62].

#### 4.3 Ion-exchange Membranes (concentration polarization)

Concentration polarization (CP) has been extensively studied in connection with membrane separation processes such as electrodialysis, filtration and reverse osmosis. In electrodialysis, where ion-exchange membranes are subjected to dc voltages, concentration polarization occurs at the interfaces between the membranes and the bathing solutions; the concentration of ions changes towards the membrane surface as a consequence of ion permeation. This phenomenon is unfavorable in the practical applications because it reduces ions available for current transport and thus water dissociation occurs.

Zhao et al. [63, 64] studied the CP phenomena of anion- and cation-exchange membranes in water by dielectric spectroscopy. In the absence of dc voltage the membrane/aqueous electrolyte systems did not show any dielectric relaxation because the ion-exchange membranes with high density fixed charges have a high conductivity value. In contrast, in the presence of dc voltage, two-step dielectric relaxation including



two relaxation terms has been developed (Fig.12b). The two-step relaxation suggests the presence of at least three phases of different electrical properties in the system. In general, CP layers occur at the both sides of the membrane, namely, ion-depletion and ion-accumulation layers. Theoretical assessments, however, indicate that the ion-accumulation layer does not contribute to dielectric relaxation as well as the membrane itself. Hence, the system is regarded as the three-phase system that consists of the ion-depletion CP layer (of complex capacitance,  $C_{cp}^*$ ), and the two aqueous bulk phases ( $C_a^*$  and  $C_b^*$ ) (Fig.12a). In the CP layer of thickness  $d_{cp}$ , it is assumed that the conductivity linearly changes from  $\kappa_\beta$  to  $\kappa_\alpha$  keeping the relative permittivity  $\epsilon_{cp}$  constant. The complex capacitance  $C_{cp}^*$  of the CP layer is given by [65]

$$C_{cp}^* = \frac{S(\kappa_\beta - \kappa_\alpha)}{d_{cp}} \frac{1}{A^2 + B^2} \left( \frac{B}{\omega} + \frac{A}{j\omega} \right), \quad (68)$$

where

$$A = \frac{1}{2} \ln \left[ 1 + \frac{(\kappa_\beta / \kappa_\alpha)^2 - 1}{1 + (\epsilon_{cp} \epsilon_0 / \kappa_\alpha)^2 \omega^2} \right], \quad (69)$$

$$B = \tan^{-1} \frac{(\kappa_\beta - \kappa_\alpha) \omega \epsilon_{cp} \epsilon_0}{(\omega \epsilon_{cp} \epsilon_0)^2 + \kappa_\beta \kappa_\alpha}. \quad (70)$$

The complex capacitance  $C^*$  of the whole system is represented by a combination of  $C_{cp}^*$ ,  $C_a^*$  and  $C_b^*$  in series. The model excellently interpreted the observed relaxation curves (Fig.12b and c), and allowed to estimate the thickness  $d_{cp}$  and the conductivity gradient  $(\kappa_\beta - \kappa_\alpha)/d_{cp}$  of the CP layer from the dielectric relaxation.

<Fig.12>

#### 4.4. Solid Supported Membranes

In contrast to free-standing planar BLMs, solid supported bilayer lipid membranes have many potential applications because of the long term stability and the possibility to use electrically conductive supports [66-68]. The advantages enable us to fabricate molecular biosensors. Self assembly of thiolipids onto gold surfaces forms ultra thin and high-resistance layers, which are suitable for the sensor systems. Dielectric (impedance) spectroscopy has been used for determining either the surface coverage of gold surfaces with lipid membranes or the membrane thickness, and also for detecting ligand binding to supported receptor/lipid membranes [68-70]

Figure 13 shows the formation of a thiolipid bilayer on a gold surface monitored

by dielectric spectroscopy. The lipid bilayer was formed by applying a thiolipid (octadecyl mercaptan) vesicle suspension to a gold electrode. Dielectric relaxation found at 0 min, which is almost due to the interfacial impedance between the bare gold electrode and the bathing solution, drastically changed with increasing the coverage of the gold electrode surface with a lipid bilayer (Fig.13a and b). The final relaxation spectrum was the Debye type and was represented by the model used for planar BLMs. The membrane conductance was about  $10^{-2}$  S/m<sup>2</sup> and the capacitance was about 6 mF/m<sup>2</sup>. This suggested that a lipid bilayer was formed by the fusion of the thiolipid vesicles on the gold surface (Fig.13c). The final surface coverage of the gold surface with the lipid bilayer was estimated to be 99.8 %.

<Fig.13>

#### 4.5 Biological membranes

Dielectric (admittance) properties of biological membranes have been measured with several electrode configurations [71]. If biological cells are large enough like squid giant axons, the trans-membrane admittance can be measured between an internal electrode inserted into the cytoplasm and an external electrode (Fig.14a). For small spherical cells, we can use the patch pipette method that measures the trans-membrane admittance at the whole cell clamp configuration (Fig.14b).

The membrane capacitance that was measured for some non-excitable cells using the patch pipette was almost unchanged between 1 Hz and 1 kHz [72, 73]. On the contrary, frequency dependence of the membrane capacitance was found for muscle cells and their cultured cells, being due to the presence of the extensive enfolding of surface membrane, namely T-tubules [74-76]. Nerve membranes also showed frequency-dependent membrane capacitance, which was explained in terms of the ionic flow related to membrane excitability [77,78].

<Fig.14>

### 5. SUSPENSIONS OF PARTICLES

#### 5.1. Emulsions

Emulsions have been extensively studied by dielectric spectroscopy and provide good test systems to examine the validity of dielectric mixture equations [2, 4]. In the case of water-in-oil (W/O) emulsions, where water droplets disperse in oil, we may assume that the conductivity of the oil phase is much lower than that of the water droplets. For spherical droplets, the following approximate equations are obtained from Hanai's equation (Eq.39) for the concentrated suspensions.

$$\Phi = 1 - (\varepsilon_a / \varepsilon_l)^{1/3}, \quad (71)$$

$$\kappa_a = \kappa_l (1 - \Phi)^3, \quad (72)$$

$$\varepsilon_p = \varepsilon_a + \frac{\varepsilon_h - \varepsilon_a}{1 - (\varepsilon_h / \varepsilon_l)^{1/3}}, \quad (73)$$

$$\kappa_p = \kappa_h \frac{3 - (2 + \varepsilon_a / \varepsilon_h)(\varepsilon_h / \varepsilon_l)^{1/3}}{3[1 - (\varepsilon_h / \varepsilon_l)^{1/3}]^2}. \quad (74)$$

Using these equations we can determine the volume fraction  $\Phi$  of the water droplets, the conductivity  $\kappa_a$  of the oil phase, and the relative permittivity  $\varepsilon_p$  and conductivity  $\kappa_p$  of the water droplets from the dielectric relaxation parameters ( $\varepsilon_l$ ,  $\varepsilon_h$ ,  $\kappa_l$  and  $\kappa_h$ ) since the relative permittivity  $\varepsilon_a$  is measured for the oil phase separately.

Figure 15 shows typical dielectric relaxation of a W/O emulsion [79]. The W/O emulsion used was prepared by mixing distilled water with the oil (a mixture of kerosene and carbon tetrachloride (73:28 V/V)) containing 0.4% (V/V) Span 80 as an emulsifier. The volume fraction of water droplets ( $\Phi=0.75$ ) estimated from Eq.71 was consistent with the volume ratio of water in the emulsion in preparation. The values of  $\kappa_p$  and  $\varepsilon_p$  were in good agreement with the conductivity and the relative permittivity of the water phase separated from the oil phase by centrifugation after the measurement. The complex plane plots of the dielectric relaxation traced a deformed circular arc, which was excellently simulated by Hanai's mixture equation.

<Fig.15>

For oil-in-water (O/W) emulsions, in which oil droplets disperse in water, the conductivity of the oil droplets is negligibly small compared with that of the aqueous phase. Assuming that  $\kappa_p \ll \kappa_a$  we obtain the following equations from Eq.39.

$$\varepsilon_l = \frac{3}{2} \varepsilon_p + \left( \varepsilon_a - \frac{3}{2} \varepsilon_p \right) (1 - \Phi)^{3/2}, \quad (75)$$

$$\left( \frac{\varepsilon_h - \varepsilon_p}{\varepsilon_a - \varepsilon_p} \right) \left( \frac{\varepsilon_a}{\varepsilon_h} \right)^{1/3} = 1 - \Phi, \quad (76)$$

$$\kappa_l = \kappa_a (1 - \Phi)^{3/2}, \quad (77)$$

$$\kappa_h = \kappa_a \frac{\varepsilon_h (\varepsilon_h - \varepsilon_p) (2\varepsilon_a + \varepsilon_p)}{\varepsilon_a (\varepsilon_a - \varepsilon_p) (2\varepsilon_h + \varepsilon_p)}. \quad (78)$$

These equations enable us to assess the magnitude of dielectric relaxation of O/W emulsions. When the relative permittivity of water phase is 78, that of oil phase is 2.5 and the volume fraction is 0.7, the relaxation intensity becomes 0.15, which is too small to detect. In general most of O/W emulsions do not give a detectable relaxation intensity as expected from the numerical assessment [80,81]. However, the use of an oil with a higher relative permittivity value leads to a definite dielectric relaxation (e.g., nitrobenzene ( $\epsilon=35$ )/water emulsion) [82].

Emulsions are not necessarily stable and change their state on the way to a complete phase separation through some processes, such as sedimentation, flocculation, and coalescence. Since the processes affect the dielectric properties, the state of emulsions can be monitored by dielectric spectroscopy [83]. Skodvin and Sjöblom [43] proposed models for flocculated W/O emulsions as mentioned in section 3.2.2.

### 5.2. Ion-exchange Resin Beads

Column chromatography is widely used for separation of ions and organic molecules. Ion-exchange resin is one of the important packing materials. The electrical properties of ion-exchange resin beads can be evaluated by dielectric spectroscopy. Ishikawa et al. [84, 85] extensively studied dielectric relaxation of various ion-exchange resin beads in distilled water. They developed a method based on Hanai's mixture equation for estimating the phase parameters ( $\kappa_a$ ,  $\Phi$ ,  $\epsilon_p$ ,  $\kappa_p$ ) from the dielectric relaxation parameters ( $\epsilon_i$ ,  $\epsilon_h$ ,  $\kappa_i$ ) and the relative permittivity of the medium  $\epsilon_a$ . The internal conductivity of the ion-exchange resin bead was much higher than the external conductivity. This is because the interior of the ion-exchange bead has movable counterions around the fixed charges. The estimated internal conductivity provided important information on the mobility of counter ions and the interactions between the counter ions and the ionic residues in the ion-exchange resin.

Figure 16 shows frequency dependence of the relative permittivity and conductivity of a bed of cation-exchange resin beads in distilled water. The dielectric relaxation was found around 30 MHz and was well simulated by Hanai's equation with reasonable phase parameters. If we consider the diffusion of the counterions around the fixed charges within the beads, another dielectric relaxation could be expected at lower frequencies. The dielectric relaxation, however, has not been found yet because of the interference of electrode polarization.

<Fig.16>

### 5.3. Polystyrene latices

Polystyrene latices with charged surfaces dispersed in aqueous electrolyte solutions provide a good test system for investigating the effect of the ion diffusion in the diffuse double layer on their dielectric behavior. Schwan et al. [86] found that polystyrene particle suspensions showed dielectric relaxation around several kHz. Recently, several authors reported two relaxation processes: the low-frequency relaxation below 1 MHz and the high-frequency relaxation above 1 MHz [87-90]. The low-frequency relaxation was first interpreted by the redistribution of counterions along the particle surface [48] and later by the theory including the ion diffusion in the diffuse double layer [90]. The high-frequency relaxation may be analyzed by the composite approach based on the model that is an insulating sphere with a conducting surface layer [90].

#### 5.4. Microcapsules

Microcapsules are widely used in pharmaceutical, food and industrial fields. There are many kinds of microcapsules made from various materials. Here, we deal with polystyrene microcapsules (PS-MCs) because of their simple and well-defined structure. PS-MCs have an aqueous spherical core and a thin insulating shell. Thus, the single-shell model is applicable to PS-MCs.

The dense suspension of PS-MCs showed dielectric relaxation including two relaxation terms (Fig.17) [91, 92]. The low-frequency relaxation is mainly attributed to the polarization at the outer interface because it was not affected by the change of the inner phase solution but by that of the outer phase one [93]. The high-frequency relaxation, on the other hand, is due to the polarization at the inner interface.

The dielectric relaxation curves were excellently simulated by the combination of Eqs39 and 52 (Fig.17b). The same analysis was also applied to polymethylmethacrylate microcapsules [94, 95].

<Fig.17>

#### 5.5. Liposomes

Liposomes are vesicles with bilayer lipid membranes, which are spontaneously formed by mixing phospholipids or their analogs in an aqueous solution. Various types of liposomes have been reported: small uni-lamella vesicle (SUV), multi-lamella vesicle (MLV), large uni-lamella vesicle (LUV) and so on. In general, dielectric relaxation of liposomes has three relaxation processes besides water relaxation ( $>1$  GHz): counterion displacement along liposome surfaces (1 kHz - 1 MHz), interfacial polarization (1-100 MHz) [96], and reorientation of dipolar head groups (30-500 MHz) [97]. In the case of



SUV dielectric relaxation due to interfacial polarization is comparable in both intensity and relaxation time with that due to reorientation of dipolar head groups, but the two relaxation processes are distinguishable from each other owing to the difference in temperature dependence [98]. For large liposomes ( $>1 \mu\text{m}$ ), interfacial polarization becomes the dominant relaxation process [99]. Although uni-lamella vesicles are represented by the single-shell model, which predicts two-step dielectric relaxation, LUVs do not show two-step relaxation. This is because one of the two relaxation terms becomes too small to detect under the conditions that the membrane thickness is much smaller than the vesicle radius and the conductivity of the internal phase is similar to that of the external medium.

Figure 18 shows dielectric relaxation of LUV and MLV suspensions. The LUV (or cell-size uni-lamella liposome) suspension was prepared by the method of Kim and Martin [100]. The dielectric relaxation was analyzed based on the single-shell model to provide the membrane capacitance of  $5.0 \text{ mF/m}^2$ , which value is comparable to that estimated for planar BLMS. The MLV suspension prepared by the method of Bangham [101] showed much broader relaxation curves than the LUV suspension. The broad relaxation curves are qualitatively interpreted by the multi-shell model, as shown in Fig.9.

<Fig. 18>

### 5.6 Biological Cells

Biological cells that have the cytoplasm and the plasma membrane are represented by the single-shell model. The thickness  $d$  of the plasma membrane is 5-10 nm, and the radius  $R$  of ordinary cells is around  $10 \mu\text{m}$ . Hence, biological cells hold for the conditions that  $d/R \ll 1$ . The conductivity  $\kappa_m$  of the plasma membrane of viable cells is negligibly small compared with that of the external medium and the cytoplasm. With these assumptions, the following approximate equations are obtained from Eqs.39 and 52.

$$\Phi = 1 - (\kappa_i / \kappa_a)^{2/3}, \quad (79)$$

$$C_m = \frac{2\epsilon_0}{3R} \frac{\epsilon_i \kappa_a - \kappa_i \epsilon_a}{\kappa_a - \kappa_i}, \quad (80)$$

$$\epsilon_i = \epsilon_a + \frac{\epsilon_h - \epsilon_a}{1 - (1 - \Phi)(\epsilon_h / \epsilon_a)^{1/3}}, \quad (81)$$

$$\kappa_i = \frac{(\epsilon_a - \epsilon_i)(2\epsilon_h + \epsilon_i)(\kappa_h / \epsilon_h) - (\epsilon_h - \epsilon_i)(2\epsilon_a + \epsilon_i)(\kappa_a / \epsilon_a)}{3(\epsilon_a - \epsilon_h)}. \quad (82)$$

The volume fraction  $\Phi$  is determined from Eq.79 with the values of  $\kappa_i$  and  $\kappa_a$  observed for the suspension and for the medium, respectively. With the mean radius  $R$  of the cells estimated by microscopy, the membrane capacitance  $C_m$  (defined as  $C_m = \epsilon_m \epsilon_0 / d$ ,  $\epsilon_m$  is the relative permittivity of the membrane) is calculated from Eq.80. The relative permittivity  $\epsilon_i$  and conductivity  $\kappa_i$  of the cytoplasm are estimated from Eqs.81 and 82, respectively. The single-shell model may meet mammalian erythrocytes that have no intracellular organelles. Indeed, spherical erythrocytes that were swollen in moderate hypotonic media showed one dielectric relaxation that was fully simulated by the single-shell model [102] (Fig.19a and c). With the value of 6.6 mF/m<sup>2</sup> estimated for the membrane capacitance of the erythrocytes, the thickness of the hydrophobic region in the plasma membrane is calculated to be 2.5-3.7 nm assuming that its relative permittivity is 2-3.

The cytoplasm of most biological cell types, however, has organelles or membranous structure, which are also polarized owing to interfacial polarization. The polarization may cause additional dielectric relaxations besides the main dielectric dispersion due to the plasma membrane. The dielectric spectra of such cells including intracellular structure are no longer dealt with the single-shell model and have been analyzed using various composite cell models (Fig.20). The "double-shell" model was first applied to lymphoma cells that possess a sizable nucleus [103], and then lymphocytes [51, 102, 104] and budding yeast cells having a vacuole in the cytoplasm [105, 106]. Plant protoplasts isolated from leaves that have a large vacuole and a thin cytoplasmic layer containing chloroplasts were modeled by the double-shell model including vesicles. The model gave a better simulation than the double-shell model [107]. In Figure 19 dielectric relaxation is compared between swollen erythrocytes and lymphocytes, indicating clearly the effect of the nucleolus on the dielectric relaxation.

As non-spherical cells, erythrocyte of biconcave shape, budding yeast as doublet, and fission yeast of rod-like shape have been studied by dielectric spectroscopy [108-110]. All these cells whose shape is represented as a body of rotation showed dielectric relaxation composed of two relaxation terms as expected from the theory based on the shell-spheroid model (Fig.20). Figure 21 shows dielectric relaxation spectra of three populations of fission yeast cells with different cell lengths. Two relaxation terms were clearly distinguished in the three relaxation spectra. The low-frequency relaxation strongly depended on the cell length, whereas the high-frequency relaxation was not sensitive to the cell length. The cell length dependence was qualitatively interpreted by the shell-spheroid model [110].

<Figs.19-21>

## 6. SINGLE PARTICLE ANALYSIS

“Single-particle” approaches would be more straightforward than the ‘suspension’ method that estimates the average electrical properties of particles from the dielectric relaxation of their suspension using an appropriate mixture equation. This is because there is no need to take into account electrical interactions between particles in the single-particle analysis. Hence, Wagner’s mixture equation would be exactly applicable to single spherical particles. Indeed, Pauly-Schwan’s equation based on Wagner’s mixture equation excellently simulated dielectric relaxation of single spherical bilayer membranes [111] and that of single microcapsules [112].

The conventional techniques with small measuring cells of parallel plate capacitor type can be used for rather large single particles ( $>100\mu\text{m}$ ) (Fig.22a). The techniques, however, are difficult to apply to single particles of smaller size ( $<10\mu\text{m}$ ). Such small particles can be analyzed by electromechanical methods [21, 22], such as dielectrophoresis [113-115] (Fig.22b) and electrorotation [116,117] (Fig.22c), which utilize motional responses of particles to applied ac fields. An alternative approach is the use of the scanning dielectric microscope that can image local relative permittivity and conductivity sensed using a scanning fine probe [23] (Fig.22d).

<Fig.22>

### 6.1. Electromechanical methods

When subjected to an ac field, a particle is polarized and has an induced dipole moment. The induced dipole interacts with the field and thus the particle experiences forces and torques. Hence, the motional response of a single particle, measured as a function of frequency of ac field, provides the complex permittivity of the particle using an appropriate theory.

The dielectrophoresis uses heterogeneous ac fields produced using asymmetric electrodes (Fig.22b). A particle experiences force in the heterogeneous ac field and migrates along the gradient of the electric field strength. The time averaged dielectrophoretic force  $\langle F \rangle$  is proportional to the real part of the dipole moment  $\mu$  of the particle [21, 22] as:

$$\langle F \rangle = \frac{1}{2} \text{Re}[\bar{\mu} \cdot \nabla \bar{E}^2]. \quad (83)$$

For a spherical particle, Eq.83 is rewritten as:

$$\langle F \rangle = 2\pi\epsilon_a\epsilon_0 R^3 \text{Re}[K] \nabla E_{rms}^2, \quad (84)$$

where  $E_{rms}$  is the root-mean-square amplitude of the ac field and the Clausius-Mossotti factor  $K$  is

$$K = \frac{\epsilon_p^* - \epsilon_a^*}{\epsilon_p^* + 2\epsilon_a^*}. \quad (85)$$

Kaler et al. [114, 115] devised the levitation method to precisely measure the dielectrophoretic force and succeeded to estimate electrical properties of single biological cells.

The electrorotation measures the rotational rate of a particle in a rotating electric field generated with four electrodes arranged as shown in Fig.22c [116, 117]. The particle experiences the time-averaged torque  $\langle T \rangle$  in the rotating field.

$$\langle T \rangle = \frac{1}{2} \text{Re}[\mu \times E]. \quad (86)$$

For a spherical particle, the time-averaged torque is a function of the imaginary part of the induced dipole moment as:

$$\langle T \rangle = -4\pi\epsilon_a\epsilon_0 R^3 \text{Im}[K] E_0^2, \quad (87)$$

where  $E_0$  is the amplitude of the ac field. For the steady-state rotation, the rotational speed  $\Omega$  is related to the torque as:

$$T = 8\pi\eta R^3 \Omega, \quad (88)$$

where  $\eta$  is the viscosity of the medium. The rotational speed is obtained by equating Eq.87 to Eq.88.

$$\Omega = -\frac{\epsilon_a\epsilon_0 \text{Im}[K] E_0^2}{2\eta}. \quad (89)$$

The Clausius-Mossotti factor  $K$  expressed by Eq.85 has one relaxation term as:

$$K = U_h + \frac{\nabla U}{1 + j\omega\tau}, \quad (90)$$

where

$$\tau = \frac{(\epsilon_p + 2\epsilon_a)\epsilon_0}{\kappa_p + 2\kappa_a}, \quad (91)$$

$$U_h = \frac{\epsilon_p - \epsilon_a}{\epsilon_p + 2\epsilon_a}, \quad (92)$$

$$\nabla U = \frac{\kappa_p - \kappa_a}{\kappa_p + 2\kappa_a} - \frac{\epsilon_p - \epsilon_a}{\epsilon_p + 2\epsilon_a}. \quad (93)$$

The real and imaginary parts of  $K$ , which are proportional to the dielectrophoretic force and the rotational speed, respectively, become

$$\operatorname{Re}[K] = U_h + \frac{\Delta U}{1 + (\omega\tau)^2}, \quad (94)$$

$$\operatorname{Im}[K] = -\frac{\Delta U\omega\tau}{1 + (\omega\tau)^2}. \quad (95)$$

$\Delta U$  has either a negative or a positive value depending on the electrical properties of the particle and the medium. Equation 94 indicates that the dielectrophoretic force changes around the frequency of  $1/(2\pi\tau)$ . The spectrum of the rotational speed would have a peak at the frequency of  $1/(2\pi\tau)$  as expected from Eq.95. Figure 23 shows calculations of  $\operatorname{Re}[K]$  and  $\operatorname{Im}[K]$  to simulate the electromechanical responses of an oil droplet in water and a water droplet in oil.

For the shell-sphere model that is applicable to microcapsules and biological cells, the Clausius-Mossotti factor  $K$  is simply obtained by substituting Eq.52 for  $\epsilon_p^*$  in Eq.85. In this case, two relaxation terms are predicted. Similarly, the Clausius-Mossotti factor is simply extended to the multi-shell sphere. Figure 24 shows calculations of  $\operatorname{Re}[K]$  and  $\operatorname{Im}[K]$  using the single-shell model and the multi-shell model of spherical shape. In the multi-shell model, membranes and inter membrane spaces are alternately arranged to simulate biological cells including intracellular organelles and multi-lamella liposomes.

<Figs.23 and 24>

## 6.2. Scanning dielectric microscopy

The scanning dielectric microscopy (SDM) has been developed for imaging the permittivity and conductivity of fine particles in liquids over a wide frequency range [23]. The SDM uses the coaxial probe consisting of an inner probing electrode and an outer guard electrode, which is scanned over a sample on a plate electrode (Fig.22d). The dielectric measurement is based on the three-terminal method that is effective to eliminate the fringing field and to restrict the measurement to a small area. The SDM, therefore, would enable us to examine dielectric properties of individual particles, although its application to date is limited to low-conductive media because of interference of electrode polarization. This method has proved to be useful for the single particle analysis of PS-microcapsules [118] and be successful for imaging cultured cells attached on substrates [119]. Figure 25 shows line-scan images and 2-dimensional dielectric images of a single PS-microcapsule in water over a frequency range of 10 kHz to 10 MHz. Two-step dielectric relaxation was clearly seen from the line-scan images as expected from the single-shell model.



&lt;Fig.25&gt;

## 7. CONCLUDING REMARKS

Dielectric relaxation of membrane systems and colloidal dispersions found in the radio frequency range has been well interpreted by theories of interfacial polarization. The number of dielectric relaxations expected in heterogeneous systems depends not only on the number of different interfaces [93] but also on the shape of the inclusions. In practice, however, all relaxations predicted are not observed because of the limited frequency range and sensitivity in measurement.

Dielectric relaxation spectra of heterogeneous systems are more or less broadened by various factors: electrical and structural interactions between particles, heterogeneity of morphological and electrical parameters of particles, frequency dependence of electrical phase parameters, intra-particle structure, particle shape and so forth. The broadening is liable to cause serious errors in determination of the electrical parameters of particles and membranes from the observed dielectric relaxation, but it may also include important information not only on the electrical and structural properties of particles and membranes and but also on the interactions between particles. Theoretical developments are required for investigating the broadening of dielectric spectra.

So long as measurements are made with suspensions containing many particles, the influence of either interactions between particles or heterogeneity of particles in a particle population are unavoidable. However, if we can measure relaxation spectra for single particles, the analysis becomes straightforward. Electromechanical techniques and dielectric imaging using a scanning probe electrode are promising tool for single-particle analysis.

By taking advantage of modern dielectric spectrometers capable of real-time measurement, dielectric spectroscopy enables us to investigate dynamic behavior of heterogeneous systems and provides a promising tool for either monitoring production processes or evaluation of product quality in industrial applications.

## Acknowledgement

Much of the work described in this paper was performed by our research group directed at first by Prof. T. Hanai and in collaboration with Prof. A. Irimajiri. I thank Prof. T. Hanai, Prof. A. Irimajiri, Dr. K. Sekine and Dr. K. Asaka for carefully reading drafts for this article and helpful comments.

## Appendixes

### A. Depolarization factor

The depolarization factor  $L_k$  along the  $k$ -axis is expressed in terms of the elliptic integrals of the first kind  $F(\varphi, k)$  and the second kind  $E(\varphi, k)$  [39]. When the semiaxes are supposed to be  $R_x > R_y > R_z$ ,  $L_x$  along the  $x$ -axis becomes

$$L_x = \frac{R_x R_y R_z}{(R_x^2 - R_z^2)^{1/2} (R_x^2 - R_y^2)} [F(\varphi, \kappa) - E(\varphi, \kappa)], \quad (\text{A1})$$

where

$$F(\varphi, \kappa) = \int_0^\varphi \frac{d\theta}{\sqrt{1 - \kappa^2 \sin^2 \theta}}, \quad (\text{A2})$$

$$E(\varphi, \kappa) = \int_0^\varphi \sqrt{1 - \kappa^2 \sin^2 \theta} d\theta, \quad (\text{A3})$$

with

$$\kappa = \sqrt{\frac{R_x^2 - R_y^2}{R_x^2 - R_z^2}}, \quad (\text{A4})$$

$$\varphi = \cos^{-1}(R_z/R_x). \quad (\text{A5})$$

The depolarization factor  $L_y$  along the  $y$ -axis is

$$L_y = \frac{R_x R_y R_z}{(R_x^2 - R_z^2)^{3/2}} \left\{ \frac{1}{\kappa^2 \kappa'^2} [E(\varphi, \kappa) - \kappa'^2 F(\varphi, \kappa)] - \frac{\sin 2\varphi}{2\kappa'^2 \sqrt{1 - \kappa^2 \sin^2 \varphi}} \right\}, \quad (\text{A6})$$

where  $\kappa'^2 = 1 - \kappa^2$ . Finally,  $L_z$  is calculated from  $L_z = 1 - L_x - L_y$ .

For an ellipsoid of revolution with  $R_x = R_y \neq R_z$  and  $L_x = L_y \neq L_z$ ,  $L_z$  is simply expressed with the axial ratio  $q = R_z/R_x$  as:

for prolate spheroids ( $q > 1$ ),

$$L_z = -\frac{1}{q^2 - 1} + \frac{q}{(q^2 - 1)^{3/2}} \ln \left[ q + (q^2 - 1)^{1/2} \right], \quad (\text{A7})$$

for oblate spheroids ( $q < 1$ ),

$$L_z = \frac{1}{1 - q^2} - \frac{q}{(1 - q^2)^{3/2}} \cos^{-1} q. \quad (\text{A8})$$

$L_x$  and  $L_y$  are given by  $L_x = L_y = (1 - L_z)/2$ .

For spherical particles ( $q = 1$ ):

$$L_x = L_y = L_z = \frac{1}{3}. \quad (\text{A9})$$

For needles or cylinders ( $q \gg 1$ ):

$$L_z \approx \frac{1}{q^2} \ln(2q-1) \approx 0 \text{ and } L_x = L_y \approx \frac{1}{2}. \quad (\text{A10})$$

For disks or lamellas ( $q \ll 1$ ):

$$L_z \approx 1 - q \cos^{-1} q \approx 1 \text{ and } L_x = L_y \approx 0. \quad (\text{A11})$$

### B. Frequency dependence of the complex permittivity expressed by Eq.17

Equation 17 is rewritten as

$$\varepsilon^* - \varepsilon_a^* = \Phi \varepsilon_a^* \sum_{k=x,y,z} \frac{\varepsilon_p^* - \varepsilon_a^*}{\varepsilon_a^* + (\varepsilon_p^* - \varepsilon_a^*) L_k} \cos^2 \varphi_x. \quad (\text{B1})$$

One of the three terms in the right hand side of Eq.B1 can be rearranged as:

$$\begin{aligned} \varepsilon_a^* \frac{\varepsilon_p^* - \varepsilon_a^*}{\varepsilon_a^* + (\varepsilon_p^* - \varepsilon_a^*) L_k} \Phi \cos^2 \varphi_k &= \varepsilon_a^* \frac{a + j\omega b}{c_k + j\omega d_k} \Phi \cos^2 \varphi_k \\ &= \frac{a\kappa_a + (j\omega)(b\kappa_a + a\varepsilon_a\varepsilon_0) + (j\omega)^2 b\varepsilon_a\varepsilon_0}{c_k(j\omega\varepsilon_0)(1 + j\omega d_k/c_k)} \Phi \cos^2 \varphi_k, \\ &= \varepsilon'_{hk} + \frac{\Delta\varepsilon_k}{1 + j\omega\tau_k} + \frac{\kappa'_{lk}}{j\omega\varepsilon_0} \end{aligned} \quad (\text{B2})$$

where

$$a = \kappa_p - \kappa_a, \quad (\text{B3})$$

$$b = \varepsilon_0(\varepsilon_p - \varepsilon_a), \quad (\text{B4})$$

$$c_k = \kappa_a + (\kappa_p - \kappa_a)L_k, \quad (\text{B5})$$

$$d_k = \varepsilon_0[\varepsilon_a + (\varepsilon_p - \varepsilon_a)L_k], \quad (\text{B6})$$

$$\tau_k = \frac{d_k}{c_k}, \quad (\text{B8})$$

$$\varepsilon'_{hk} = \frac{b}{d_k} \varepsilon_a \Phi \cos^2 \varphi_k, \quad (\text{B9})$$

$$\kappa'_{lk} = \frac{a}{c_k} \Phi \cos^2 \varphi_k, \quad (\text{B10})$$

$$\Delta \varepsilon_k = \left[ \varepsilon_a \left( \frac{a}{c_k} - \frac{b}{d_k} \right) + \frac{\kappa_a}{\varepsilon_0} \left( \frac{b}{c_k} - \frac{ad_k}{c_k^2} \right) \right] \Phi \cos^2 \varphi_k. \quad (\text{B11})$$

Equation B2 has one relaxation term of the Debye type, and therefore Eq.B1 is expressed as:

$$\varepsilon^* = \varepsilon_h + \sum_{k=x,y,z} \frac{\Delta \varepsilon_k}{1 + j\omega\tau_k} + \frac{\kappa_l}{j\omega\varepsilon_0}, \quad (\text{B12})$$

where

$$\varepsilon_h = \varepsilon_a + \sum_{k=x,y,z} \varepsilon'_{lk}, \quad (\text{B13})$$

$$\kappa_l = \kappa_a + \sum_{k=x,y,z} \kappa'_{lk}. \quad (\text{B14})$$

When ellipsoids orient at random in suspension, the complex permittivity of the suspension is obtained substituting  $\cos^2 \varphi_k = 1/3$  in Eqs.B9-B11.

## REFERENCES

1. van Beek LKH. Dielectric behaviour of heterogeneous systems. In: Birks JB editor. Progress in Dielectrics. vol.7. London: Heywood Books, 1967. p.69-114.
2. Hanai T. Electrical properties of emulsions. In: Sherman P editor. Emulsion Science. London and New York: Academic Press, 1968. p. 353-478.
3. Dukhin SS, Shilov VN. Dielectric Phenomena and the Double Layer in Disperse Systems and Polyelectrolites. Jerusalem: Halsted, 1974.
4. Clausse M. Dielectric properties of emulsions and related systems. In: Becher P editor. Encyclopedia of Emulsion Technology. New York and Basel: Marcel Dekker, 1983. p. 481-715.
5. Pethig R. Dielectric and Electronic Properties of Biological Materials. New York: John Wiley & Sons, 1979.
6. Takashima S. Electrical Properties of Biopolymers and Membranes. Bristol and Philadelphia: Adam Hilger, 1989.
7. Grant EH, Sheppard RJ, South GP. Dielectric Behaviour of Biological Molecules in Solution. Oxford: Oxford University Press, 1978.
8. Foster KR, Schwan HP. Dielectric properties of tissues. In: Polk C, Postow E editors. Handbook of Biological Effects of Electromagnetic Fields. Boca Raton: CRC Press, 1996. p. 27-96.

9. Cole KS, Cole RH. Dispersion and absorption in dielectrics. I. Alternating current characteristics. *J Chem Phys* 1941; 9:341-351.
10. Davidson DW, Cole RH. Dielectric relaxation in glycerol, propylene glycol, and n-propanol. *J Chem Phys* 1951;19:1484-1490.
11. Havriliak S, Negami S. A complex plane representation of dielectric and mechanical relaxation processes in some polymers. *Polymer* 1967;8:161-210.
12. von Schweidler ER. Studien über die Anomalien im Verhalten der Dielektrika. *Annalen der Physik (Leipzig)* 1907;24:711-770.
13. Williams G, Watts DC. Non-symmetrical dielectric relaxation behaviour arising from a simple empirical decay function. *Trans Faraday Soc* 1970;66:80-91.
14. Fuoss RM, Kirkwood JG. Electrical properties of solids. VIII. Dipole moments in polyvinyl chloride-diphenyl system. *J Am Chem Soc* 1941;63:385-394.
15. Jonscher AK. A new model of dielectric loss in polymers. *Colloid Polym Sci* 1975;253:231-250.
16. Cole RH, Berberian JG, Mashimo S, Chryssik G, Burns A, Tombari E. Time domain reflection methods for dielectric measurements to 10 GHz. *J Appl Phys* 1989;66:793-802.
17. Feldman YD, Zuev YF, Polygalov EA, Fedotov VD. Time domain dielectric spectroscopy. A new effective tool for physical chemistry investigation. *Colloid Polym Sci* 1992;270:768-780.
18. Schwan HP. Determination of biological impedances. In: Nastuk WL editor. *Physical Techniques in Biological Research*. Vol. VI, Part B. New York: Academic Press, 1963. p.323-407.
19. Schwan HP, Ferris CD. Four-electrode null technique for impedance measurement with high resolution. *Rev Sci Instrum* 1968;39:481-485.
20. Wakamatsu H. A dielectric spectrometer for liquid using the electromagnetic induction method. *Hewlett-Packard J*. 1997;48:37-44.
21. Pohl HA. *Dielectrophoresis*. Cambridge: Cambridge University Press, 1978.
22. Jones TB. *Electromechanics of Particles*. Cambridge: Cambridge University Press, 1995.
23. Asami K. The scanning dielectric microscope. *Meas Sci Technol* 1994;5:589-592.
24. Niesel W. Die Dielektrizitätskonstanten heterogener Mischkörper aus isotropen und anisotropen Substanzen. *Annalen der Physik (Leipzig)* 1952;10:336-348.
25. Polder D, Van Santen JH. The effective permeability of mixtures of solids. *Physica* 1946;12:257-271.
26. Altshuller AP. The shapes of particles from dielectric constant studies of

- suspensions. *J Phys Chem* 1954;58:544-547.
27. Fricke H. The Maxwell-Wagner dispersion in a suspension of ellipsoids. *J Phys Chem* 1953;57:934-937.
  28. Sillars RW. The properties of a dielectric containing semi-conducting particles of various shapes. *J Inst Elec Engrs (London)* 1937;80:378-394.
  29. Maxwell JC. *Treatise on Electricity and Magnetism*. Oxford: Clarendon Press, 1891.
  30. Wagner KW. Erklärung der dielektrischen Nachwirkungsvorgänge auf Grund Maxerllsher Vorstellungen. *Archiv für Electrotechnik (Berlin)* 1914;2:371-387.
  31. Asami K, Hanai T, Koizumi N. Dielectric approach to suspensions of ellipsoidal particles covered with a shell in particular reference to biological cells. *Jpn J Applied Phys* 1980;19:359-365.
  32. Bruggeman DAG. Berechnug vershiedener physikalischen Konstanten von heterogenen Substanzen. *Annalen der Physik (Leipzig)* 1935;24:636-664.
  33. Hanai T. Theory of the dielectric dispersion due to the interfacial polarization and its application to emulsion. *Kolloid Z.* 1960;171:23-31.
  34. Boned C, Peyrelasse J. Etude de la permittivite complex d'ellipsoïdes disperses dans un milieu continu. *Analyses theorique et unmerique. Colloid Polym Sci* 1983;261:600-612.
  35. Boyle MH. The electrical properties of heterogeneous mixtures containing an oriented spheroidal dispersed phase. *Colloid Polym Sci* 1985;263:51-57.
  36. Hanai T, Kita Y, Koizumi N. Dielectric relaxation profiles in a theory of interfacial polarization developed for concentrated disperse systems of spherical particles. *Bull Inst Chem Res, Kyoto Univ* 1980;58:534-547.
  37. Hanai T, Sekine K. Theory of dielectric relaxations due to the interfacial polarization for two-component suspensions of spheres. *Colloid Polym Sci* 1986;264:888-895.
  38. Schwarz G, Saito M, Schwan HP. On the orientation of nonspherical particles in an alternating electrical field. *J Chem Phys* 1965;10:3562-3569.
  39. Saito M, Schwan HP, Schwarz G. Response of nonspherical biological particles to alternating electric fields. *Biophys J* 1966;6:313-327.
  40. Asami K, Yonezawa T. Dielectric behavior of non-spherical cells in culture. *Biochim Biophys Acta* 1995;1245:317-324.
  41. Pauly H, Schwan HP. Über die Impedanz einer Suspension von kugelförmigen Teilchen mit einer Schale. *Z. Naturforsch.* 1959;14b:125-131.
  42. Hanai T, Asami K, Koizumi N. Dielectric theory of concentrated suspension of



- shell-spheres in particular reference to the analysis of biological cell suspensions. Bull Inst Chem Res, Kyoto Univ 1979;57:297-305.
43. Skodvin T, Sjöblom J. Models for the dielectric properties of flocculated w/o-emulsions. J Colloid Interface Sci 1996;182:190-198.
  44. L.D. Stepin, Dielectric permeability of a medium with nonuniform ellipsoidal inclusions. Soviet Physics-Technical Physics 1965;10:768-772.
  45. Fricke H. The complex conductivity of a suspension of stratified particles of spherical or cylindrical form. J Phys Chem 1955;59:168-170.
  46. Irimajiri A, Hanai T, Inouye A. A dielectric theory of "multi-stratified shell" model with its application to a lymphoma cell. J Theor Biol 1979;78:251-269.
  47. Stepin LD. Permittivity of a medium with inhomogeneous spherical inclusions. Soviet Physics-Technical Physics 1965;9:1348-1351.
  48. Schwarz G. A theory of the low-frequency dielectric dispersion of colloidal particles in electrolyte solution. J Phys Chem 1962;66:2636-2642.
  49. Chew WC, Sen PN. Dielectric enhancement due to electrochemical double layer: Thin double layer approximation. J Chem Phys 1982;77:4683-4693.
  50. Grosse C. Permittivity of a suspension of charged spherical particles in electrolyte solution. 2. Influence of the surface conductivity and asymmetry of the electrolyte on the low-and high-frequency relaxations. J Phys Chem 1988;92:3905-3910.
  51. Bordi F, Cametti C, Rosi A, Calcabrini A. Frequency domain electrical conductivity measurements of the passive electrical properties of human lymphocytes. Biochim Biophys Acta 1993;1153:77-88.
  52. Cametti C, de Luca F, Macri MA, Maraviglia B, Zimatore G, Bordi F, Misasi R, Sorice M, Lenti L, Pavan A. To what extent are the passive electrical parameters of lymphocyte membranes deduced from impedance spectroscopy altered by surface roughness and microvillosity? Colloids Surfaces B: Biointerfaces 1995;3:309-316.
  53. Vrinceanu D, Gheorghiu E. Shape effects on the dielectric behavior of arbitrarily shaped particles with particular reference to biological cells. Bioelectrochem Bioenerg 1996;40:167-170.
  54. Sekine K. Finite-element calculations for dielectric relaxation of one-sphere systems in a parallel-electrode measuring cell. Colloid Polym Sci 1999;277:388-393.
  55. Sekine K. Application of boundary element method to calculation of the complex permittivity of suspensions of cells in shape of  $D_{\infty h}$  symmetry. Bioelectrochem 2000;52:1-7.

56. Kita Y. Dielectric relaxation in distributed dielectric layers. *J Appl Phys* 1984;55:3747-3755.
57. Hanai T, Haydon DA, Taylor J. An investigation by electrical methods of lecithin-in-hydrocarbon films in aqueous solutions. *Proc Roy Soc (London), Series A* 1964;281:377-391.
58. White SH. The physical nature of planar bilayer membranes. In: Miller C editor. *Ion Channel Reconstitution*. New York and London: Plenum, 1986. p. 2-35.
59. Coster HGL, Smith JR. The molecular organization of bimolecular lipid membranes. A study of the low frequency Maxwell-Wagner impedance dispersion. *Biochim Biophys Acta* 1974;373:151-164.
60. Coster HGL, Chilcott TC, Coster ACF. Impedance spectroscopy of interfaces, membranes and ultrastructures. *Bioelectrochem Bioenerg* 1996;40:79-98.
61. Asaka K. Dielectric properties of cellulose acetate reverse osmosis membranes in aqueous salt solutions. *J Membrane Sci* 1990;50:71-84.
62. Matsuura T, Pageau L, Sourirajan S. Reverse osmosis separation of inorganic solutes in aqueous solutions using porous cellulose acetate membranes. *J Appl Polym Sci* 1975;19:179-198.
63. Zhao KS, Matsubara Y, Asaka K, Asami K, Hanai T. Dielectric analysis of concentration polarization phenomena at cation-exchange membrane/solution interfaces by frequency variation and d.c. bias application. *J Membrane Sci* 1991;64:163-172.
64. Zhao KS, Asaka K, Asami K, Hanai T. Dielectric analysis of concentration polarization structure at anion-exchange membrane/solution interface under dc bias voltage application. *J Colloid Interface Sci* 1992;153:562-571.
65. Hanai T, Zhao KS, Asaka K, Asami K. Theoretical approach and the practice to the evaluation of structural parameters characterizing concentration polarization alongside ion-exchange membranes by means of dielectric measurement. *Colloid Polym Sci* 1993;271:766-773.
66. Steinem C, Janshoff A, Ulrich WP, Sieber M, Galla HJ. Impedance analysis of supported lipid bilayer membranes: a scrutiny of different preparation techniques. *Biochim Biophys Acta* 1996;1279:169-180.
67. Heyse S, Stora T, Schmid E, Lakey JH, Vogel H. Emerging techniques for investigating molecular interactions at lipid membranes. *Biochim Biophys Acta* 1998;1376:319-338.
68. Sackmann E. Supported membranes: Scientific and practical applications. *Science* 1996;271:43-48.

69. Stelzle M, Weissmüller G, Sackmann E. On the application of supported bilayers as receptive layers for biosensors with electrical detection. *J Phys Chem* 1993;97:2974-2981.
70. Cornell BD, Braach-Maksvytis VLB, King LG, Osman PDJ, Raguse B, Wieczorek L, Pace RJ. A biosensor that uses ion-channel switches. *Nature* 1997;387:580-583.
71. Takashima S, Asami K, Yantorno RF. Determination of electrical admittances of biological cells. *J Electrostatics* 1988;21:225-244.
72. Takashima S, Asami K, Takahashi Y. Frequency domain studies of impedance characteristics of biological cells using micropipet technique. I. Erythrocyte. *Biophys J* 1988;54:995-1000.
73. Asami K, Takahashi Y, Takashima S. Frequency domain analysis of membrane capacitance of cultured cells (HeLa and myeloma) using the micropipette technique. *Biophys J* 1990;58:143-148.
74. Eisenberg RS, Gage PW. Frog skeletal muscle fibers: changes in electrical properties after disruption of transverse tubular system. *Science* 1967;158:1700-1701.
75. Takashima S. Passive electrical properties and voltage dependent membrane capacitance of single skeletal muscle fibers. *Pflügers Archiv* 1985;403:197-204.
76. Asami K, Takashima S. Membrane admittance of cloned muscle cells in culture: use of a micropipet technique. *Biochim Biophys Acta* 1994;1190:129-136.
77. Takashima S. Admittance change of squid axon during action potentials. Change in capacitance component due to sodium currents. *Biophys J* 1979;26:133-142.
78. Fishman HM, Poussart D, Moore LE. Complex admittance of Na conduction in squid axon. *J Membrane Biol* 1979;50:43-63.
79. Hanai T, Imakita T, Koizumi N. Analysis of dielectric relaxation of w/o emulsions in the light of theories of interfacial polarization. *Colloid Polym Sci* 1982;260:1029-1034.
80. Hanai T, Koizumi N, Gotoh R. Dielectric properties of emulsions. I. Dielectric constants of o/w emulsions. *Kolloid Z* 1959;167:41-43.
81. Hanai T, Koizumi N, Sugano T, Gotoh R. Dielectric properties of emulsions. II. Electrical conductivities of O/W emulsions. *Kolloid Z* 1960;171:20-23.
82. Hanai T, Koizumi N, Gotoh R. Dielectric properties of emulsions. IV. Dielectric behaviour of nitrobenzene-in-water emulsions., *Kolloid Z* 1962;184:143-148.
83. Sax BM, Schön G, Paasch S, Schwuger MJ. Dielectric spectroscopy—a method of investigating the stability of water-oil emulsions. *Prog Colloid Polym Sci*

- 1988;77:109-114.
84. Ishikawa A, Hanai T, Koizumi N. Evaluation of relative permittivity and electrical conductivity of ion-exchange beads by analysis of high-frequency dielectric relaxations. *Jpn J Applied Phys* 1981;20:79-86.
  85. Ishikawa A, Hanai T, Koizumi N. Dielectric properties of quaternary ammonium ion-exchange beads dispersed in aqueous phases. *Colloid Polym Sci* 1984;262:477-480.
  86. Schwan HP, Schwarz G, Maczuk J, Pauly H. On the low-frequency dielectric dispersion of colloidal particles in electrolyte solution. *J Phys Chem* 1962;66:2626-2635.
  87. Ballario C, Bonincontro A, Cametti C. Radiowave dielectric dispersions of colloidal particles in KCl and LiCl electrolyte solutions. *J Colloid Interface Sci* 1979;72:304-313.
  88. Sasaki S, Ishikawa A, Hanai T. Dielectric properties of spherical macroion suspensions. I. Study on monodisperse polystyrene latex. *Biophys Chem* 1981;14:45-53.
  89. Blum G, Maier H, Sauer F, Schwan HP. Dielectric relaxation of colloidal particle suspensions at radio frequencies caused by surface conductance. *J Phys Chem* 1995;99:780-789.
  90. Grosse C, Tirado M, Pieper W, Pottel R. Broad frequency range study of the dielectric properties of suspensions of colloidal polystyrene particles in aqueous electrolyte solutions. *J Colloid Interface Sci* 1998;205:26-41.
  91. Zhang HZ, Sekine K, Hanai T, Koizumi N. Dielectric observations of polystyrene microcapsules and the theoretical analysis with reference to interfacial polarization. *Colloid Polym Sci* 1983;261:381-389.
  92. Zhang HZ, Sekine K, Hanai T, Koizumi N. Dielectric approach to polystyrene microcapsule analysis and the application to the capsule permeability to potassium chloride. *Colloid Polym Sci* 1984;262:513-520.
  93. Hanai T, Zhang HZ, Sekine K, Asaka K, Asami K. The number of interfaces and the associated dielectric relaxations in heterogeneous systems. *Ferroelectrics* 1988;86:191-204.
  94. Sekine K. Dielectric study of poly(methyl methacrylate) microcapsules in particular reference to the effect of the frequency dependence of the permittivity of the capsule wall. *Colloid Polym Sci* 1986;264:943-950.
  95. Sekine K. Analysis of dielectric observations of KCl-charged poly(methyl methacrylate) microcapsules using a two-component model consisting of KCl-

- permeable and KCl-impermeable capsules. *Colloid Polym Sci* 1987;265:1054-1060.
96. Schwan HP, Takashima S, Miyamoto VK, Stoeckenius W. Electrical properties of phospholipid vesicles. *Biophys J* 1970;10:1102-1119.
  97. Pottel R, Kaatz U, Muller St. Dielectric relaxation in aqueous solutions of zwitterionic surfactant micelles. *Ber Bunsen-Ges Phys Chem* 1978;82:1086-1093.
  98. Ermolina I, Smith G, Ryabov Y, Puzenko A, Polevaya Y, Nigmatullin R, Feldman Y. Effect of Penetration Enhancers on the Dynamic Behavior of Phosphatidylcholine Headgroups in Liposomes. *J Phys Chem* 2000;104:1373-1381.
  99. Sekine K, Hanai T, Koizumi N. Dielectric behavior of liposomes of large size. *Bull Inst Chem Res, Kyoto Univ* 1983;61:299-313.
  100. Kim S, Martin GM. Preparation of cell-size unilamellar liposomes with high captured volume and defined size distribution. *Biochim. Biophys. Acta* 1981;646:1-9.
  101. Bangham AD, Hill MW, Miller NGA. Preparation and use of liposomes as models of biological membranes. In: Korn ED editor. *Methods in Membrane Biology*. Vol.1. New York and London: Plenum, 1974. p.1-68.
  102. Asami K, Takahashi Y, Takashima S. Dielectric properties of mouse lymphocytes and erythrocytes. *Biochim Biophys Acta* 1989;1010:49-55.
  103. Irimajiri A, Doida Y, Hanai T, Inouye A. Passive electrical properties of cultured murine lymphoblast (L5178Y) with reference to its cytoplasmic membrane, nuclear envelope, and intracellular phase. *J Membr Biol* 1978;38: 209-232.
  104. Polevaya Y, Ermolina I, Schlesinger M, Ginzburg BZ, Feldman Y. Time domain dielectric spectroscopy study of human cells; II. Normal and malignant white blood cells. *Biochim Biophys Acta* 1999;1419:257-271.
  105. Asami K, Yonezawa T. Dielectric behavior of wild-type yeast and vacuole-deficient mutant over a frequency range of 10 kHz to 10 GHz. *Biophys J* 1996;71:2192-2200.
  106. Raicu V, Raicu G, Turcu G. Dielectric properties of yeast cells as simulated by the two-shell model. *Biochim Biophys Acta* 1996;1274:143-148.
  107. Asami K, Yamaguchi T. Dielectric spectroscopy of plant protoplasts. *Biophys J* 1992;63:1493-1499.
  108. Asami K. Dielectric relaxation spectroscopy of biological cell suspensions. In: Hackley VA, Texter J editors. *Handbook on Ultrasonic and Dielectric Characterization Techniques for Suspended Particulates*. Westerville: The

- American Ceramic Society, 1998. p.333-349.
109. Asami K, Gheorghiu E, Yonezawa T. Dielectric behavior of budding yeast in cell separation. *Biochim Biophys Acta* 1998;1381:234-240.
  110. Asami K. Effect of cell shape on dielectric behavior of fission yeast. *Biochim Biophys Acta* 1999;1472:137-141.
  111. Asami K, Irimajiri A. Dielectric dispersion of a single spherical bilayer membrane in suspension. *Biochim Biophys Acta* 1984;769:370-376.
  112. Asami K, Zhao KS. Dielectric measurement of a single sub-millimeter size microcapsule. *Colloid Polym Sci* 1994;272:64-71.
  113. Pethig R, Huang Y, Wang X, Burt JPH. Positive and negative dielectrophoretic collection of colloidal particles using interdigitated castellated microelectrodes. *J. Phys D: Appl Phys* 1992;24:881-888.
  114. Kaler KVIS, Jones TB. Dielectrophoretic spectra of single cells determined by feedback-controlled levitation. *Biophys. J.* 1990;57:173-182.
  115. Kaler KVIS, Xie JP, Jones TB, Paul R. Dual-frequency dielectrophoretic levitation of *Canola* protoplasts. *Biophys J* 1992;63:58-69.
  116. Arnold WM, Zimmermann U. Rotating-field-induced rotation and measurement of the membrane capacitance of single mesophyll cells of *Avena sativa*. *Z Naturforsch* 1982;37c: 908-915.
  117. Fuhr G, Gimsa J, Glaser R. Interpretation of electrorotation of protoplasts. I. Theoretical considerations. *Studia Biophys* 1985;108:149-164.
  118. Asami K. Dielectric analysis of polystyrene microcapsules using scanning dielectric microscope. *Colloid Polym Sci* 1998;276:373-378.
  119. Asami K. Dielectric imaging of biological cells. *Colloid Polym Sci* 1995;273:1095-1097.



### Figure captions

**Fig.1** Ideal dielectric relaxation of the Debye type. (a) Frequency dependence of relative permittivity and conductivity, (b) frequency dependence of loss factor and (c) complex plane plots. Relaxation parameters ( $\varepsilon_i$ ,  $\kappa_i$ ,  $\varepsilon_h$ ,  $\kappa_h$  and  $f_0$ ) are indicated in (a) and (b).

**Fig.2** Complex plane plots of four relaxation types: (a) Debye, (b) Cole-Cole, (c) Davidson-Cole and (d) Havriliak-Negami, which are formulated as shown in Table 1.

**Fig.3** Electrode configurations and measurement techniques. (a) two-electrode method, (b) three-terminal method, (c) open-ended coaxial probe, (d) four-electrode method and (e) electromagnetic induction method with a pair of toroidal coils. The dotted line in (e) indicates an induced electric field.  $V$  is applied voltage and  $I$  is current.

**Fig.4** (a) Electrical potential  $V_{out}$  at a point outside an ellipsoid (of complex permittivity  $\varepsilon_p^*$ ) in a continuous medium ( $\varepsilon_a^*$ ) when a homogeneous ac field  $E$  is applied.  $R_x$ ,  $R_y$  and  $R_z$  are the semiaxes of the ellipsoid along the  $x$ -,  $y$ - and  $z$ -axes. (b) Effective dipole moment  $\mu$  ( $\mu_x$ ,  $\mu_y$ ,  $\mu_z$ ) induced by the  $E$  and its component  $m$  in the  $E$ -direction.  $\varphi_k$  is the angle between the  $k$ -axis and the  $E$ -direction.

**Fig.5** Dielectric relaxation of suspensions of spheroids. (a) For randomly oriented spheroids in suspension, the reduced relaxation intensity ( $\Delta\varepsilon_z/\Phi$  and  $(\Delta\varepsilon_x+\Delta\varepsilon_y)/\Phi$ ) and relaxation time ( $\tau_z$  and  $\tau_x=\tau_y$ ) were calculated by varying the axial ratio  $q$ . (b) For oriented prolate spheroids of  $q=10$ ,  $\Delta\varepsilon_z/\Phi$  and  $(\Delta\varepsilon_x+\Delta\varepsilon_y)/\Phi$  were calculated by varying the angle  $\varphi_z$  between the major axis and the electric field. The parameter values used are:  $\varepsilon_a=2$ ,  $\kappa_a=10$   $\mu\text{S/m}$ ,  $\varepsilon_p=80$ , and  $\kappa_p=0.1$  S/m.

**Fig.6** Effects of volume fraction  $\Phi$  on dielectric relaxation of spherical particle suspensions. (a) Frequency dependence of relative permittivity and conductivity, (b) normalized complex plane plots. The theoretical curves were calculated from Eq.39 with  $\varepsilon_a=2$ ,  $\kappa_a=10$   $\mu\text{S/m}$ ,  $\varepsilon_p=80$  and  $\kappa_p=0.01$  S/m.

**Fig.7** Electrical models for three-phase systems. (a) Single-shell model and (b) droplet-inclusion model. For details, see text.

**Fig.8** Multi-shell model. The schematic illustration describes the derivation procedure of the theoretical equation. For details, see text.

**Fig.9** Theoretical dielectric relaxation curves for suspensions of spherical particles covered with membranes whose number  $n_m$  is varied as: 1 (single-membrane), 2 (double-membrane), 5 and 200 (multi-membrane). In the calculations for particles with multi membranes, membranes (relative permittivity  $\varepsilon_m$ , conductivity  $\kappa_m$ , and thickness  $d_m$ ) and inter-membrane spaces ( $\varepsilon_{im}$ ,  $\kappa_{im}$ ,  $d_{im}$ ) are alternately arranged. The parameter values used are: for the membrane phase,  $\varepsilon_m=5$ ,  $\kappa_m=0$  S/m and  $d_m=7$  nm; for the inter-

membrane phase,  $\varepsilon_m=80$ ,  $\kappa_m=0.1$  S/m and  $d_m=10$  nm; for the core phase,  $\varepsilon_c=80$  and  $\kappa_c=0.1$  S/cm; for the external phase,  $\varepsilon_a=80$  and  $\kappa_a=0.1$  S/m. The volume fraction is 0.3 and the outer most radius is 10  $\mu\text{m}$ .

**Fig.10** Electrical models of membrane systems that are expressed by equivalent circuit models. (a) Two-lamella system and (b) three-lamella system. For details, see text.

**Fig.11** Dielectric relaxation of planar BLMs in various aqueous electrolyte solutions. The low-frequency relaxation includes several relaxation terms and the high-frequency relaxation is almost the Debye type. (From Coster et al., 1996 [60]) Reproduced by permission of Elsevier Science Ltd.

**Fig.12** (a) An electrical model of the membrane system including concentration polarization layers. (b) and (c): Dielectric relaxation of an ion-exchange membrane in water when subjected to a trans-membrane voltage of 9V. The open circles are data points and the solid lines are calculated by the electrical model in (a). (From Zhao et al., 1991 [63]) Reproduced by permission of Elsevier Science Ltd.

**Fig.13** Dielectric spectra monitored during formation of thiolipid (octadecyl mercaptan) bilayer on a gold electrode. (a) Frequency dependence of the capacitance, and (b) that of the conductance. (c) A possible mechanism of the membrane formation. A thiolipid vesicle suspension prepared in 100 mM KCl by sonication was applied to the gold surface. The times in min after the application of the vesicle suspension are indicated. (Yokoi and Asami, unpublished data).

**Fig.14** Measurement techniques for transmembrane admittance of biological cells. (a) The internal electrode method and (b) the patch pipette method.

**Fig.15** Dielectric relaxation of a W/O emulsion. (a) Frequency dependence of the relative permittivity  $\varepsilon'$  and the loss factor  $\varepsilon''$ , (b) the complex plane plots. The open circles are data points, the solid lines were calculated from Hanai's mixture equation (Eq.39) and the dotted lines were from Wagner's mixture equation (Eq.23). (From Hanai et al., 1982 [79]) Reproduced by permission of Springer-Verlag GmbH & Co. KG.

**Fig.16** Dielectric relaxation of cation-exchange resin beads (Amberlite® IR-120B, Rohm and Hass) in distilled water. The open and solid circles are data points and The solid lines are calculated from Eq.39 with  $\varepsilon_a=78$ ,  $\kappa_a=0.0098$  S/m,  $\varepsilon_p=40$ ;  $\kappa_p=3.3$  S/m and  $\Phi=0.56$ . (Zhao and Asami, unpublished data)

**Fig.17** Dielectric relaxation of dense suspensions of polystyrene microcapsules. (a) The solution of the external medium was changed from 1m M KCl to distilled water, (b) the solution of the inner phase was changed from 1mM KCl to distilled water. The

measured relaxation was compared with the theoretical curves calculated from Eqs.39 and 52 in (c) the frequency dependence profile and (d) the complex plane plots. (From Hanai et al., 1988 [93] and Zhang et al., 1984 [92]) Reproduced by permission of Taylor & Francis Ltd. and Springer-Verlag GmbH & Co. KG.

**Fig.18** Dielectric relaxation of LUV and MLV suspensions. The LUV (or Cell-size liposome) suspension was prepared by the method of Kim and Martin [99]. The lipid used was a mixture of phosphatidylcholine, cholesterol, cardiolipin and triolein (4:4:1:1). The mean radius was about 3  $\mu\text{m}$  and the volume fraction was 0.30. The MLV suspension was prepared from DMPC according to Bangam's method [100]. Volume fraction was 0.23. The external medium for both the LUV and the MLV was 100 mM KCl containing 10 mM phosphate buffer (pH 7.0). Measurements were made at 25°C. (Asami, unpublished data)

**Fig.19** The effective relative permittivity of (a) spherical erythrocyte and (b) lymphocyte calculated from the dielectric relaxation of their cell suspensions using Hanai's mixture equation. The open circles are data points. The solid lines were calculated using (a) the single-shell model and (b) the double-shell model, which are illustrated as insets. (c) and (d): the complex plane plots for (a) and (b), respectively. (From Asami et al., 1989 [102]) Reproduced by permission of Elsevier Science Ltd.

**Fig.20** Composite-cell model and ellipsoidal cell model. (a) Double-shell model, (b) double-shell model including vesicles, (c) ellipsoidal cell model.

**Fig.21** Dielectric relaxation of suspensions of fission yeast cells of rod-like shape with different mean cell lengths: (a) 14.2  $\mu\text{m}$ , (b) 29.4  $\mu\text{m}$  and (c) 42.0  $\mu\text{m}$ . The mean cell diameter was 4.1  $\mu\text{m}$ . The dielectric spectra observed (open circles) are composed of two relaxation terms (solid lines). (From Asami, 1999 [110]) Reproduced by permission of Elsevier Science Ltd.

**Fig.22** The electrode configurations used for single-particle analysis: (a) parallel plate capacitor for dielectric spectroscopy, (b) dielectrophoresis, (c) electrorotation and (d) scanning dielectric microscopy. Applied ac voltages are indicated.

**Fig.23** The Clausius-Mossotti factor  $K$  calculated for a water droplet in an oil phase of (W/O type) and for an oil droplet in a water phase (O/W type). The real part (a) and the imaginary part (b) of  $K$  are plotted against frequency. The parameter values used are as follows. For W/O type, the relative permittivity of the oil phase  $\epsilon_a$  is varied as 2, 10 and 35,  $\kappa_a=10^{-7}$  S/m,  $\epsilon_p=80$ ,  $\kappa_p=0.001$  S/m. For O/W type, the relative permittivity of the oil droplet  $\epsilon_p$  is varied as 2, 10 and 35,  $\kappa_p=10^{-7}$  S/m,  $\epsilon_a=80$ ,  $\kappa_a=0.001$  S/m.

**Fig.24** The Clausius-Mossotti factor  $K$  calculated for particles in which membranes (relative permittivity  $\epsilon_m$ , conductivity  $\kappa_m$ , and thickness  $d_m$ ) and inter-membrane spaces

$(\epsilon_{im}, \kappa_{im}, d_{im})$  are alternately arranged. Frequency dependence of (a) the real and (b) the imaginary part of  $K$ , and (c) the complex plane plots. The parameter values used are the same as in Fig.9 except those of the external medium ( $\epsilon_a=80$  and  $\kappa_a=0.001$  S/m), i.e.,  $\epsilon_m=5$  and  $\kappa_m=0$  S/m for the membrane,  $\epsilon_{im}=80$  and  $\kappa_{im}=0.1$  S/m for the inter-membrane phase,  $\epsilon_c=80$  and  $\kappa_c=0.1$  S/cm for the core phase,  $d_m=7$  nm, and  $d_{im}=10$  nm. The particle radius is  $10\text{ }\mu\text{m}$ . The number of membranes  $n_m$  is varied as: 1, 2, 5, 20 and 200.

**Fig.25** Images of capacitance and conductance of a single microcapsule in water. (a) Line-scan images obtained by scanning a probe electrode along the line through the top of the microcapsule and (b) raster-scan images where the probe frequencies are indicated. The microcapsule of about  $800\text{ }\mu\text{m}$  in diameter had an aqueous inner phase of 3 mM KCl and a polystyrene shell of about  $3\text{ }\mu\text{m}$  thick. (From Asami, 1998 [118]). Reproduced by permission of Springer-Verlag GmbH & Co. KG.

**Table 1** Formalism of dielectric relaxation

Formalism	Complex permittivity	Real and imaginary parts
Debye Semicircular arc rule	$\epsilon^* = \epsilon_h + \frac{\Delta\epsilon}{1 + j\omega\tau}$	$\epsilon' = \epsilon_h + \frac{\Delta\epsilon}{1 + (\omega\tau)^2}$ $\epsilon'' = \frac{\Delta\epsilon\omega\tau}{1 + (\omega\tau)^2}$
Cole-Cole Circular arc rule	$\epsilon^* = \epsilon_h + \frac{\Delta\epsilon}{1 + (j\omega\tau)^{1-\alpha}}$ ( $0 < \alpha < 1$ )	$\epsilon' = \epsilon_h + \frac{\Delta\epsilon [1 + (\omega\tau)^{(1-\alpha)} \cos\{\pi(1-\alpha)/2\}]}{1 + 2(\omega\tau)^{(1-\alpha)} \cos\{\pi(1-\alpha)/2\} + (\omega\tau)^{2(1-\alpha)}}$ $\epsilon'' = \frac{\Delta\epsilon(\omega\tau)^{(1-\alpha)} \sin\{\pi(1-\alpha)/2\}}{1 + 2(\omega\tau)^{(1-\alpha)} \cos\{\pi(1-\alpha)/2\} + (\omega\tau)^{2(1-\alpha)}}$
Davidson-Cole Skewed arc rule	$\epsilon^* = \epsilon_h + \frac{\Delta\epsilon}{(1 + j\omega\tau)^\beta}$ ( $0 < \beta < 1$ )	$\epsilon' = \epsilon_h + \Delta\epsilon \cos(\beta\theta) \cos^\beta \theta$ $\epsilon'' = \Delta\epsilon \sin(\beta\theta) \cos^\beta \theta$ $\theta = \tan^{-1}(\omega\tau)$
Havriliak- Negami	$\epsilon^* = \epsilon_h + \frac{\Delta\epsilon}{[1 + (j\omega\tau)^{(1-\alpha)}]^\beta}$ ( $0 < \alpha < 1, 0 < \beta < 1$ )	$\epsilon' = \epsilon_h + r^{-\beta/2} \Delta\epsilon \cos(\beta\theta)$ $\epsilon'' = r^{-\beta/2} \Delta\epsilon \sin(\beta\theta)$ $r = [1 + (\omega\tau)^{(1-\alpha)} \sin(\alpha\pi/2)]^2 + [(\omega\tau)^{(1-\alpha)} \cos(\alpha\pi/2)]^2$ $\theta = \tan^{-1} \frac{(\omega\tau)^{(1-\alpha)} \cos(\alpha\pi/2)}{1 + (\omega\tau)^{(1-\alpha)} \sin(\alpha\pi/2)}$

**Table 2** Dielectric mixture equations for two-phase systems.

Dielectric mixture equations	Vol. frac.	Eqs. in text
Ellipsoids oriented to a given direction		
$\epsilon^* = \epsilon_a^* \left[ 1 + \Phi \sum_{k=x,y,z} \frac{\epsilon_p^* - \epsilon_a^*}{\epsilon_a^* + (\epsilon_p^* - \epsilon_a^*) L_k} \cos^2 \varphi_k \right]$	$\Phi \ll 1$	17
The $k$ -axis is parallel to $E$		
$\epsilon^* = \epsilon_a^* \left[ 1 + \Phi \frac{\epsilon_p^* - \epsilon_a^*}{\epsilon_a^* + (\epsilon_p^* - \epsilon_a^*) L_k} \right]$	$\Phi \ll 1$	19
$\frac{\epsilon^* - \epsilon_a^*}{\epsilon_a^* + (\epsilon_p^* - \epsilon_a^*) L_k} = \Phi \frac{\epsilon_p^* - \epsilon_a^*}{\epsilon_a^* + (\epsilon_p^* - \epsilon_a^*) L_k}$	$\Phi < 0.1$	21
$1 - \Phi = \left( \frac{\epsilon^* - \epsilon_p^*}{\epsilon_a^* - \epsilon_p^*} \right) \left( \frac{\epsilon_a^*}{\epsilon^*} \right)^{L_k}$		38

Random orientation

$$\varepsilon^* = \varepsilon_a^* \left[ 1 + \frac{1}{3} \Phi \sum_{k=x,y,z} \frac{\varepsilon_p^* - \varepsilon_a^*}{\varepsilon_a^* + (\varepsilon_p^* - \varepsilon_a^*) L_k} \right] \quad \Phi \ll 1 \quad 20$$

$$\frac{\varepsilon^* - \varepsilon_a^*}{\varepsilon^* + 2\varepsilon_a^*} = \frac{1}{9} \Phi \sum_{k=x,y,z} \frac{\varepsilon_p^* - \varepsilon_a^*}{\varepsilon_a^* + (\varepsilon_p^* - \varepsilon_a^*) L_k} \quad \Phi < 0.1 \quad 22$$

$$1 - \Phi = \left( \frac{\varepsilon_a^* - \alpha \varepsilon_p^*}{\varepsilon^* - \alpha \varepsilon_p^*} \right)^A \left( \frac{\varepsilon_a^* - \beta \varepsilon_p^*}{\varepsilon^* - \beta \varepsilon_p^*} \right)^B \left( \frac{\varepsilon^* - \varepsilon_p^*}{\varepsilon_a^* - \varepsilon_p^*} \right) \left( \frac{\varepsilon_a^*}{\varepsilon^*} \right)^{3T} \quad 28$$

Spheres ( $L_x=L_y=L_z=1/3$ )

$$\varepsilon^* = \varepsilon_a^* \left[ 1 + 3\Phi \frac{\varepsilon_p^* - \varepsilon_a^*}{2\varepsilon_a^* + \varepsilon_p^*} \right] \quad \Phi \ll 1$$

$$\frac{\varepsilon^* - \varepsilon_a^*}{\varepsilon^* + 2\varepsilon_a^*} = \Phi \frac{\varepsilon_p^* - \varepsilon_a^*}{\varepsilon^* + 2\varepsilon_p^*} \quad \Phi < 0.1 \quad 23$$

$$1 - \Phi = \left( \frac{\varepsilon^* - \varepsilon_p^*}{\varepsilon_a^* - \varepsilon_p^*} \right) \left( \frac{\varepsilon_a^*}{\varepsilon^*} \right)^{1/3} \quad 39$$

Cylinders ( $L_x=L_y=1/2$ ) oriented parallel to  $E$ 

$$\varepsilon^* = \varepsilon_a^* \left[ 1 + 2\Phi \frac{\varepsilon_p^* - \varepsilon_a^*}{\varepsilon_a^* + \varepsilon_p^*} \right] \quad \Phi \ll 1$$

$$\frac{\varepsilon^* - \varepsilon_a^*}{\varepsilon^* + \varepsilon_a^*} = \Phi \frac{\varepsilon_p^* - \varepsilon_a^*}{\varepsilon^* + \varepsilon_p^*} \quad \Phi < 0.1 \quad 24$$

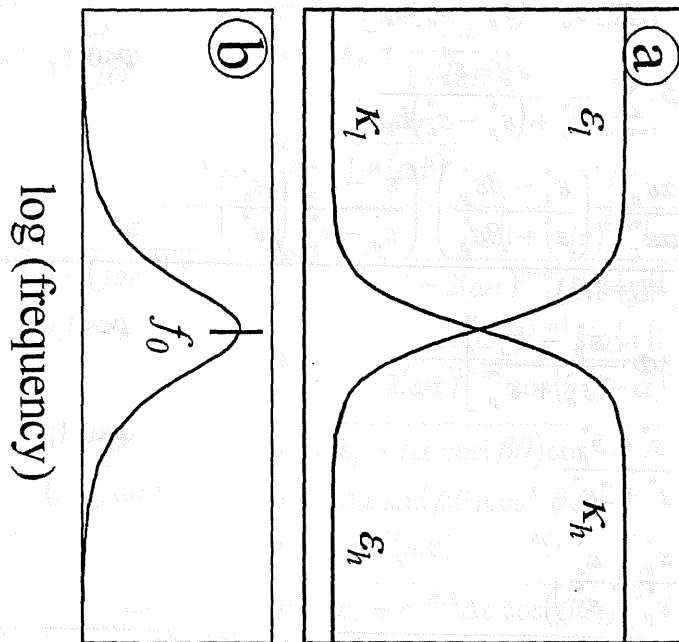
$$1 - \Phi = \left( \frac{\varepsilon^* - \varepsilon_p^*}{\varepsilon_a^* - \varepsilon_p^*} \right) \left( \frac{\varepsilon_a^*}{\varepsilon^*} \right)^{1/2} \quad 40$$

Lamellars ( $L_z=1$ )

$$\frac{1}{\varepsilon^*} = (1 - \Phi) \frac{1}{\varepsilon_a^*} + \Phi \frac{1}{\varepsilon_p^*} \quad 25$$



Loss factor      Rel. permittivity



Conductivity

Loss factor

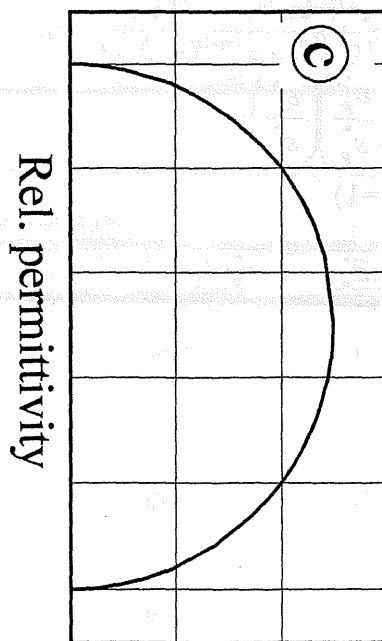
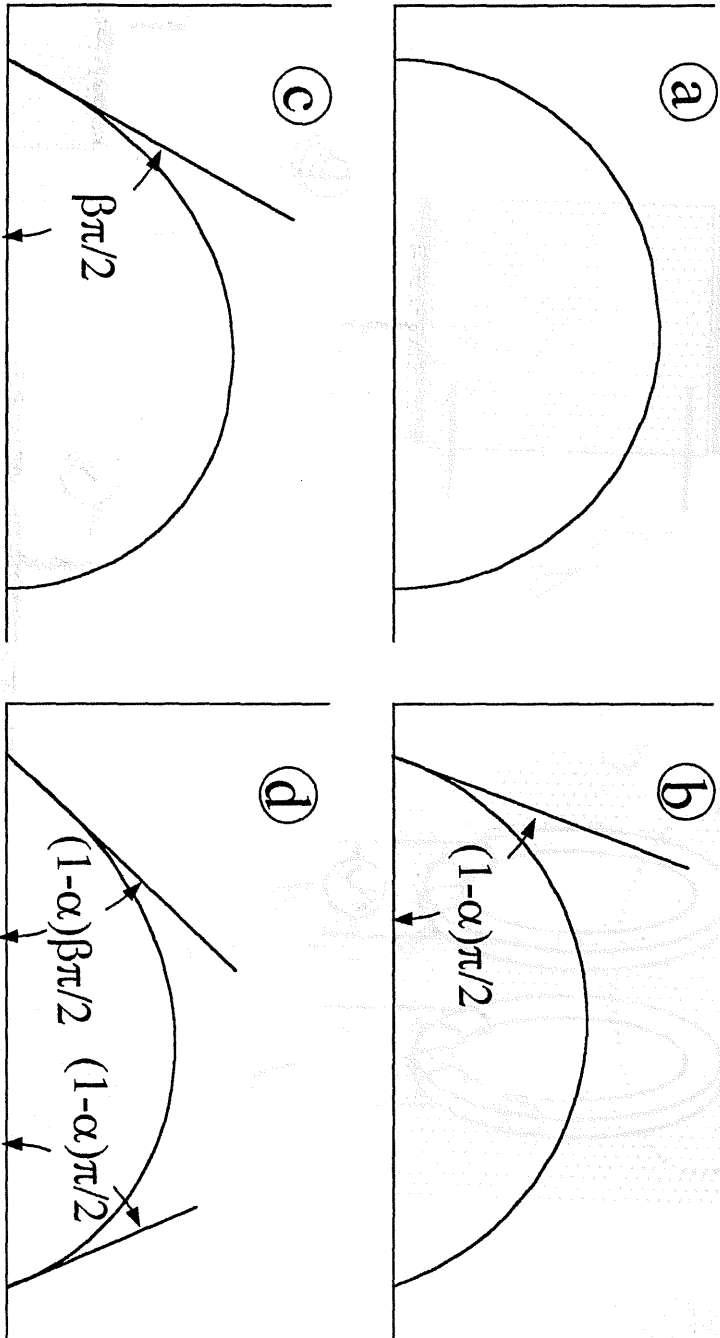
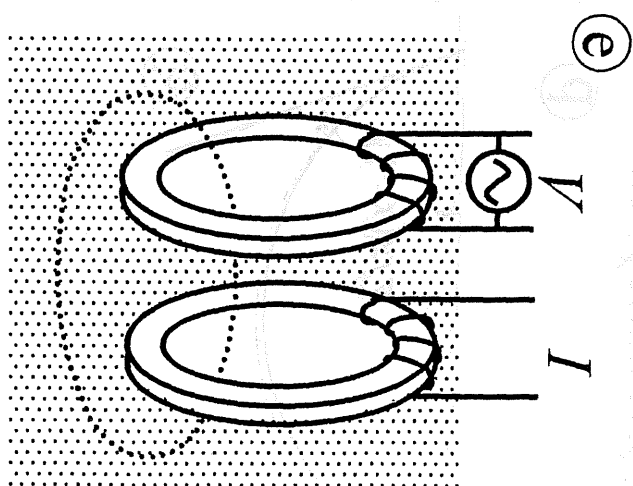
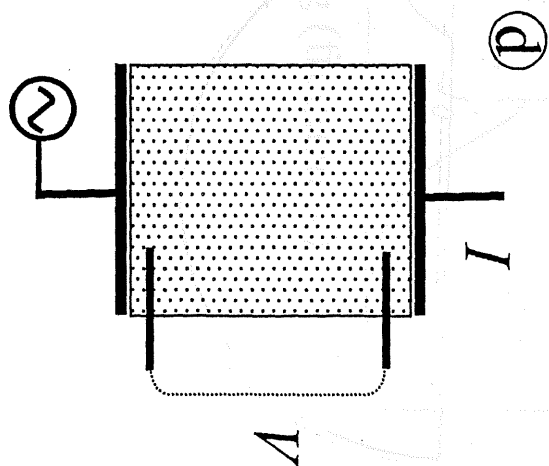
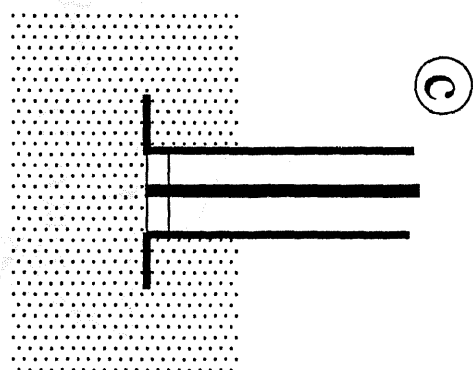
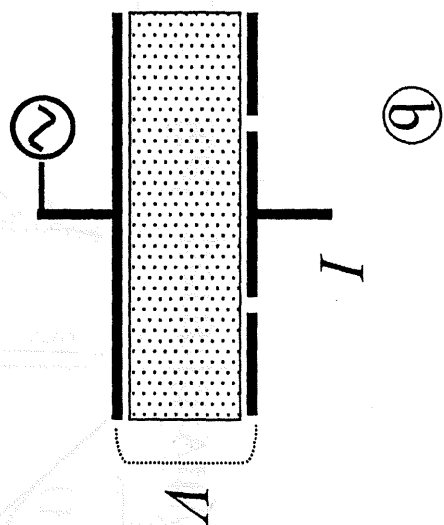
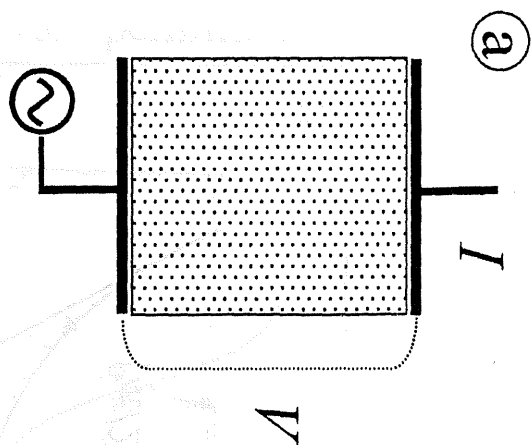


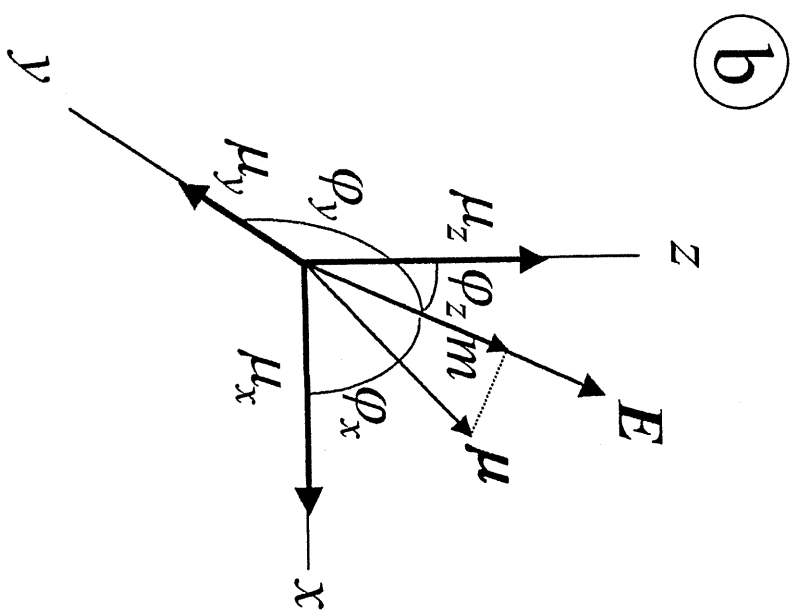
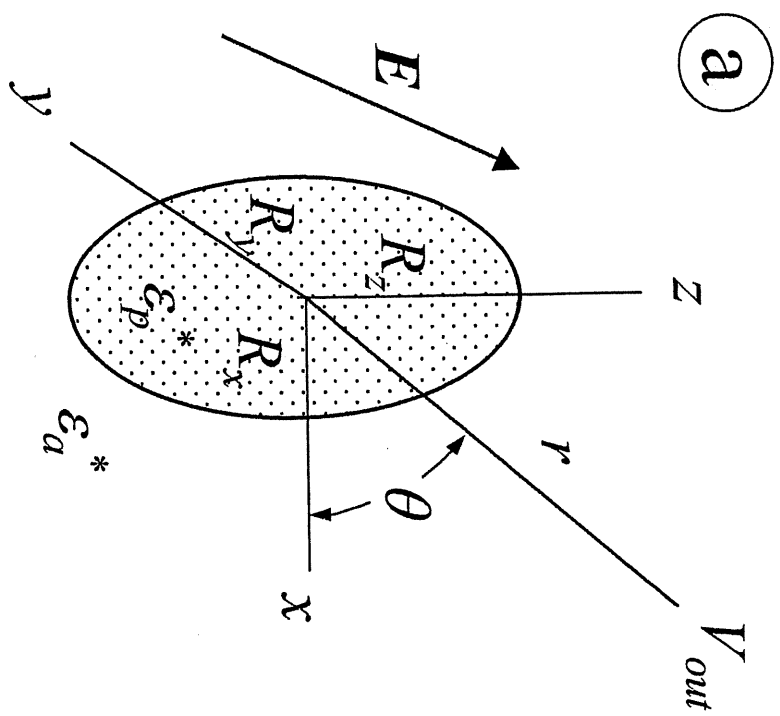
Fig. 1

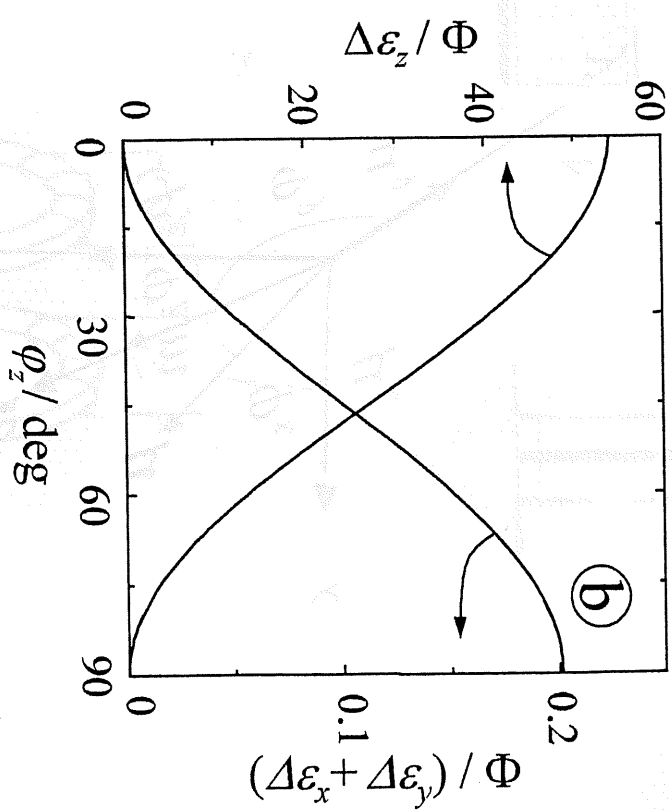
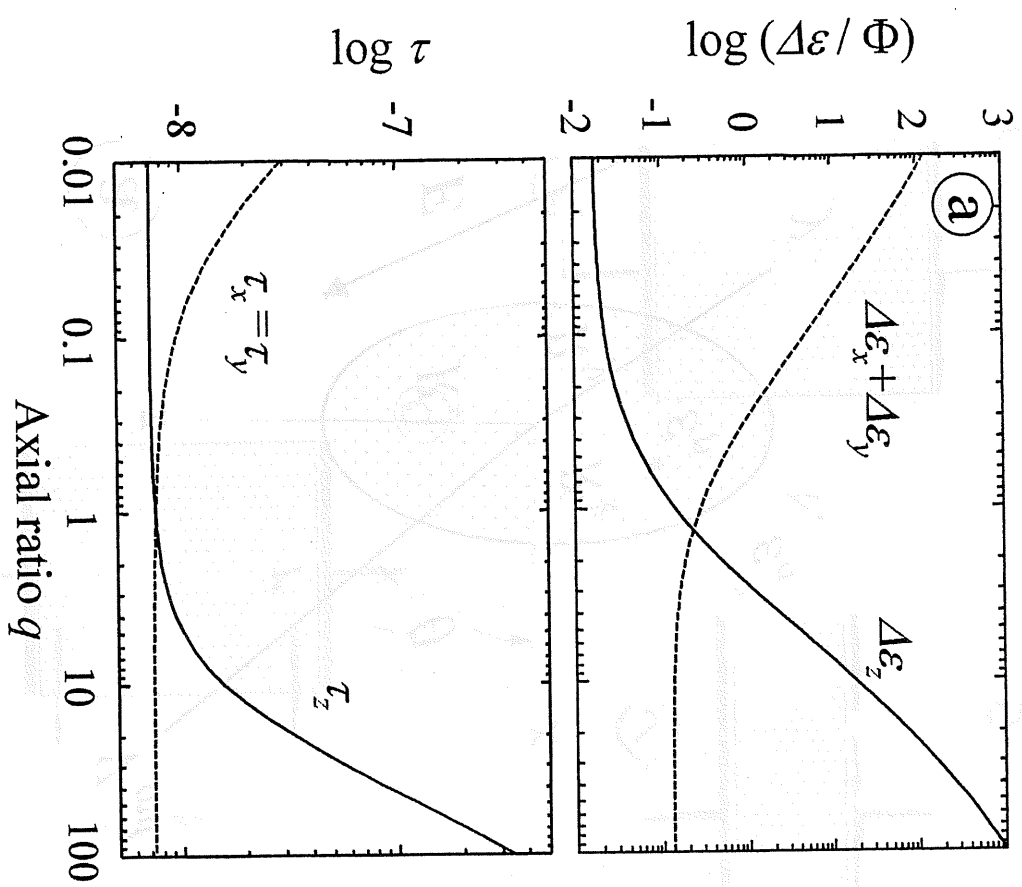
Loss factor

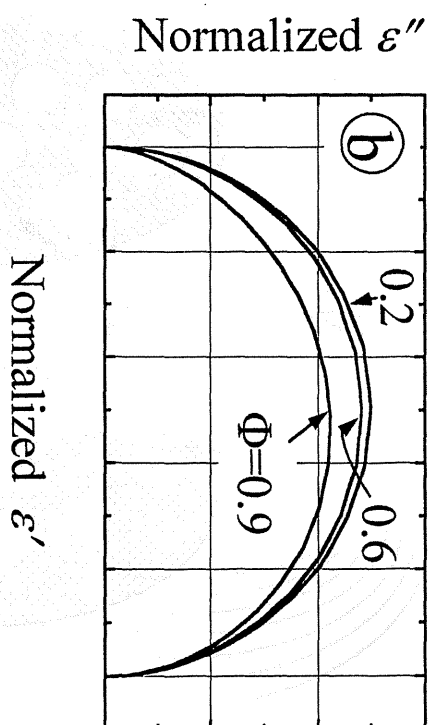
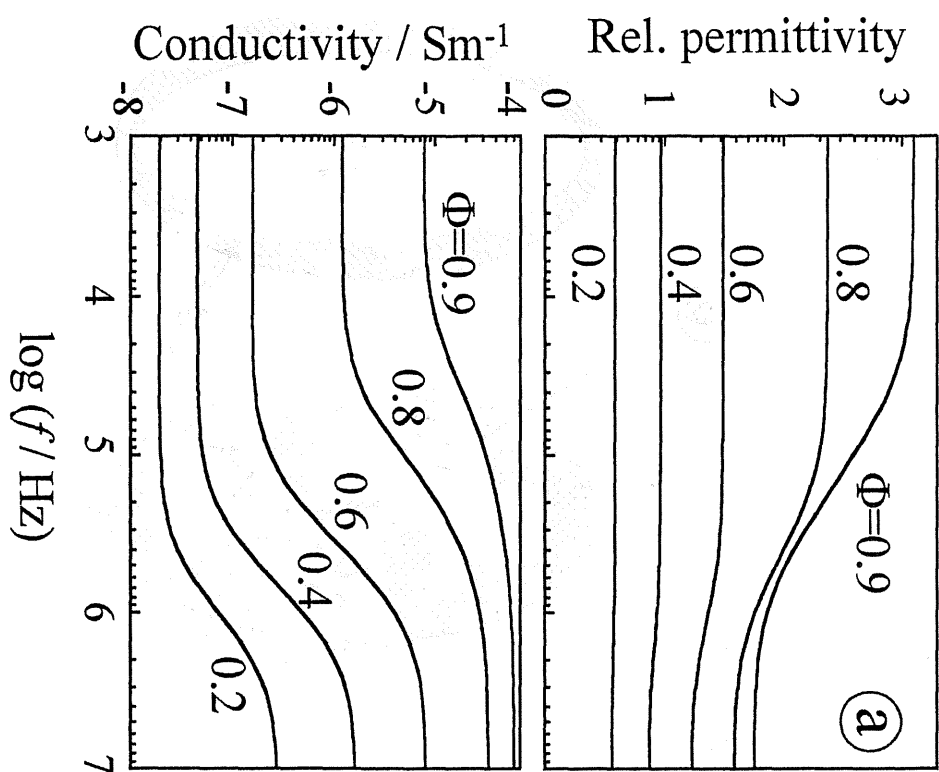


Rel. permittivity

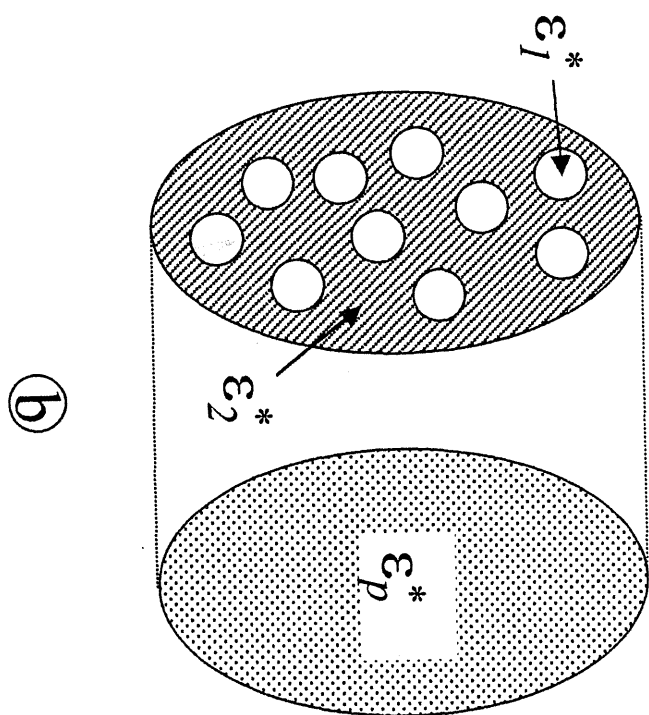
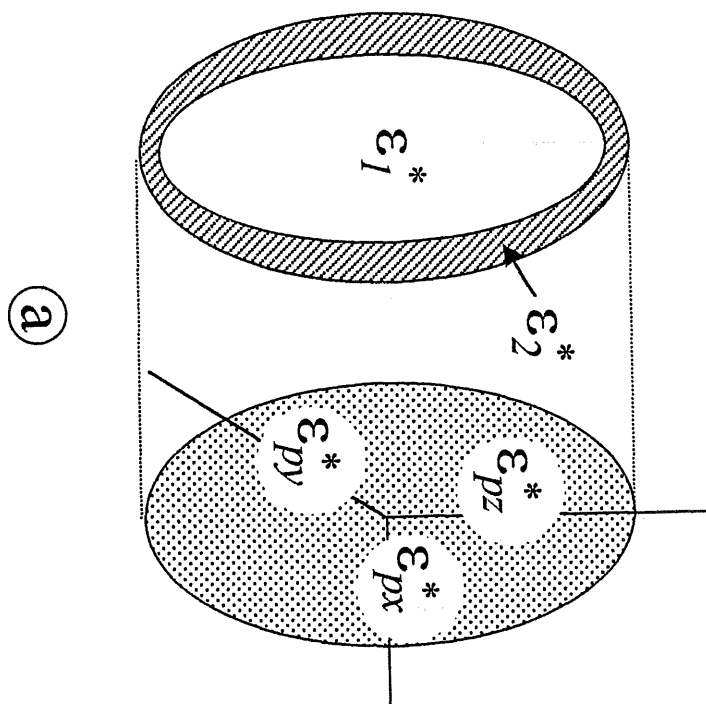


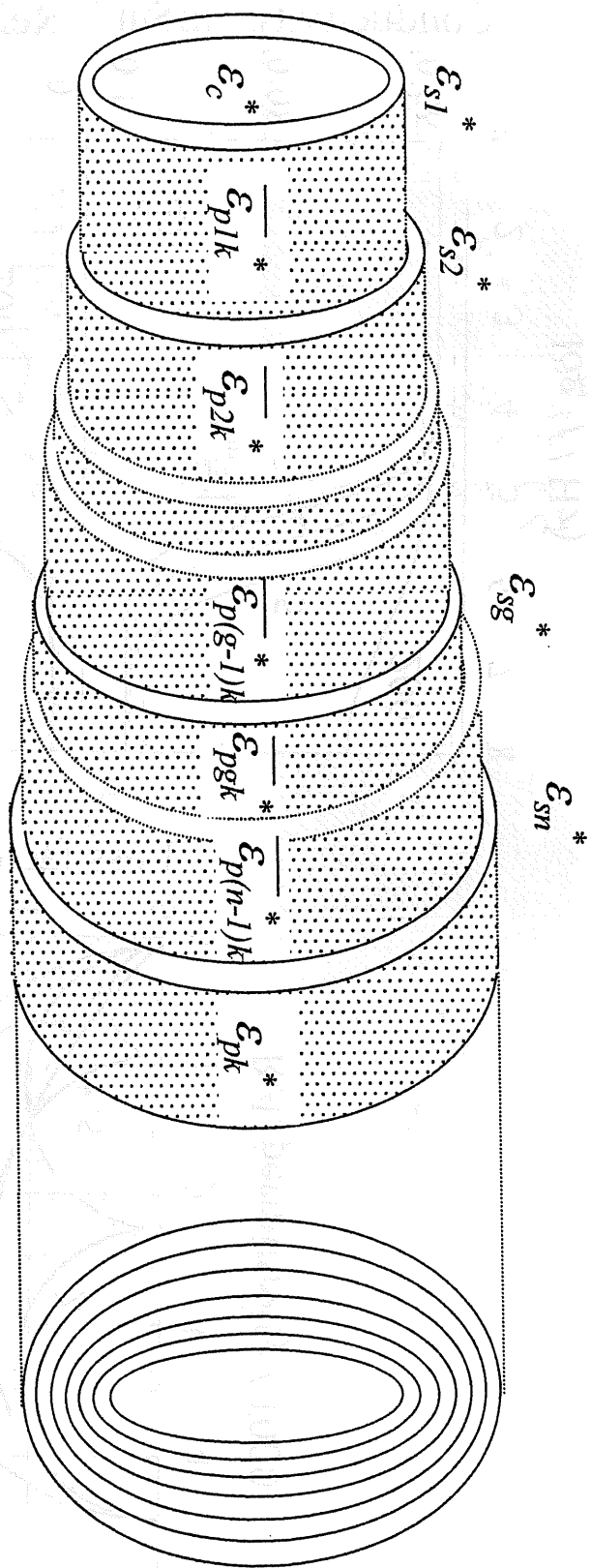


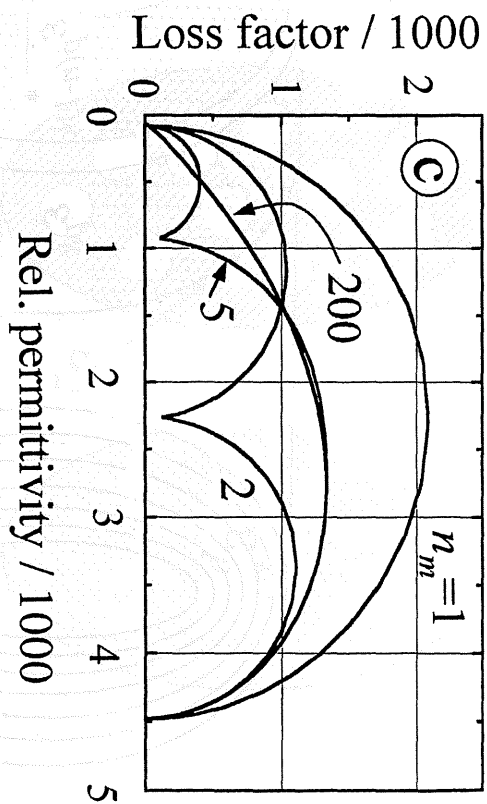
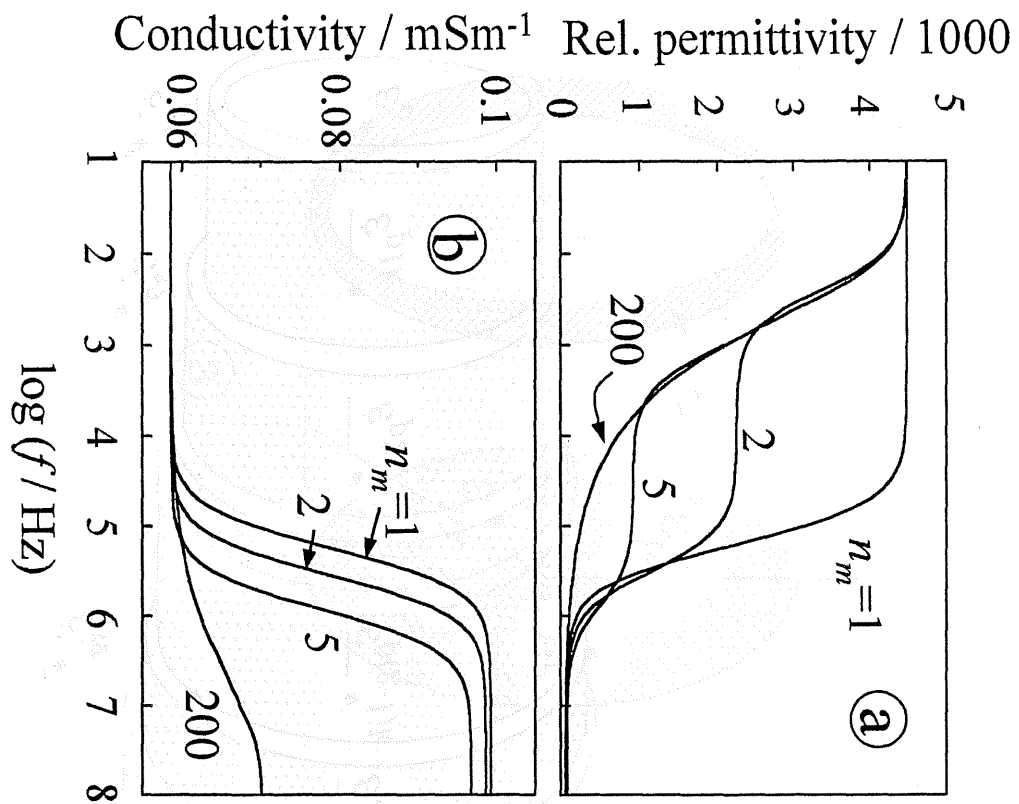




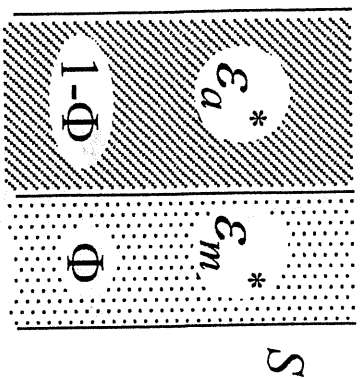




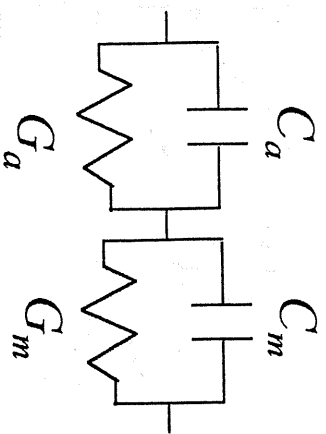




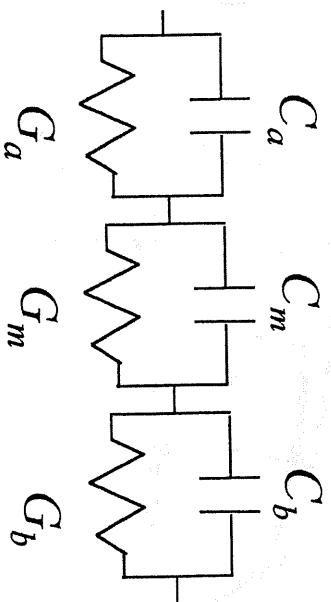
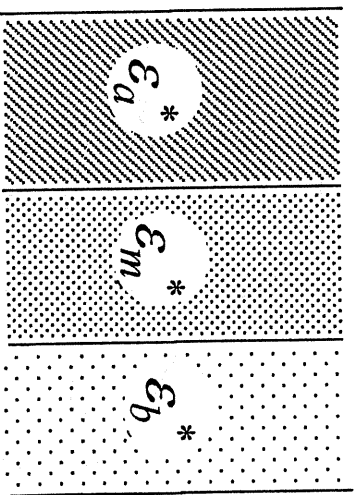
a

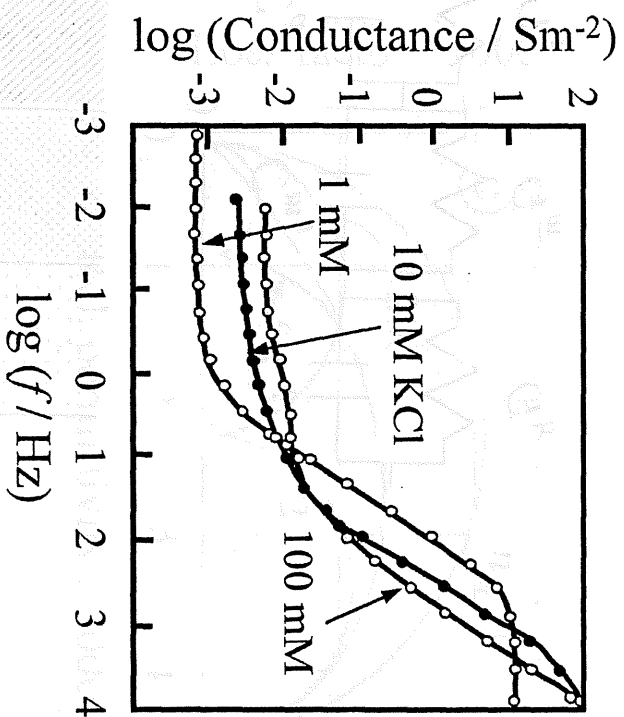
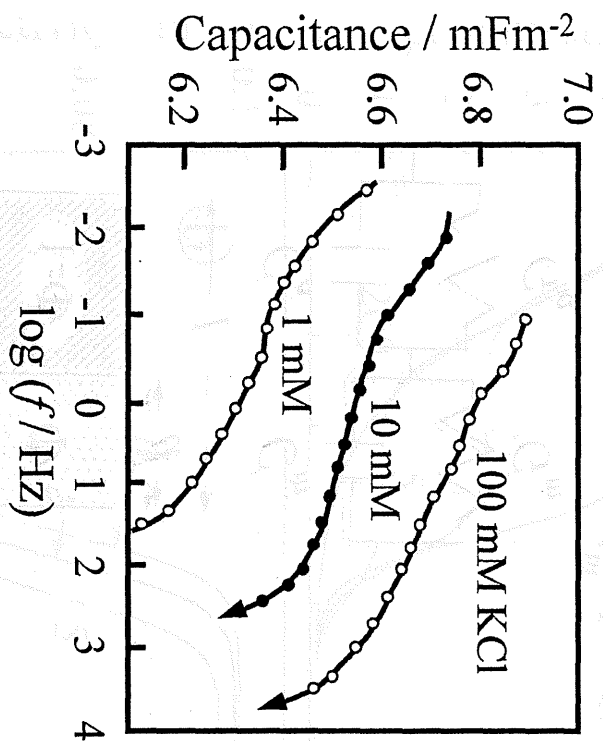


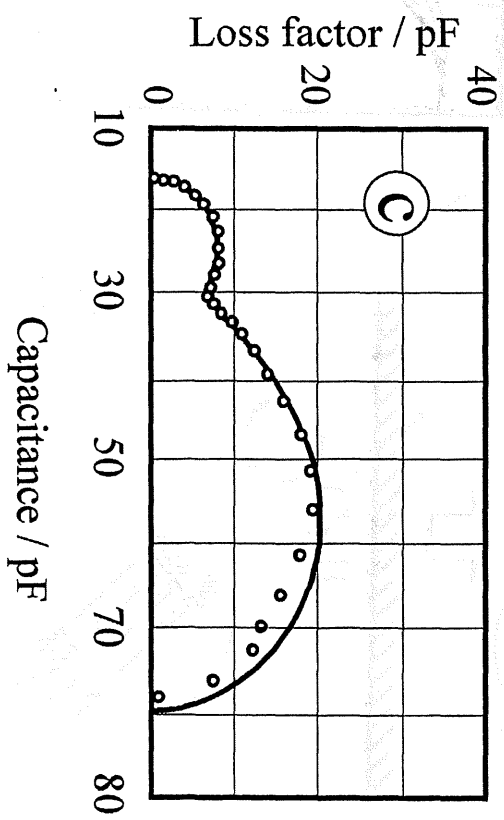
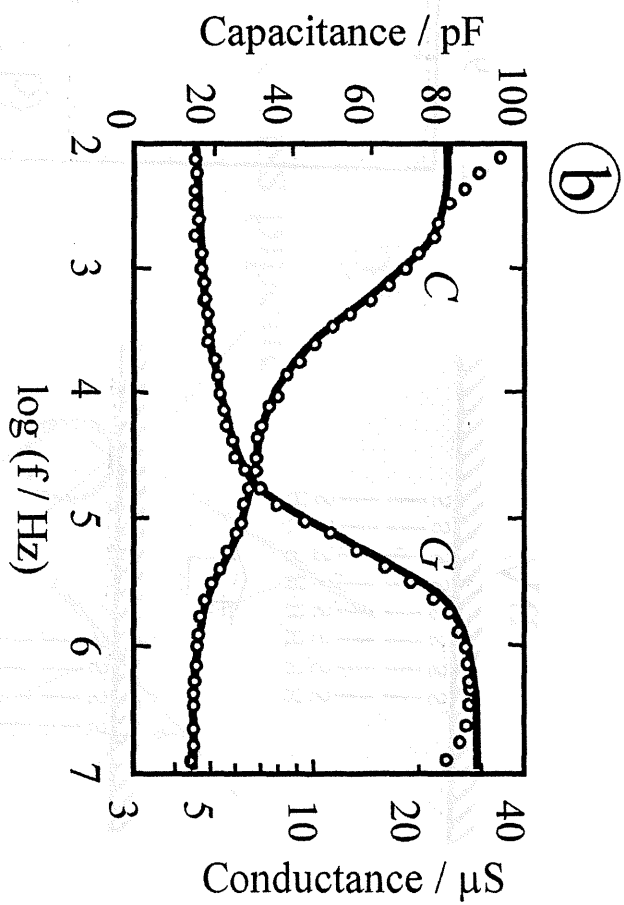
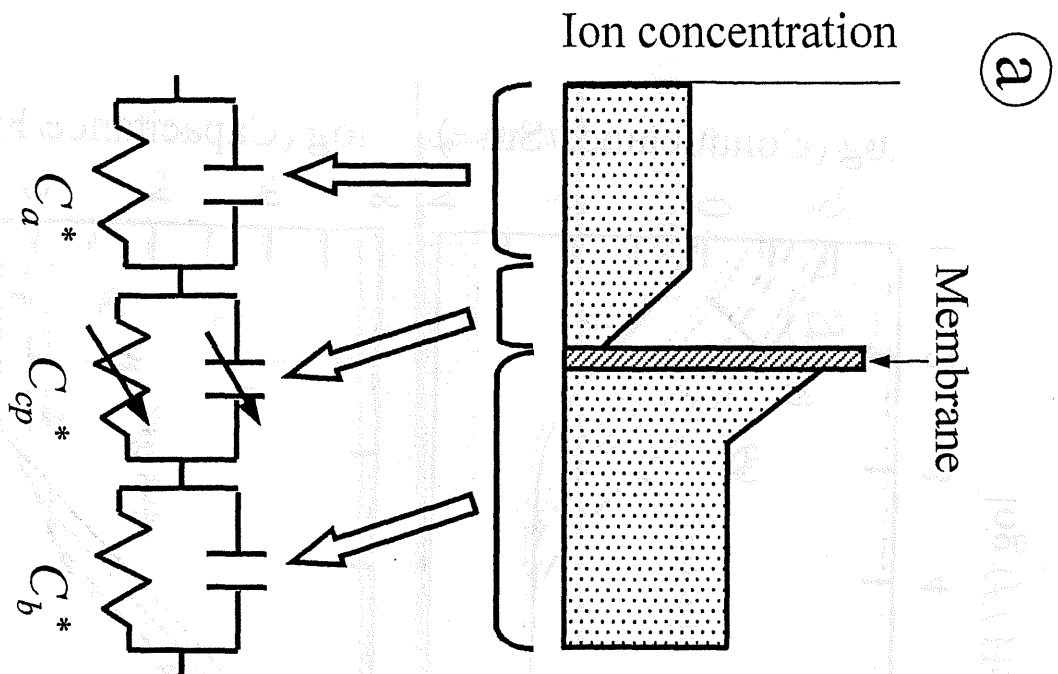
$l$   
 $d$



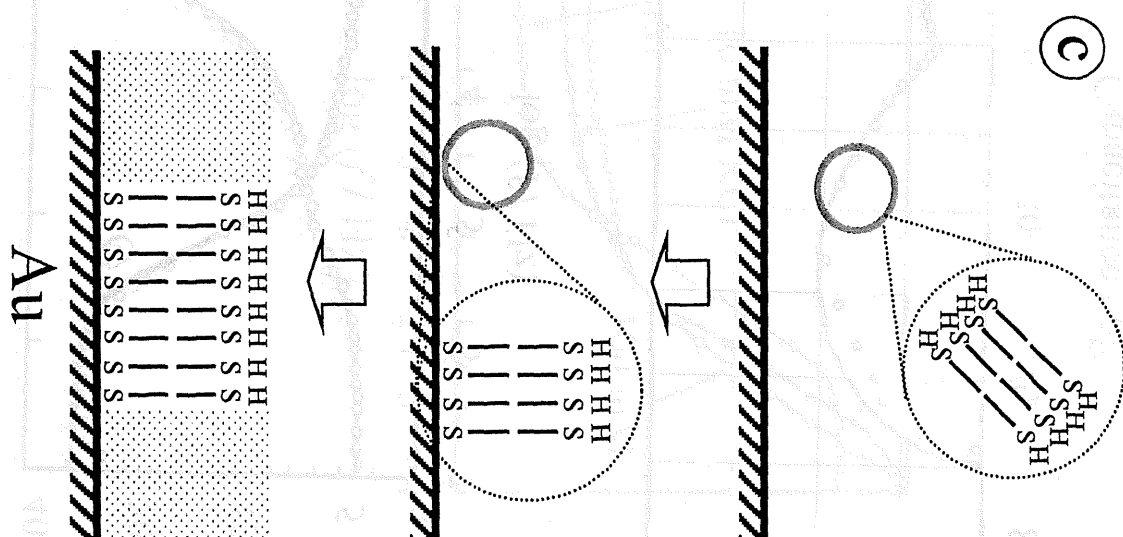
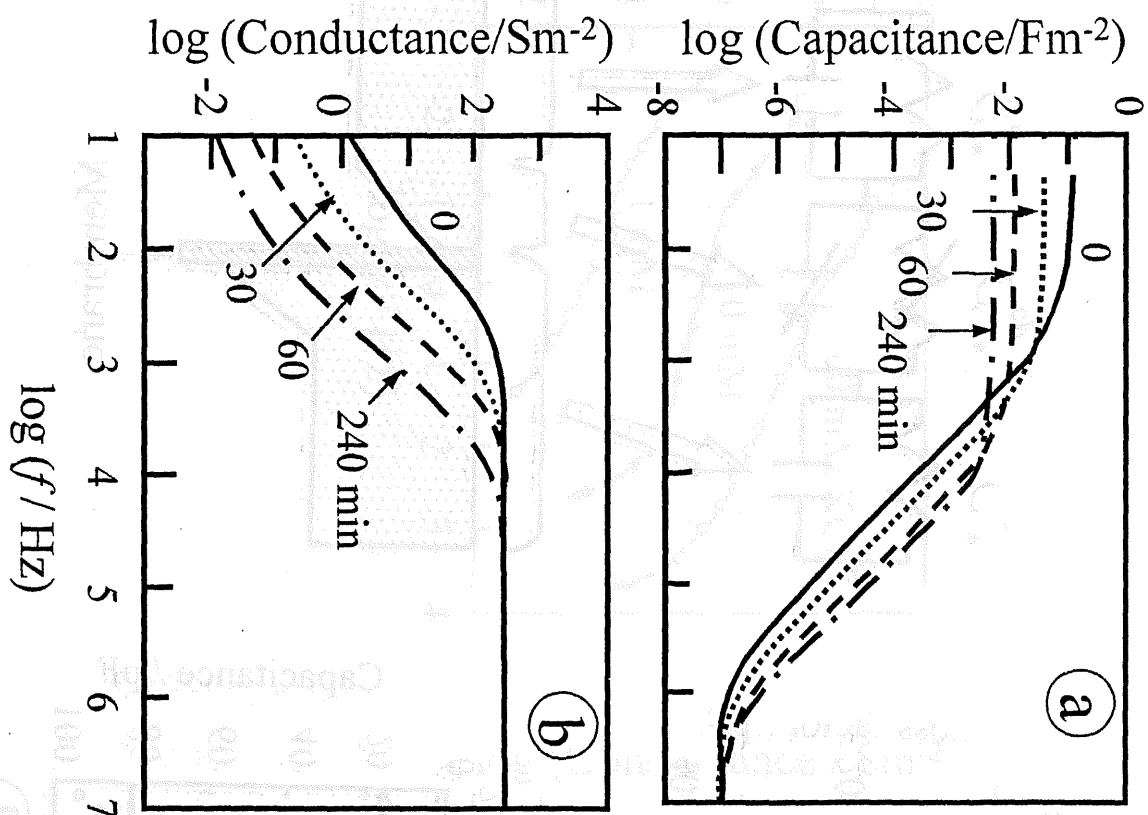
b

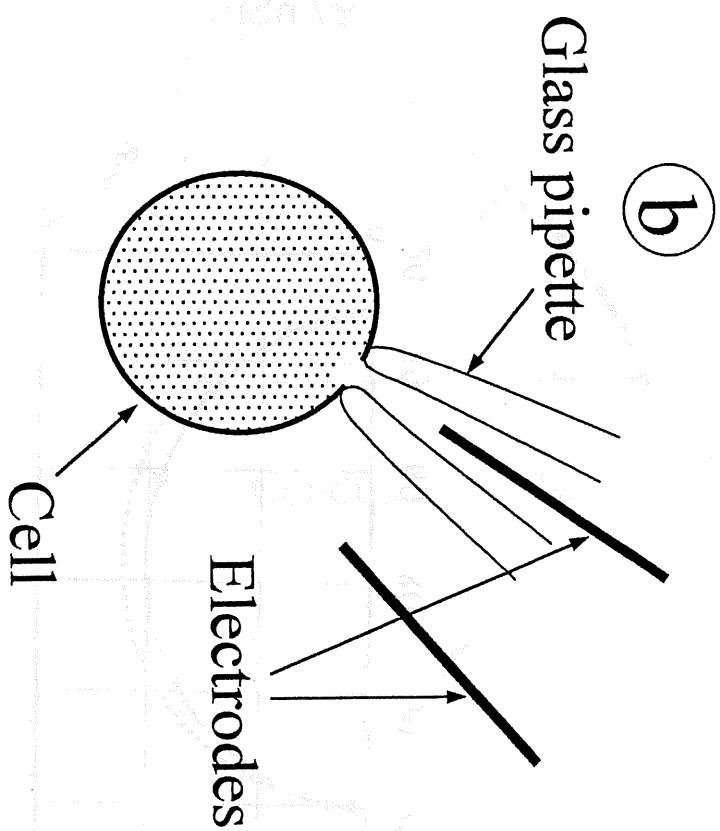
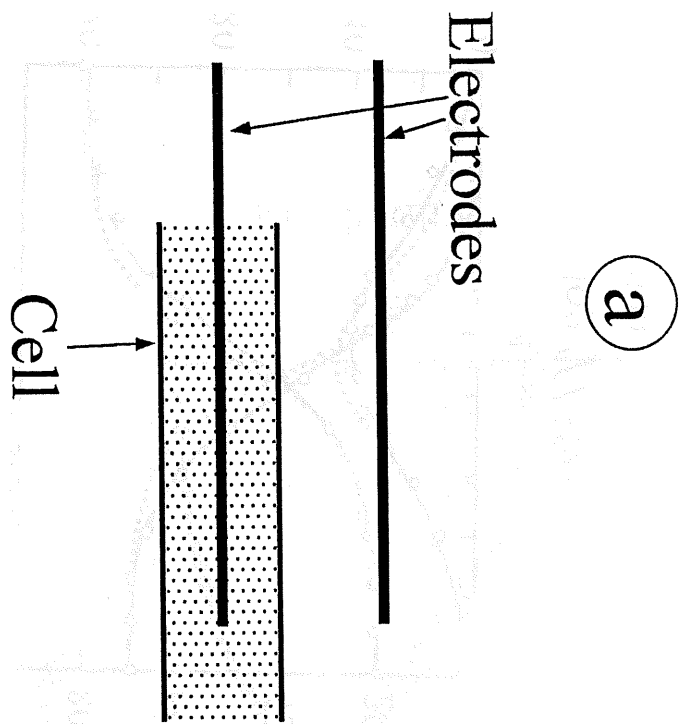


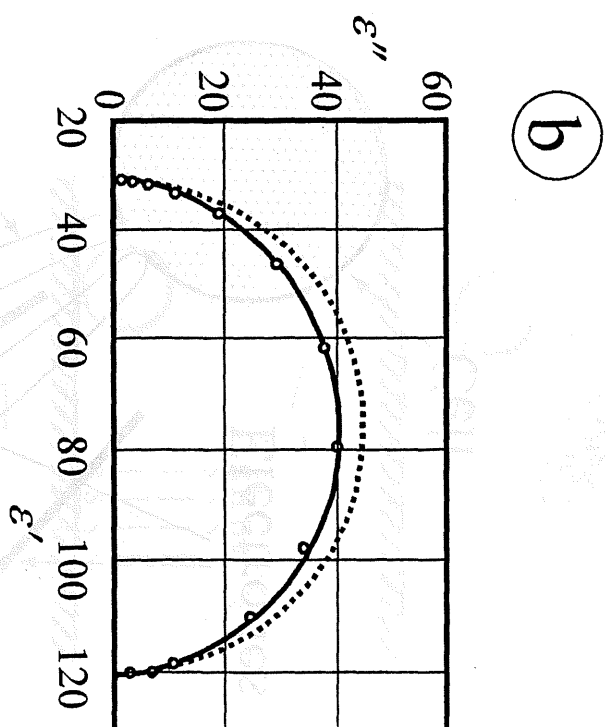
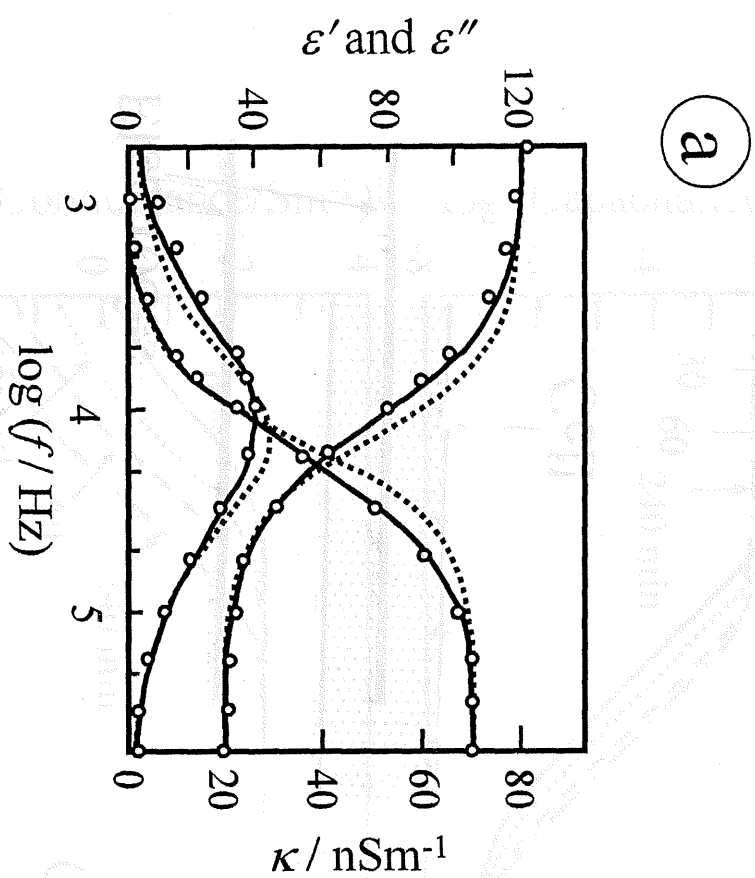


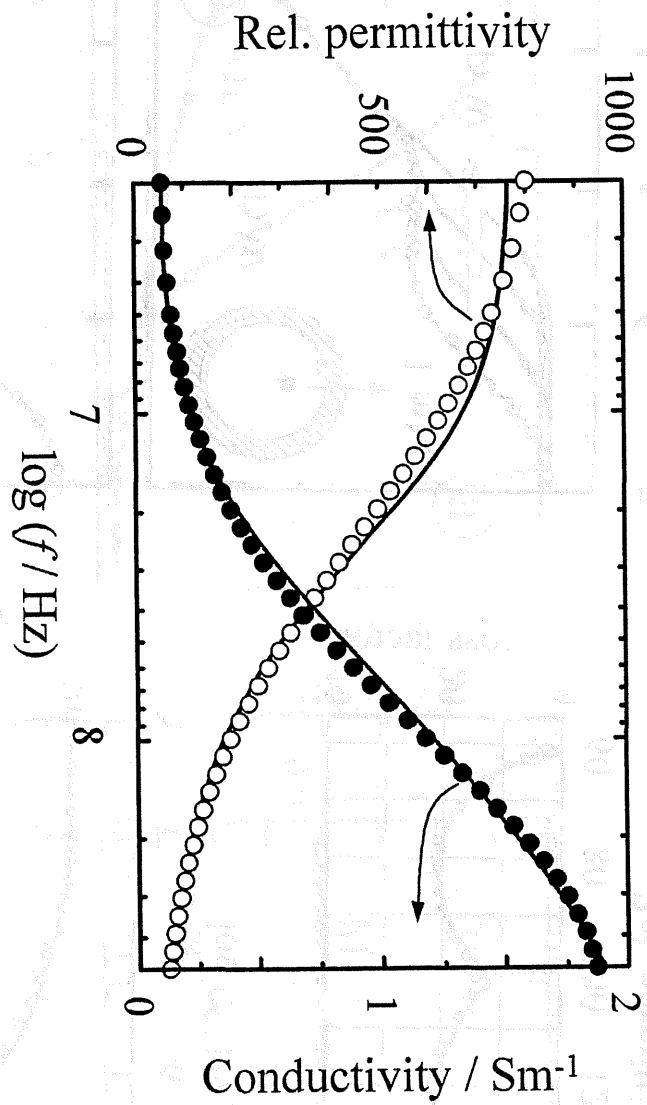


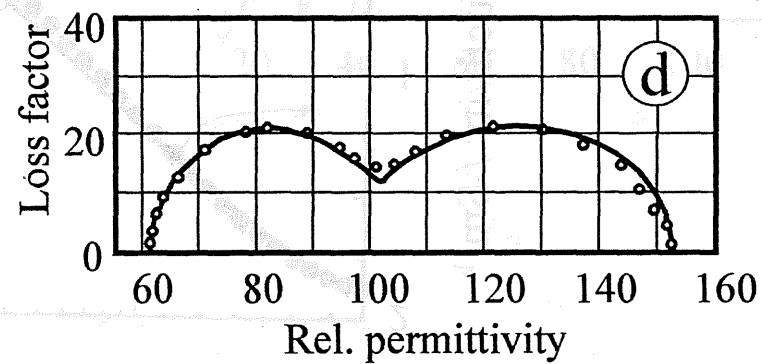
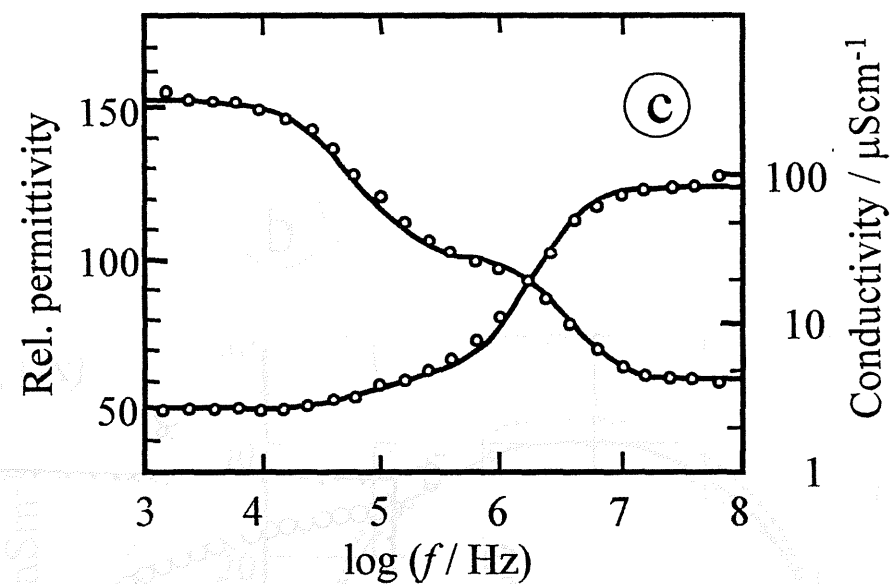
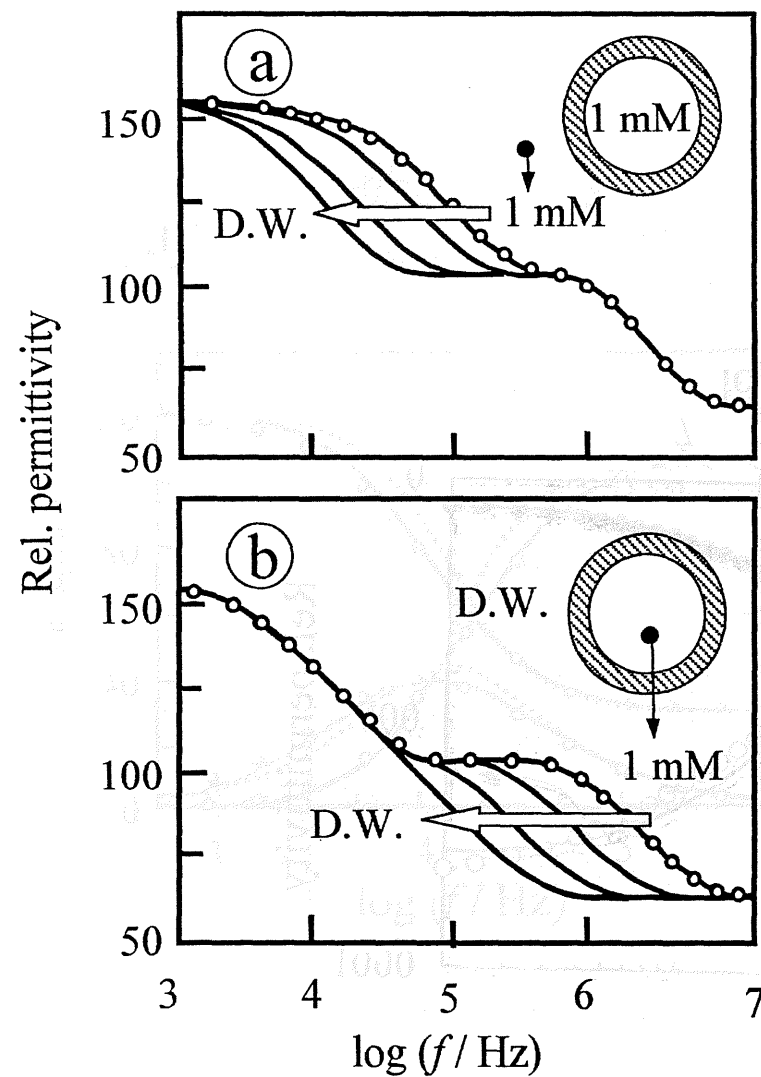


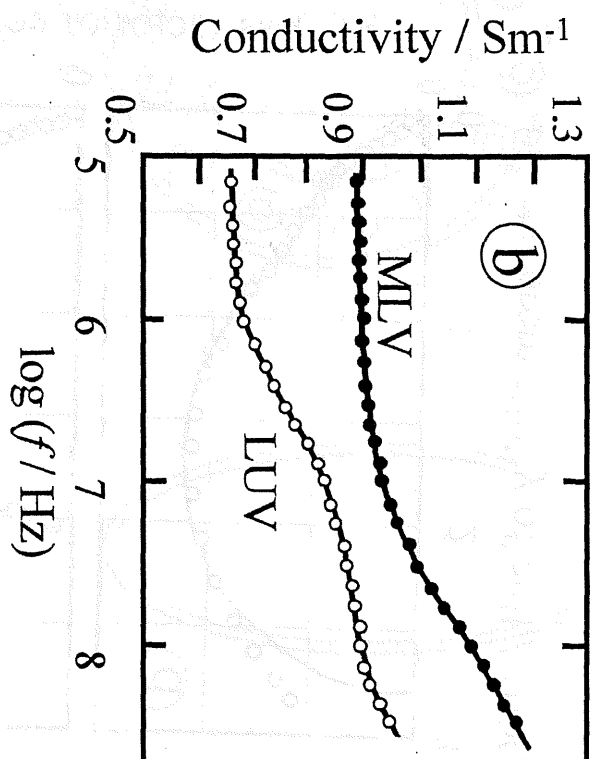
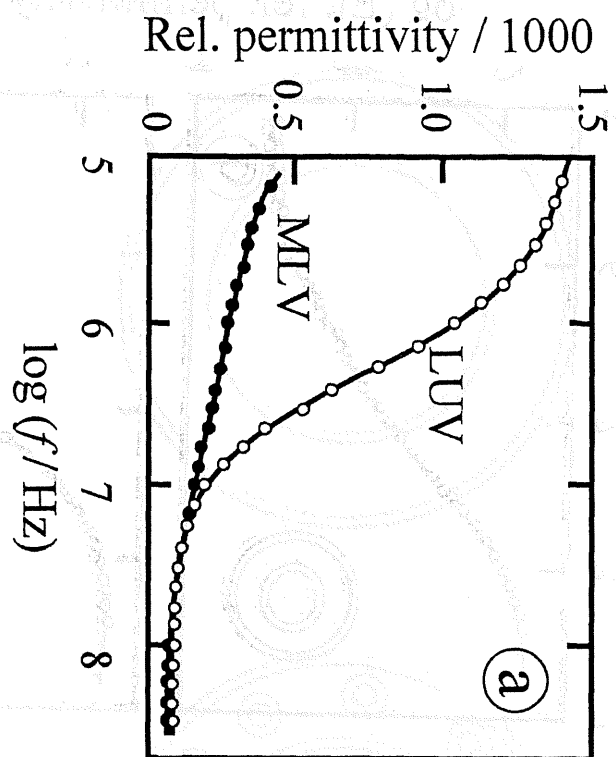




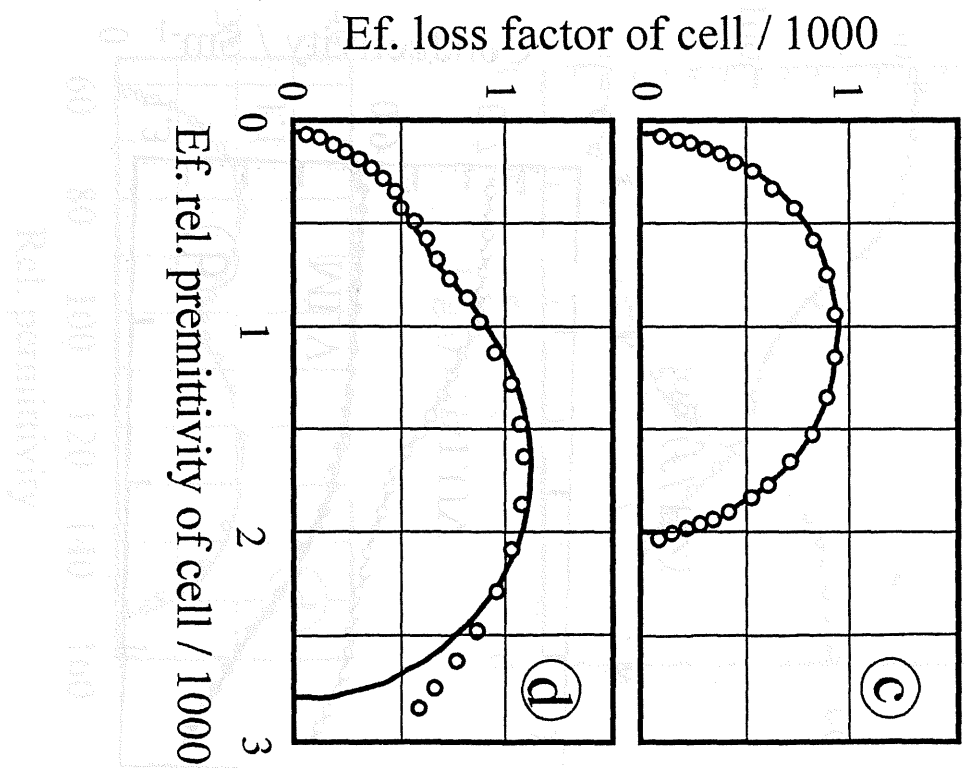
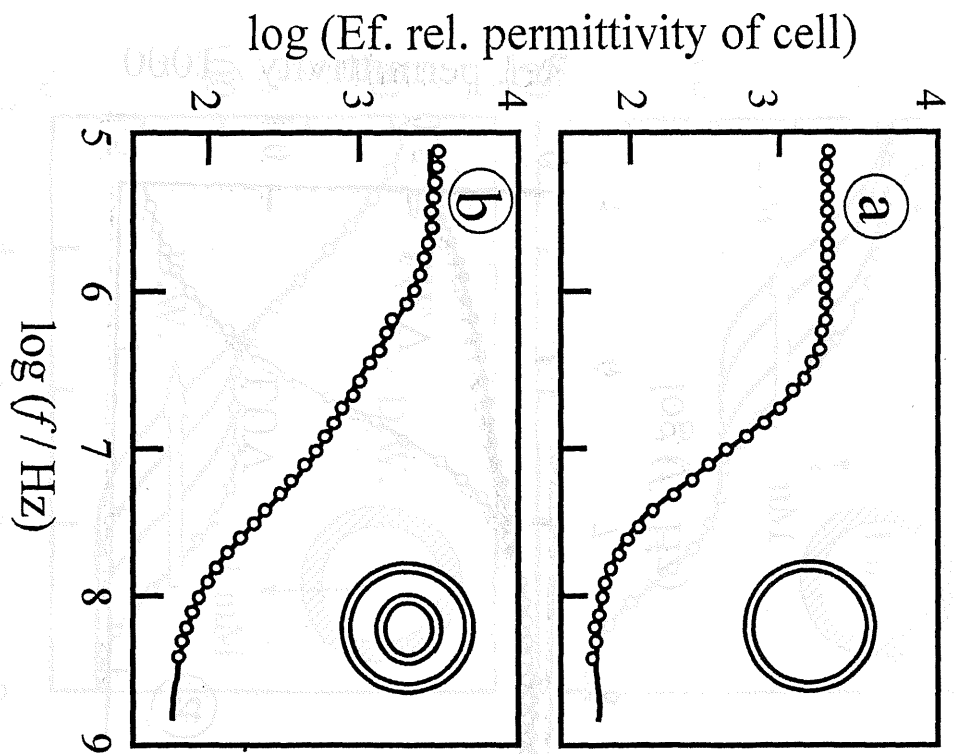


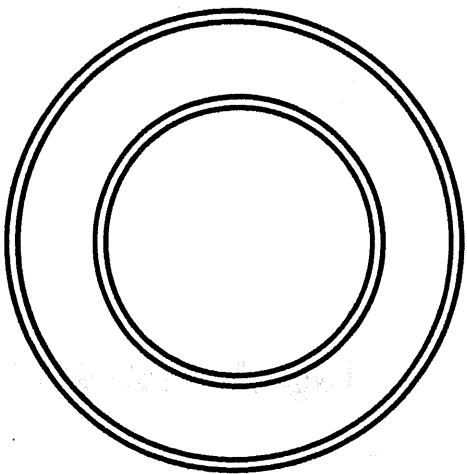




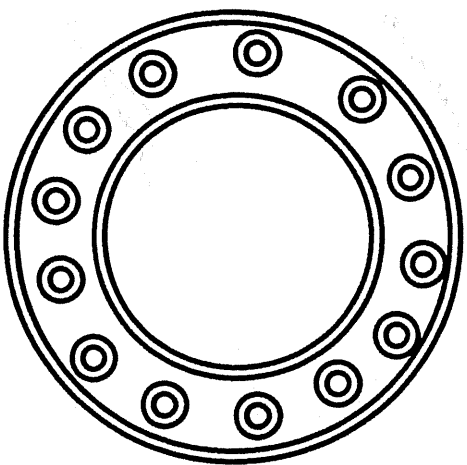




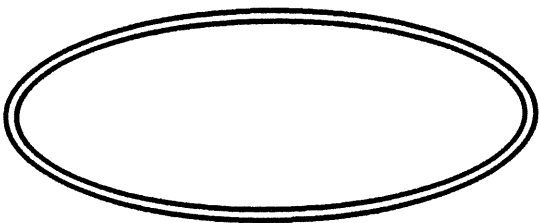




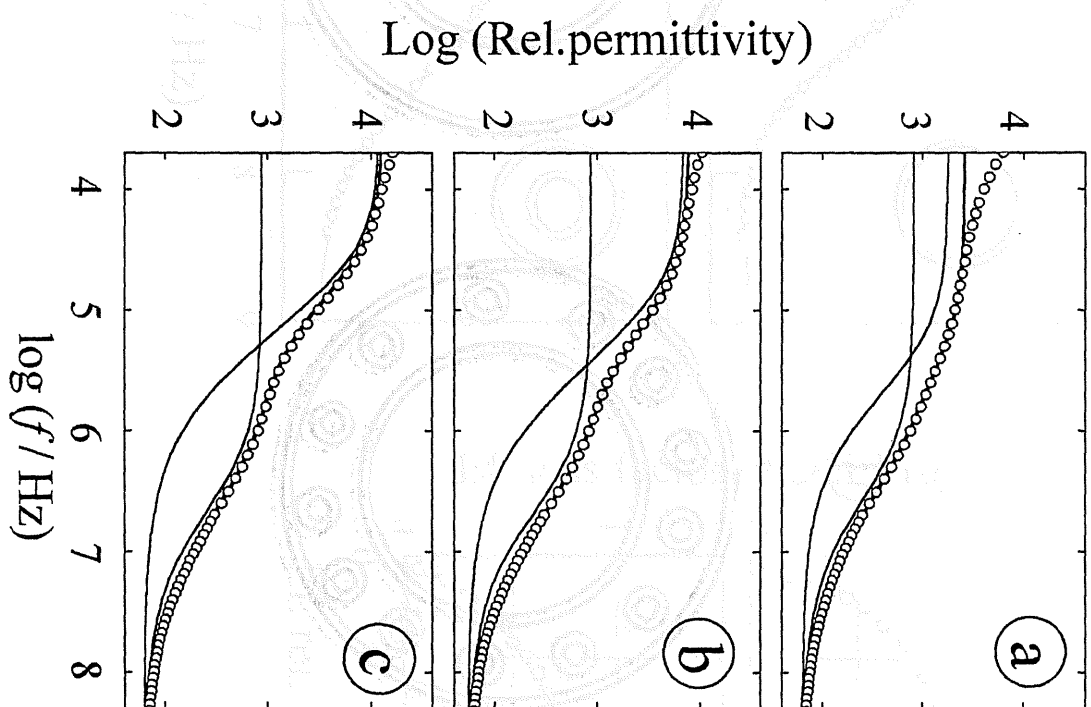
a



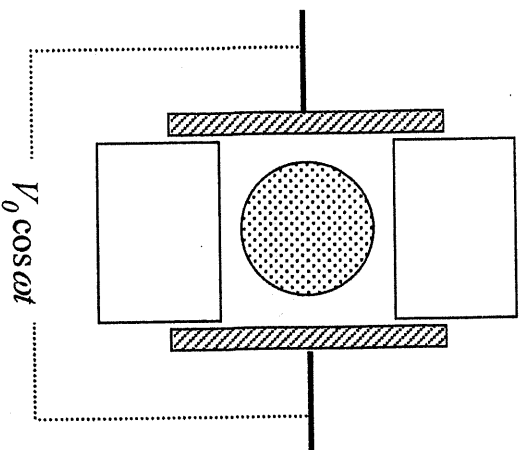
b



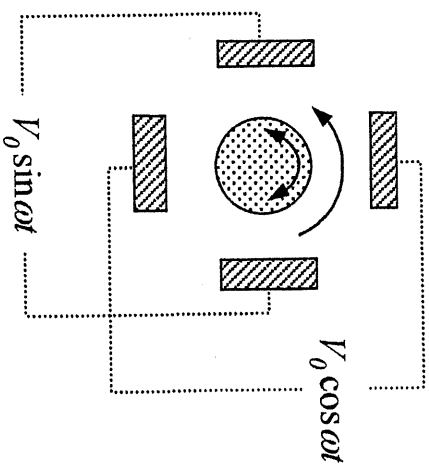
c



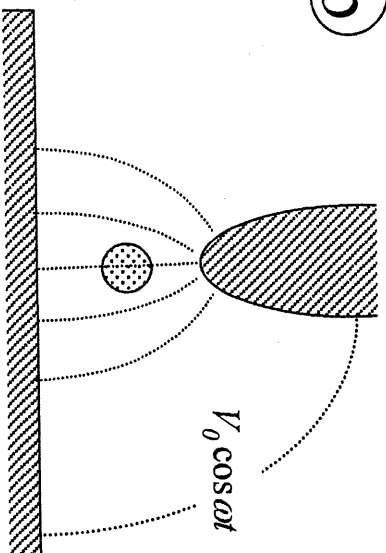
a



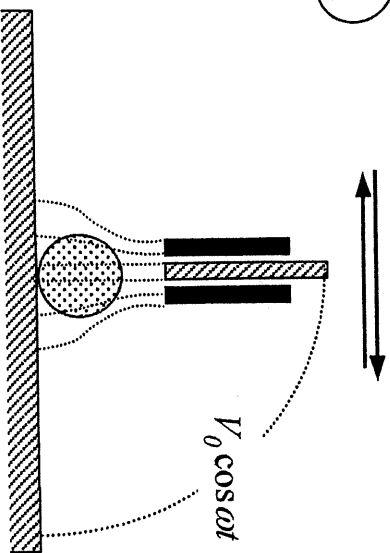
c

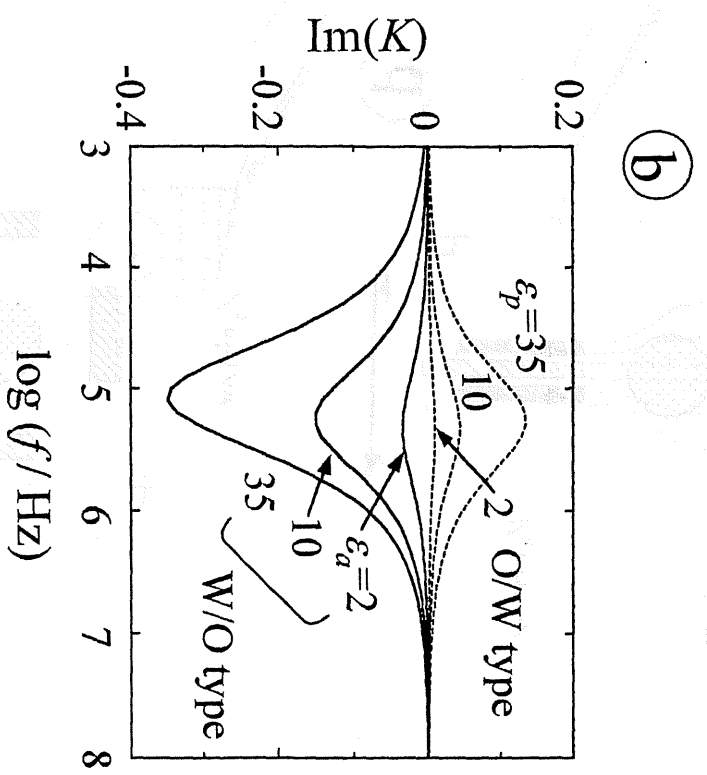
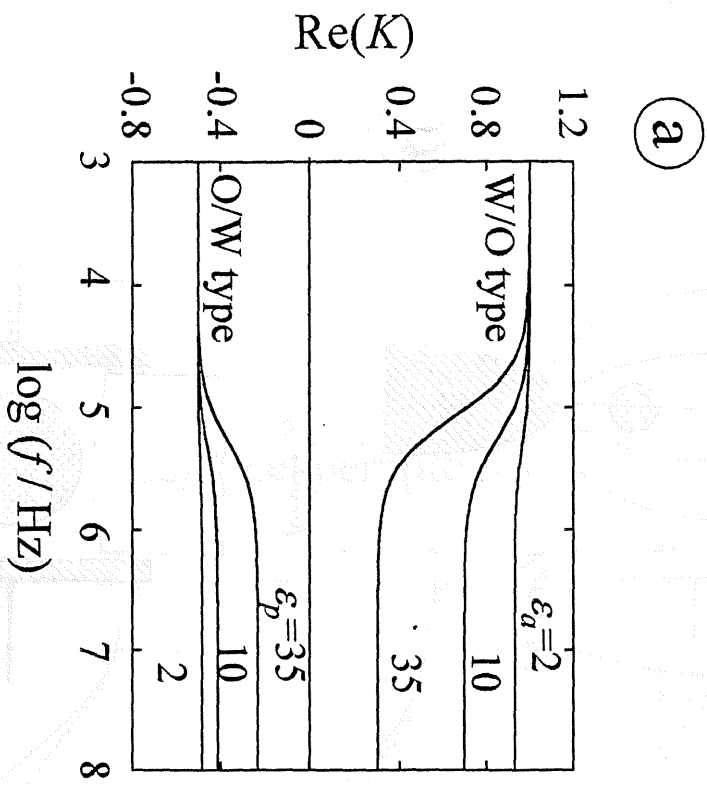


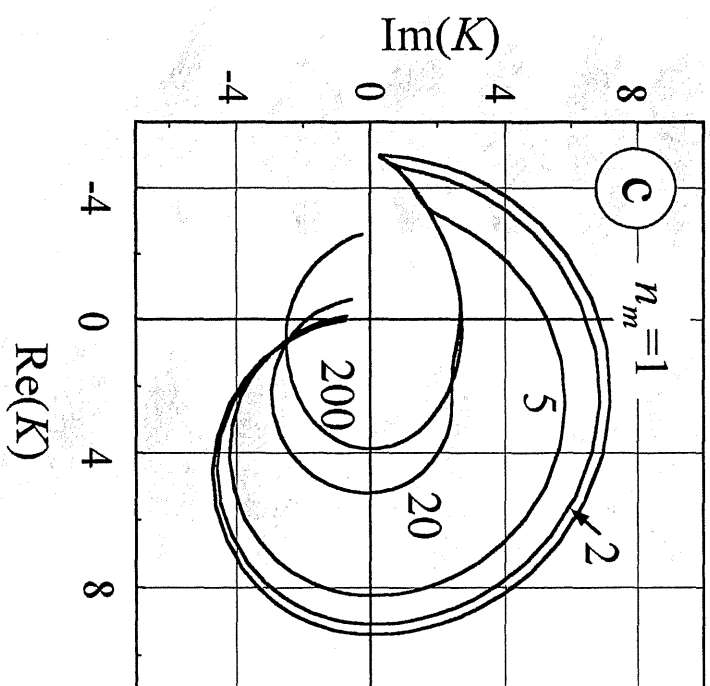
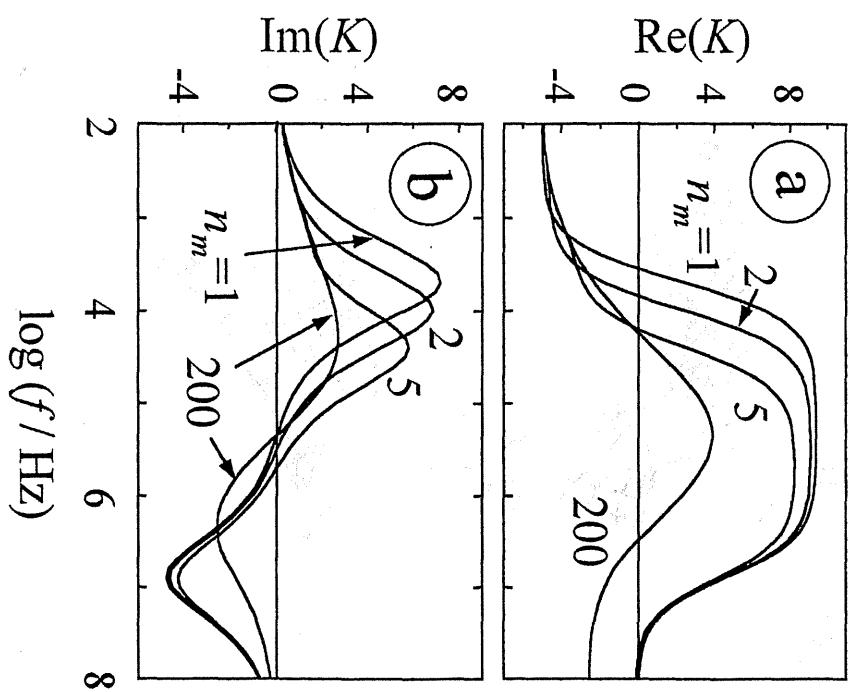
b



d

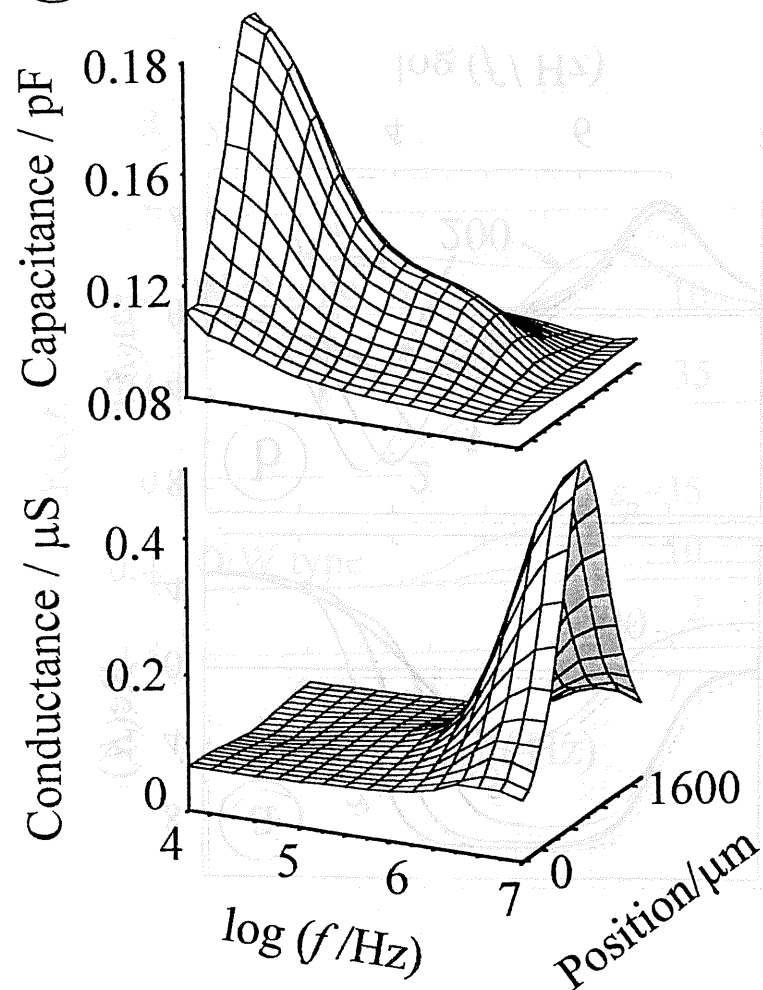








a



b

